

Metal Absorption Systems in Spectra of Pairs of QSOs

David Tytler^{*}, Mark Gleed, Carl Melis, Angela Chapman, David Kirkman
Dan Lubin, Pascal Paschos and Tridivesh Jena

Center for Astrophysics and Space Sciences, University of California San Diego, La Jolla, CA, 92093-0424

and Arlin P.S. Crotts

Department of Astronomy, Columbia University, 550 West 120th Street, New York, NY 10027

2 February 2008

ABSTRACT

We present the first large sample of metal absorption systems in pairs of QSOs with sightlines separated by about 1 Mpc at $z = 2$. We found 691 absorption systems in the spectra of 310 QSOs in 170 pairings. Most of the systems contain C IV or MgII absorption.

We see 17 cases of absorption in one line-of-sight within 200 km s^{−1} (1 Mpc) of absorption in the paired line-of-sight. When we see absorption in one line-of-sight, the probability of also seeing absorption within about 500 km s^{−1} in the partner line-of-sight is at least $\approx 50\%$ at < 100 kpc, declining rapidly to 23% at 100 – 200 kpc and 0.7% by 1 – 2 Mpc. Although we occasionally probe an individual absorbing halo with two lines-of-sight, the absorber-absorber correlation is primarily a probe of the large scale distribution of metals around galaxies and galaxy clustering. With redshifts errors of ~ 23 km s^{−1}, we detect clustering on 0.5 Mpc scales and we see a hint of the “fingers of God” redshift-space distortion. The distribution is consistent with absorbers arising in galaxies at $z = 2$ with a normal correlation function, normal systematic infall velocities and unusually low random pair-wise velocity differences, more consistent with blue than with red galaxies. Absorption in gas flowing out from galaxies with a mean velocity of 250 km s^{−1} would produce vastly more redshift elongation than we see. The UV absorption from fast winds that Adelberger et al. (2005) see in spectra of LBGs is not representative of UV absorption that we see. Either the winds are confined to the UV luminous star forming regions of LBGs and account for under 1/3 of the absorption systems, or if they are common to all galaxies, they can not extend to 40 kpc with large velocities, while continuing to make UV absorption that we can detect. This suggests that the metals were in place in the IGM long before $z = 2$.

Separately, we examine the absorption seen when a sight line passes a second QSO. We see 19 absorbers within ± 400 km s^{−1} of the redshifts of the partner QSO and 30 within 1000 km s^{−1}. These transverse absorbers are more tightly clustered about the QSO redshift than are associated C IV absorbers seen in individual QSO spectra. The probability of seeing absorption when a sight line passes a QSO is approximately constant for impact parameters 0.1 – 1.5 Mpc. Perhaps we do not see a rapid rise in the probability at small impact parameters, because the UV from QSOs destroys some absorbers near to the QSOs. The 3D distribution of 64 absorbers around 313 QSOs is to first order isotropic, with just a hint of the anisotropy expected if the QSO UV emission is beamed into coaxial cones of half apex angle ~ 20 degrees towards and away from the Earth. Alternatively, QSOs might emit UV isotropically but for a surprisingly short time of only 0.3 Myr. Anisotropy is obscured because some z_{em} values have large errors, we do not know the distance from the QSOs at which a given absorber will be destroyed, and the axis of the cone of UV radiation has an unknown angle to our line-of-sight.

Key words: quasars: absorption lines – cosmology: observations – intergalactic medium.

1 INTRODUCTION

In this paper we discuss correlations between metal line absorption systems seen in the spectra of pairs of QSOs with sight lines separated by approximately 1 Mpc proper at $z = 2$. These metal systems probe two separate environments; metals in the outer regions of galaxies that are far from both QSO, and separately, metals in the immediate vicinity of one or both QSOs. We will maintain the distinction between these two environments throughout the paper.

We use moderate resolution spectra (FWHM 100 – 250 km s⁻¹), with a wide range of SNR and hence we are sensitive to a wide range of absorption line equivalent widths. The absorption lines that we see typically come from the outer parts of galaxies, and the regions around the QSOs themselves. We learn little about the distribution of metals in the IGM far from galaxies because those metals tend to make absorption lines that are weaker than most that we can detect.

In general information that we gain from paired sight lines complements what we have learnt from individual sight lines over the last 30 years. However, it remains hard to decide what is causing the absorption, especially because we get velocity and not pure distance information from redshifts in spectra. When we come to examine small scale differences in redshifts, both in single lines of sight, between paired sight lines, or between QSO absorption and adjacent galaxies, peculiar velocities can be comparable to the Hubble flow. Moreover, these peculiar velocities can have systematic as well as random components on small scales. We expect to see net infall relative to Hubble motion when the absorbing region is over-dense, while we might see outflows if the gas is ejected from a galaxy in a wind.

In the remainder of this introduction we discuss metal absorption systems far from the QSO and then those near to the QSO and finally we describe the distance measures that we use. In §2 we describe the sample of 310 QSOs and their separations from their partners. In §3 we present the observations then in §4 we describe the absorption systems that we found. In §5 we discuss the redshift differences between pair of absorbers in different sight lines, and absorbers near to QSOs. In §6 we see that these coincidences have the same ions and W_{rest} values as normal systems. In §7 we see that the absorber-absorber correlation is strong and inconsistent with absorption in fast winds. In §8 we see that the absorbers have a uniform distribution around the QSOs, with a hint of a lack of absorbers near to the line of sight. We mention BAL systems in §9 and discuss our conclusions in §10.

1.1 Metals Absorption Far from QSOs

In general the correlation of metal line absorption between sight lines tells us about the size and structure of the regions that produce metal absorption.

When QSO sight lines are separated by 1 – 100 kpc we see metal absorption lines in each that can have very similar line profiles, indicating that the light is passing through the same gas clouds. Rauch et al. (2002) have studied ions such as Mg II, Ca II, and Fe II in a quadruple gravitationally lensed QSO to derive the structure of metal clouds in the interstellar medium.

For all except exceptionally close sight lines with arcsec-

ond separations, it is hard to distinguish between absorption by a single large cloud and absorption by clouds which are too small to individually cover both sight lines, but that are clustered such that one cloud covers each sight line. Or in terms of a continuous distribution of gas, the density, ionization and metal abundance are changing significantly over the distance between the sight lines. This ambiguity was first stressed by Weymann et al. (1981) and is more apparent in spectra of lower spectral resolution.

The sizes of the metal absorbing regions, either single clouds and clusters of clouds, have been estimated from various pairings on the sky. Lensed images of the same QSO (Steidel & Sargent 1991) probe the smallest separations and give proper sizes of ~ 15 to about ~ 80 kpc ($H_0 = 71$ km s⁻¹ Mpc⁻¹). Pairs of physically distinct QSOs close to each other on the sky, like those used here, typically probe separations greater than 1 Mpc, but the occasional pair is closer and gives sizes of roughly 100 kpc for strong C IV absorbers (Crotts et al. 1994). Chen et al. (2001) find C I V is very often seen out to impact parameters (radii) of 140 kpc around galaxies seen in images, but only rarely beyond that distance. Churchill et al. (2007) discuss one E/SO galaxy that shows no metals at 58 kpc, showing that not all galaxies absorb at large distances. Adelberger et al. (2005) examined the absorption near 1044 foreground galaxies in the spectra of 23 background QSOs and found C IV absorption with column densities $N_{CIV} \gg 10^{14}$ is often seen to radii of 40 kpc, while $N_{CIV} \approx 10^{14}$ is seen to 80 kpc. A corresponding size for M II absorbers at low-redshifts ($z \lesssim 0.5$) is about 70 kpc (Lanzetta & Bowen 1990). We will see strong correlations arising from sight lines that pass through the same halo, but in general out paired sight lines are too far apart to both probe the same halo.

On larger scales the correlation in the redshifts of metal line absorption in adjacent sight lines depend on the clustering of baryons, modified by the spatial variation in both the ratio of metals to baryons, and the level of ionization of the metal atoms.

We know from many large surveys of single QSO sight lines that metal lines are very strongly clustered on scales of < 150 km s⁻¹, with detectable clustering out to beyond 600 km s⁻¹ (Sargent et al. 1988; Petitjean & Bergeron 1994; Rauch et al. 1996; Pichon et al. 2003; Scannapieco et al. 2006), and possibly out to 140 Mpc (for $q_0 = 0.5$) (Quashnock et al. 1996). Absorption systems with higher H I or metal line column densities tend to be more strongly clustered and confined, while those with low column densities are more widespread (Sargent et al. 1980; Tytler 1987; Cristiani et al. 1997).

With some assumptions we can convert velocities along sight lines into a prediction for the correlation between adjacent sight lines. We need to specify the cosmological model, and the 3D density field of the metal ions. The connection between line of sight and transverse clustering is complicated by velocity field distortions. Ignoring these velocity distortions, we would expect the see metal lines weakly correlated in sight lines separated by $< 600/H(z) \simeq 3$ Mpc at $z = 2$. Crotts et al. (1997) found that the clustering of C IV in HIRES spectra of the triplet near 1623+27 was weaker than along the line of sight, they suggest perhaps because peculiar velocities make the clustering appear over extended along the line of sight.

Scannapieco (2005) argues that we expect metals to be highly clustered around their sources that are in high density peaks. Scannapieco et al. (2006) show that the metal line correlations function along a line of sight can be modelled with most metals confined to bubbles of radius 2 Mpc comoving. On the other hand, Pieri et al. (2006) show that the incidence of weak C IV and O VI absorption is similar both near to galaxies (marked by strong metal lines) and far from galaxies, indicating that some metals (mostly below our detection threshold) are present well beyond the immediate surroundings of galaxies.

Coppolani et al. (2006) did not see any significant correlation in 139 C IV systems towards 32 pairs of QSOs, except for an over-density of C IV in front of a group of 4 QSOs. Since the mean separation of their QSO pairs is > 2 arcmin, they conclude that metal enriched “bubbles” should be smaller. Below we will show that we see strong correlations between sight lines, but only when the separations are < 0.6 Mpc. Simcoe et al. (2006) study galaxies and intergalactic gas towards a single QSO at $z=2.73$ and conclude that the metal absorption can arise from bubbles of radii ≈ 100 kpc and thickness ≈ 1 kpc.

On the largest scales Jakobsen et al. (1986) and Sargent & Steidel (1987) discuss evidence for a supercluster filament causing absorption at similar velocities in sight lines separated by 17.9 arcminutes. Romani et al. (1991) describe how absorption in pairs of QSOs could be used to find superclusters at high redshifts, before any galaxies were known at these redshifts. Jakobsen & Perryman (1992) used C IV absorption in 12 QSOs including Tol 1037-2703 to detect a sheet spanning tens of Mpc. Tytler et al. (1993) saw no sign of periodicity on 10 – 210 Mpc scales in the 3D distribution of 268 Mg II absorption systems. Loh et al. (2001) examined the 3D distribution of 345 C IV systems from 276 QSOs and found evidence for clustering on scales up to 220 Mpc ($q_0 = 0.5$). Vanden Berk et al. (2000) found four metal line absorption systems towards QSOs near to the HDF, two of which have redshifts that place them in the second most populated peak in the galaxy redshift distribution. Williger et al. (1996) compiled a statistically complete sample of C IV absorption at $1.5 < z < 2.8$ in 25 sight lines. They found evidence for structure on 2 – 50 Mpc proper scales but not for a smaller sample of 11 Mg II absorbers. Overall, this body of work shows that the distribution of absorption systems clearly reveals large scale structure, especially the redshift spikes seen in all narrow angle galaxy surveys (Broadhurst et al. 1990). The sample presented here is not well suited to studying correlations on these largest scales because we have very low sampling density, and we very rarely see even one metal system when we pass a given group of galaxies.

1.2 Metals Absorption near to QSOs

We are especially interested in absorption by metals around QSOs because these metals will help us understand the feedback of QSOs on the IGM. Specifically, we should learn about the ejection from the QSOs of hot gas that contains metals. We might see absorption from the emission line region, the ISM of the QSO host galaxy, and galaxies in a group that might contain the QSO host. In all cases we expect to see enhanced photoionization by the QSO UV. If the QSO UV is not isotropic then we might see an anisotropic

spatial distribution of the absorbers about the QSOs. We also expect to see a higher density of absorbers near to the QSOs because QSO hosts are in over-dense environments.

The results in the literature on absorption near to QSOs are diverse. We will distinguish between absorption seen along a single line of sight (from a QSO to the Earth) from that seen in the spectrum of a second background QSO (transverse to the line of sight). It also helps to distinguish different ions, since they probe different gas densities and respond differently to the QSO environment. Note however that if we can show that QSOs emit isotropically, or instead are strongly beamed, using one line of evidence, then this result may hold even if other lines of evidence seem to be contradictory. The other evidence might be based on a small sample or the measurements may be less sensitive to the effect in question.

A significant fraction of metal lines systems are intrinsic to QSOs and not at the positions implied by their redshifts. Richards et al. (1999) found that the numbers of C IV systems in a heterogeneous catalogue of absorption systems depended on the optical luminosity and radio properties of the QSOs. If this were confirmed in a homogeneous sample it would be evidence that perhaps 36% of C IV systems are intrinsic. Recently Misawa et al. (2007) used doublet ratios of metal lines in Keck HIRES spectra of 37 QSOs to conduct the first large survey of the frequency of absorbers that do not cover the QSO UV radiation source. They found 28 reliable cases of intrinsic absorption, corresponding to 10 – 17% of narrow C IV systems at velocities of 5000 – 70,000 km s⁻¹ from their QSOs, and at least 50% of QSOs show intrinsic systems. Ganguly & Brotherton (2007) estimate that 60% of QSOs, with a wide range of luminosity, display outflows in absorption that we can see as BAL or associated absorption, or absorption with partial coverage, time variability, high photoionization or high metallicity.

Intrinsic gas that is ejected and clumped in velocity can appear like a supercluster of galaxies along a single sight line. The examination of absorption systems in pairs of QSOs can clarify the situation. The outflows mentioned above are generally believed to be confined to within a few pc to a few kpc of the QSOs (Narayanan et al. 2004; Wise et al. 2004; Misawa et al. 2005), too small a distance to intercept the other line of sight.

1.2.1 Absorption near to QSOs and along individual Lines of Sight (*los*)

We see various behaviours in the number of absorption lines from different ions at velocities near to the QSOs emission redshifts. The amount of H I decreases, probably because of the increased photoionization. The number of Lyman limit Systems (LLS) is little changed, while the number of C IV lines (Young et al. 1982) and DLAs (Russell et al. 2006) increases. N V lines in particular are found mostly near to the QSOs (Petitjean et al. 1994). Prochaska et al. (2007) also study the incidence of DLAs within 3000 km s⁻¹ of their QSOs. At $z < 2.5$ and $z > 3.5$ they see no deviation from a flat intervening distribution, but at intermediate z they see twice the usual number of DLAs. They had expected 5 – 10 times more DLAs near the QSOs because of clustering of galaxies around the QSOs and interpret this lack as due to the enhanced ionization from the QSOs.

It has long been known (Tytler 1982) that there is no strong excess of LLS with $z_{\text{abs}} \simeq z_{\text{em}}$ along individual sight lines to mostly high luminosity QSOs, and hence no sign of absorption in the host galaxies. There are two obvious explanations. First, the QSOs might be in galaxies (elliptical or lenticular) that do not have enough H I columns to make LLS, $\log N_{\text{HI}} > 17.2 \text{ cm}^{-2}$. While high luminosity QSOs are in elliptical galaxies, low luminosity QSOs are often disk galaxies (Hamilton et al. 2002), hence we predict that lower luminosity QSOs may show enhanced LLS at $z_{\text{abs}} \simeq z_{\text{em}}$. Second, the QSO UV radiation or relativistic jets may have ionized the gas in the sight line. In some models, feedback from optical (Di Matteo et al. 2005) or radio loud AGN (Best 2007) can effect the host galaxy as a whole, tending to make it appear like an elliptical galaxy, and hence making the first explanation a consequence of the second: the host is elliptical because of the QSOs effect on the host.

When an absorption system has velocities similar to that of the QSO emission lines, we must be aware that the gas could have significant peculiar velocity, either from gas ejected from the QSO or the motions in a group of galaxies containing the QSO host galaxy. Guimarães et al. (2007) find that the H I proximity effect in 45 high QSOs at $z > 4$ is less than expected, by an amount that implies that QSOs reside in regions with overdensities of 5 to 2 within 3 and $10 h^{-1} \text{ Mpc}$, with higher luminosity QSOs in higher overdensities.

1.2.2 Absorption near to QSOs and seen in background spectra: Transverse

The results of searches for a relative decrease in H I absorption near foreground QSOs, the classical “transverse proximity effect”, are complex and confusing. In early work, Dobrzycki & Bechtold (1991a,b) found a large transverse void in the amount of $\text{Ly}\alpha$ absorption that they concluded was probably not caused by UV from a foreground QSO. Sri-anand (1997) discussed a second void that was less than expected from the foreground QSO luminosity. Fernandez-Soto et al. (1995) and Liske & Williger (2001) claimed marginal detections of the transverse proximity effect while Crotts (1989); Moller & Kjaergaard (1992); Crotts & Fang (1998); Croft (2004); Schirber et al. (2004) saw no lack of H I absorption. Rather, in some cases we have reports of enhanced, instead of decreased H I absorption near foreground QSOs (Crotts & Fang 1998; Croft 2004; Schirber et al. 2004).

Three types of explanation have been discussed for the non-detections of the expected H I transverse proximity effect:

- (i) The QSOs were less luminous in the past, by factors of 10 – 100 some 1 – 30 Myr ago (Schirber et al. 2004).
- (ii) The QSO radiation is beamed so that their typical luminosity in transverse directions is factors of 10 – 100 lower than in the line of sight (los) direction (Barthel 1989; Crotts 1989; Moller & Kjaergaard 1992; Antonucci 1993; Schirber et al. 2004).
- (iii) The H I does feel the full QSO UV luminosity but the increased photoionization is partly cancelled by increased gas density, and the increased number of galaxies near the QSO (Loeb & Eisenstein 1995; Schirber et al. 2004; Rollinde

et al. 2005; Guimarães et al. 2007; Faucher-Giguere et al. 2007; Kim & Croft 2007).

The first two explanations both make the radiation around the QSOs anisotropic, but both narrow beam opening angles and ultra short UV life times are disfavoured by other evidence Urry & Padovani (1995). The third is widely agreed to be a real effect that enhances the numbers of many types of absorbers near to QSOs.

In contrast with H I, there are claims that the He II ionization is changed by the radiation from foreground QSOs (Jakobsen et al. 2003; Worseck & Wisotzki 2006a,b; Worseck et al. 2007). Worseck & Wisotzki (2006a) claim that the hardness of the radiation ionising H and He II changes near to four foreground QSOs and that lifetimes are at least 10 – 30 Myr ago.

Only a few cases of metal line systems near to foreground QSOs have been found (Shaver et al. 1982; Shaver & Robertson 1983, 1985; D’Odorico et al. 2002; Adelberger et al. 2006) because few QSO pairs were known until recently. Williger et al. (1996) found marginal evidence of an association between C IV absorbers and a grouping of 25 QSOs.

Bowen et al. (2006) found excess Mg II absorption in background QSOs at the emission redshift of foreground QSOs. They considered four pairs of QSOs with separations of 3 – 15 arcsec, or 26 – 97 kpc. Since we do not expect to see associated Mg II in 4 out of 4 sight lines, they conclude that the absorbing gas is not isotropic, and they discuss possible explanations (host galaxy, nearby galaxies, ejected gas), none of which were compelling to them.

Hennawi & Prochaska (2007) examine the incidence of a subset of all LLS, those with $\log N_{\text{HI}} > 19 \text{ cm}^{-2}$, in the spectra of 149 QSO pairs with the nearer QSOs at $1.8 < z < 4.0$. They find 17 such LLS in transverse pairings which they argue is larger than the number seen along lines of sight by factors of 4 – 20 times. Hennawi et al. (2006) note their concern over the level of completeness and the false positive rate in their samples, since it is hard to find $\text{Ly}\alpha$ lines with $\log N_{\text{HI}} > 18.3$ or 19.3 cm^{-2} in low SNR moderate resolution spectra, and the reality of an excess depends on the precise minimum N_{HI} values, and the number of false high column systems in their sample. Like Bowen et al. (2006), they suggest that absorbers are an-isotropically distributed. Hennawi & Prochaska (2007) suggest that the LLS absorbers in the line of sight are photo-evaporated while those in the transverse direction are not evaporated because they do not see the full QSO UV flux.

1.3 Distances

We will measure separations in various units. The separations of sight lines in the plane of the sky are known in arcseconds. The errors on these separations are probably less than one arcsecond, but they will be larger when the QSOs lack modern position measurements, or when the two QSOs were measured in different coordinate reference frames. We use a flat cosmological model with $\Omega_{\Lambda} = 0.73$, $\Omega_m = 0.27$ and $H_0 = 71 \text{ km s}^{-1} \text{ Mpc}^{-1}$.

We convert from arcsec to Mpc in the plane of the sky, an impact parameter, using

$$b = \frac{c \delta\phi}{(1+z)H_0} \int_0^z \frac{dz}{\sqrt{\Omega_m(1+z)^3 + \Omega_\Lambda}} \quad (1)$$

where b is the transverse proper distance in the plane of the sky corresponding to the angular separation $\delta\phi$ in radians and measured at redshift z . The b parameter is the proper equivalent of the comoving r_p often seen in galaxy literature. For our cosmological model this gives

$$b = \frac{0.020471}{(1+z)} \int_0^z \frac{dz}{\sqrt{0.27(1+z)^3 + 0.73}} \quad (2)$$

where $\delta\theta$ is now the angular separation in arcseconds, and the integral is 0.44567, 0.78566, 1.24223, 1.75678 for $z = 0.5, 1, 2, 3$. Jakobsen et al. (2003, Eqn 1,2) and Pen (1999) give analytic approximations, and Wright (2006) gives a Java calculator. We do not use the formulae given by Liske (2000) that are required for large angles or large redshift differences.

Distances along the lines of sight are most conveniently expressed as differences of redshift. When we discuss correlations in the positions of absorbers, we are interested in scales of about 1 Mpc or 100 – 400 km/s depending on the redshift. These correlations will include higher density regions that will be expanding less rapidly than the Hubble flow, and some of them may be bound with constant proper size.

We shall convert the differences in redshift into velocity intervals using

$$\frac{v}{c} = \frac{(1+z_1)^2 - (1+z_2)^2}{(1+z_1)^2 + (1+z_2)^2}, \quad (3)$$

which for small intervals is approximately $v/c = H(z)d/c \approx \Delta z/(1+z)$. We can convert these velocities into proper distances d using $v = H(z)d$ where $[H(z)/H_0]^2 = (1+z)^3\Omega_m + \Omega_\Lambda$ for our flat model and $H(z) = 120.70, 201.069, 301.31, 416.91$ km/s at $z = 1, 2, 3$ and 4.

For small distances conversion from velocity along the line of sight using the Hubble constant and ignoring peculiar velocities will be highly inaccurate because of the distortions caused by the systematic peculiar velocities (Kaiser 1988; McDonald 2003; Kim & Croft 2007). The effect of peculiar velocities has been studied in detail for H I Ly α absorption from the IGM (Hui et al. 1999; McDonald & Miralda-Escudé 1999; Rollinde et al. 2003). The goal is to measure the correlation in the H I absorption between adjacent sight lines, divided by the correlation along individual sight lines. The division removes most of the effects of evolution and is used in a geometric cosmological test which Alcock & Paczynski (1979) showed is particularly sensitive to Ω_Λ . In this paper we assume that we know Ω_Λ with negligible error. We discuss redshift-space distortions in §7 and §8.

2 QSO TARGETS

We use spectra of the 310 QSOs which include 140 pairs and 10 triplets. We treat each triple as 3, non-independent pairs, giving 170 QSO-to-QSO pairings. We selected these QSOs because their separations and redshifts are suitable for studying the correlations in the H I Ly α absorption in the Ly α forest. When choosing objects to observe we initially observed all known pairs separated by under a few arcminutes. Later, as more pairs were announced by 2dF Quasar

Redshift Survey (Boyle et al. 1997; Shanks et al. 2000; Miller et al. 2004) and SDSS (York & et al. 2000), we strongly biased our observing to the closest known suitable pairs, typically those within 120 arcseconds. We also strongly biased our sample to pairs with similar emission redshifts, z_{em} , to maximise the redshift of overlap in the region between Ly α and Ly β in the paired spectra. However, some of the pairs discussed here do have widely differing z_{em} values. We also biased the sample against pairs where C IV BAL absorption was at z_{abs} values that would put Ly α at rest wavelengths 1070 – 1170 Å, the key wavelengths for correlations of Ly α in the Ly α forest. Hence the sample contains less than the normal number of BAL QSOs, though there remain BAL systems in 34 of the QSOs, especially weak BAL systems and systems restricted to z_{abs} similar to z_{em} . If we knew from SDSS spectra that a QSO in a pair had strong and widespread BAL absorption then we typically did not obtain new spectra of higher resolution or higher signal-to-noise ratio (SNR) to cover the Ly α forest at wavelengths < 3900 Å that were not covered by the SDSS spectra.

In Table 1 we list the J2000 coordinates of the 310 QSOs their z_{em} values and the separation from the partner QSO in arcseconds. We give each QSO a label comprising a ‘P’, a number, and a letter. The number identifies the pair and the letter ‘a’, ‘b’ or ‘c’ the QSO in that pair or triple. We show the label in bold face when that QSO is part of a triple. The angles listed are from the current QSO to the next QSO in the sequence b, c then a; hence QSO P8c is 217 arcseconds from P8a. The order of the QSOs in this table is not random and mostly relates in part to when we obtained spectra.

In Fig. 1 we show the distribution of the QSO pair separations in arcseconds and in proper Mpc. For this figure we use the lower of the two z_{em} values for each pair when we convert to Mpc since this is the highest z at which their sight lines overlap.

In Fig. 2 we show the proper distance between two sight lines separated by 150 arcsec, the typical separation for our sample, as a function of z . The sight lines reach a maximum separation at $z = 1.628$. We will consider absorption systems at a wide range of z_{abs} values, including low redshifts where the proper distances are $\ll 1$ Mpc.

2.1 Emission Redshifts

The average emission redshift of the QSOs is $z = 2.470$, with a range of 1.84 to 3.84. We took emission redshift z_{em} values from the SDSS when available and otherwise from the literature. The SDSS redshifts use effective rest frame wavelength for emission lines from Vanden Berk & et al. (2001), intended to give z_{em} values that approximate the redshifts of the host galaxies of the QSOs, the so called “systemic redshifts”. The SDSS redshifts are referenced to a composite QSO spectrum with a zero point from the [O III] emission line (Stoughton & et al. 2002, §4.10.2.3). The redshift values are obtained by the SDSS project either by cross-correlation with the composite spectrum or using effective rest wavelengths for emission lines from the composite. We do not know how much these redshifts differ from the systemic values, but we shall see in §5.1 that the small dispersion in the difference between z_{em} values and z_{abs} values in partner QSOs suggests errors are ~ 500 km s $^{-1}$ for some QSOs. Although the errors may be many times larger for some QSOs, depending on the

Table 1. QSO Targets. In order of QSO pair Label number, not RA.

RA (J2000)	Dec (J2000)	z_{em}	Label	Separation
00 44 34.08	+00 19 03.5	1.878	P1a	88.64"
00 44 39.33	+00 18 22.8	1.866	P1b	
00 55 57.46	-32 55 39.0	2.250	P2a	122.53"
00 56 05.33	-32 56 51.1	2.125	P2b	
02 09 54.8	-10 02 23.0	1.970	P3a	12.04"
02 10 00.1	-10 03 54.0	1.976	P3b	
02 56 42.6	-33 15 21.0	1.915	P4a	55.78"
02 56 47.02	-33 15 27.0	1.863	P4b	
03 10 06.08	-19 21 24.9	2.144	P5a	60.27"
03 10 09.05	-19 22 08.1	2.122	P5b	
03 10 36.47	-30 51 08.4	2.554	P6a	72.04"
03 10 41.06	-30 50 27.5	2.544	P6b	
09 14 04.1	+46 10 44.9	2.180	P7a	64.59"
09 14 10.3	+46 10 50.01	2.370	P7b	
09 56 58.73	+69 38 52.5	2.048	P8a	130.92"
09 57 21.22	+69 37 54.5	2.054	P8b	108.83"
09 57 25.94	+69 36 08.5	2.048	P8c	217.08"
11 45 47.55	-00 31 06.7	2.043	P9a	149.34"
11 45 53.67	-00 33 04.5	2.055	P9b	
12 12 51.14	-00 53 42.2	2.473	P10a	74.01"
12 12 56.06	-00 53 36.5	2.459	P10b	
13 06 34.19	+29 24 43.1	1.960	P11a	27.82"
13 06 35.41	+29 25 05.9	1.926	P11b	
13 21 47.86	+01 06 04.8	2.130	P12a	107.86"
13 21 54.33	+01 06 51.9	1.971	P12b	
13 39 39.0	+00 10 22.0	2.122	P13a	101.69"
13 39 45.4	+00 09 45.0	1.869	P13b	
13 46 21.4	-00 38 05.0	1.894	P14a	119.62"
13 46 25.6	-00 39 47.0	1.848	P14b	
14 12 24.51	-01 56 34.0	1.916	P15a	112.60"
14 12 29.73	-01 55 13.1	2.030	P15b	
14 20 45.98	-00 05 18.0	2.193	P16a	299.36"
14 20 55.61	-00 09 40.0	2.193	P16b	
16 12 37.9	+23 57 09.0	2.014	P17a	117.22"
16 12 45.6	+23 58 00.0	2.005	P17b	
16 45 01.09	+46 26 16.0	3.790	P18a	195.32"
16 45 19.62	+46 25 38.3	3.831	P18b	
17 27 56.45	+58 21 55.7	2.368	P19a	111.58"
17 28 06.77	+58 20 39.19	2.011	P19b	
17 30 14.71	+54 56 57.5	2.127	P20a	244.99"
17 30 42.38	+54 56 01.1	2.112	P20b	
17 36 26.73	+55 27 20.7	1.822	P21a	101.46"
17 36 35.51	+55 28 29.4	1.988	P21b	
22 39 41.75	-29 49 55.2	2.101	P22a	154.98"
22 39 48.64	-29 47 48.7	2.068	P22b	63.52"
22 39 51.82	-29 48 37.0	2.121	P22c	152.44"
23 09 11.88	-27 32 27.1	1.930	P23a	49.52"
23 09 15.34	-27 32 45.3	1.927	P23b	
23 26 03.52	-29 37 40.4	2.310	P24a	141.22"
23 26 14.26	-29 37 22.3	2.387	P24b	
09 09 23.13	+00 02 03.9	1.889	P25a	14.99"
09 09 24.01	+00 02 11.0	1.866	P25b	
11 07 25.70	+00 33 53.6	1.883	P26a	24.82"
11 07 27.08	+00 34 07.3	1.882	P26b	
14 35 06.42	+00 09 01.5	2.378	P27a	33.24"
14 35 08.32	+00 08 44.4	2.378	P27b	
15 48 40.77	+53 37 08.59	2.165	P28a	126.11"
15 48 50.17	+53 38 43.0	2.188	P28b	
23 01 12.42	-31 43 45.0	1.977	P29a	67.84"
23 01 17.62	-31 43 59.2	2.132	P29b	
00 45 26.49	-32 00 16.91	1.885	P30a	79.62"
00 45 27.54	-32 01 35.4	1.988	P30b	
01 24 56.45	-28 51 21.0	1.992	P31a	100.69"
01 24 53.09	-28 52 51.5	2.094	P31b	

Table 1. Continued.

RA (J2000)	Dec (J2000)	z_{em}	Label	Separation
01 35 14.53	-00 53 18.9	2.111	P32a	258.23"
01 35 21.00	-00 57 18.2	2.075	P32b	
02 48 25.59	-28 03 55.4	2.139	P34a	193.83"
02 48 40.13	-28 03 32.4	2.209	P34b	
21 36 19.40	+00 41 31.0	2.030	P35a	288.90"
21 36 38.60	+00 41 54.0	1.941	P35b	
23 53 10.02	-27 26 14.09	1.968	P36a	40.35"
23 53 13.03	-27 26 09.4	2.303	P36b	
00 08 52.71	-29 00 44.1	2.645	P37a	78.53"
00 08 57.73	-29 01 26.9	2.610	P37b	
02 18 21.44	-29 53 40.9	2.070	P38a	21.97"
02 18 22.96	-29 53 31.3	1.917	P38b	
03 06 40.91	-30 10 31.9	2.093	P39a	51.21"
03 06 43.75	-30 11 07.49	2.129	P39b	
03 13 24.40	-31 41 44.9	1.954	P40a	17.00"
03 13 25.51	-31 41 54.3	2.065	P40b	
03 33 20.90	-06 12 16.8	2.050	P41a	145.71"
03 33 24.83	-06 10 03.4	2.139	P41b	
21 48 34.95	-29 41 09.9	1.807	P42a	26.74"
21 48 36.61	-29 40 54.19	2.089	P42b	
22 32 20.27	-28 38 58.7	2.204	P43a	50.81"
22 32 23.45	-28 38 29.9	2.065	P43b	
23 59 44.12	-00 57 38.16	1.778	P44a	46.15"
23 59 45.48	-00 58 19.56	1.814	P44b	
00 59 34.10	-08 43 13.1	2.074	P45a	269.92"
00 59 51.67	-08 44 23.8	2.142	P45b	
01 06 57.94	-08 55 00.1	2.354	P46a	181.93"
01 06 58.41	-08 58 01.9	1.827	P46b	
03 40 23.50	+00 31 11.8	1.910	P47a	217.35"
03 40 27.31	+00 34 41.5	1.874	P47b	
08 54 06.10	+42 38 10.0	2.387	P49a	283.22"
08 54 15.40	+42 42 34.0	2.174	P49b	449.63"
08 54 25.00	+42 35 17.0	1.850	P49c	271.04"
10 05 38.50	+57 07 44.0	1.866	P50a	122.15"
10 05 41.30	+57 05 44.0	2.306	P50b	
10 40 32.20	-27 27 48.6	2.331	P51a	291.12"
10 40 33.50	-27 22 58.0	1.937	P51b	133.92"
10 40 40.32	-27 24 36.4	2.460	P51c	220.51"
10 41 21.90	+56 30 01.0	2.052	P52a	65.09"
10 41 29.30	+56 30 23.0	2.267	P52b	
10 43 30.46	-02 30 12.7	2.246	P53a	258.44"
10 43 42.53	-02 33 17.3	1.993	P53b	
11 06 10.70	+64 00 09.0	2.201	P54a	170.00"
11 06 26.60	+63 57 55.0	1.960	P54b	
11 11 12.30	+01 22 01.6	2.417	P55a	91.33"
11 11 14.11	+01 20 34.4	2.150	P55b	280.80"
11 11 31.30	+01 22 25.0	2.010	P55c	285.96"
11 19 22.40	+60 48 51.0	2.014	P56a	142.19"
11 19 28.90	+60 46 37.0	2.293	P56b	164.79"
11 19 31.10	+60 49 21.0	2.645	P56c	70.35"
12 24 27.80	-11 20 50.0	2.495	P57a	253.03"
12 24 41.40	-11 23 25.0	2.171	P57b	
13 31 25.93	+00 44 14.0	2.020	P58a	219.75"
13 31 38.50	+00 42 21.1	2.429	P58b	252.96"
13 31 50.51	+00 45 10.7	1.893	P58c	247.41"
14 16 47.60	+63 02 51.0	2.034	P60a	284.83"
14 16 50.80	+63 07 35.0	1.961	P60b	
14 26 05.80	+50 04 26.0	2.242	P61a	235.17"
14 26 28.00	+50 02 48.0	2.324	P61b	
14 53 29.53	+00 23 57.3	2.538	P62a	259.89"
14 53 37.99	+00 20 10.5	1.859	P62b	
14 58 38.04	+00 24 18.0	1.888	P63a	387.74"
14 59 01.28	+00 21 23.7	1.988	P63b	180.73"
14 59 07.19	+00 21 01.2	3.012	P63c	91.46"

Table 1. Continued.

RA (J2000)	Dec (J2000)	z_{em}	Label	Separation
15 22 43.99	+03 27 19.8	1.998	P64a	249.33"
15 22 46.66	+03 31 25.9	2.287	P64b	
16 06 28.39	+17 31 26.0	2.040	P65a	265.05"
16 06 37.60	+17 35 16.0	2.323	P65b	
16 32 52.30	+37.47 47.99	1.888	P66a	156.19"
16 32 57.60	+37 50 11.0	2.152	P66b	
22 40 26.20	+00 39 38.0	2.200	P67a	213.50"
22 40 40.10	+00 40 24.0	2.200	P67b	
23 31 32.84	+01 06 20.9	2.641	P68a	153.99"
23 31 39.75	+01 04 27.0	2.245	P68b	
23 46 46.02	+12 45 30.18	2.763	P69a	334.44"
23 46 28.21	+12 48 59.89	2.525	P69b	
20 45 33.15	-06 21 54.3	2.014	P70a	182.84"
20 45 22.28	-06 23 19.0	2.157	P70b	
13 48 08.70	+28 40 07.0	2.464	P71a	59.09"
13 48 04.40	+28 40 24.0	2.464	P71b	
09 00 06.90	+03 33 07	1.872	P72a	212.87"
08 59 52.70	+03 33 18	2.163	P72b	
08 04 00.30	+30 20 46	3.446	P73a	269.22"
08 03 42.00	+30 22 54	2.031	P73b	
15 45 44.20	+51 13 07	2.242	P74a	98.27"
15 45 34.60	+51 12 28	2.453	P74b	
17 17 30.70	+26 22 27	2.203	P75a	211.93"
17 17 15.20	+26 21 48	1.934	P75b	
17 29 43.36	+60 21 54.20	1.928	P76a	370.01"
17 30 30.20	+60 19 47.40	2.215	P76b	
17 18 45.00	+30 26 47	2.028	P77a	160.61"
17 18 37.20	+30 28 52	2.028	P77b	
17 28 40.02	+56 39 57.74	1.984	P78a	148.43"
17 28 52.65	+56 41 43.58	1.769	P78b	
14 57 56.27	+57 44 46.90	2.130	P79a	73.63"
14 57 47.55	+57 44 23.50	2.016	P79b	
15 34 12.70	+50 34 05	2.118	P80a	280.61"
15 33 48.30	+50 31 28	2.215	P80b	
15 08 38.11	+60 35 40.10	2.179	P81a	120.46"
15 08 27.67	+60 34 07.40	1.893	P81b	
16 50 51.10	+34 43 10	2.002	P82a	169.84"
16 50 43.30	+34 45 30	1.984	P82b	
07 55 45.60	+40 56 43.61	2.348	P83a	138.18"
07 55 35.61	+40 58 02.90	2.418	P83b	
11 09 52.30	+55 42 24	3.177	P84a	221.68"
11 09 27.20	+55 41 20	3.472	P84b	
11 26 34.30	-01 24 36	3.741	P85a	278.71"
11 26 17.40	-01 26 32	3.607	P85b	
12 19 33.26	+00 32 26.40	2.871	P86a	260.71"
12 19 22.19	+00 29 05.40	2.627	P86b	
13 54 42.90	+59 28 56	2.554	P87a	161.67"
13 54 38.40	+59 31 34	2.992	P87b	
14 19 19.50	+57 45 13	3.339	P88a	248.30"
14 19 00.60	+57 48 30	2.937	P88b	
14 29 51.87	+63 16 31.90	2.403	P89a	188.86"
14 29 33.01	+63 14 12.40	2.749	P89b	
14 35 00.27	+03 54 03.50	2.491	P90a	224.84"
14 34 55.38	+03 50 30.90	2.853	P90b	
14 41 34.30	+61 39 19	2.435	P91a	296.10"
14 40 52.90	+61 38 52	2.898	P91b	
15 59 22.70	+52 00 27	3.101	P92a	145.47"
15 59 17.40	+52 02 44	3.042	P92b	
21 36 29.40	+10 29 52	2.555	P93a	237.83"
21 36 15.40	+10 27 54	2.966	P93b	
08 25 50.20	+35 48 03	3.203	P94a	259.91"
08 25 40.10	+35 44 14	3.846	P94b	
08 31 15.90	+38 14 24	3.073	P95a	216.00"
08 30 53.00	+38 12 43	3.171	P95b	288.08"
08 30 52.90	+38 09 07	3.149	P95c	417.03"

Table 1. Continued.

RA (J2000)	Dec (J2000)	z_{em}	Label	Separation
10 19 37.00	+55 23 55	3.231	P96a	125.37"
10 19 22.90	+55 24 31	3.720	P96b	
11 08 19.15	-00 58 24.00	4.564	P97a	113.03"
11 08 13.86	-00 59 44.50	4.033	P97b	
13 02 16.91	-03 38 03.70	3.714	P98a	141.24"
13 02 08.17	-03 37 10.50	3.718	P98b	
13 48 08.79	+00 37 23.20	3.626	P99a	236.72"
13 47 55.68	+00 39 35.00	3.814	P99b	
17 19 37.90	+29 18 05	3.079	P100a	106.46"
17 19 32.90	+29 19 29	3.294	P100b	
20 53 03.70	-01 04 42	3.115	P101a	137.52"
20 53 02.90	-01 02 25	3.251	P101b	
08 59 59.14	+02 05 19.70	2.980	P102a	275.29"
08 59 56.83	+02 09 52.80	2.233	P102b	
13 37 57.87	+02 18 20.90	3.332	P103a	172.33"
13 37 56.34	+02 15 30.10	2.314	P103b	
10 42 53.43	-00 13 00.90	2.958	P104a	289.81"
10 42 43.12	-00 17 06.00	1.969	P104b	
09 45 08.00	+50 40 57	3.736	P105a	182.57"
09 44 53.80	+50 43 00	3.789	P105b	
11 04 11.60	+02 46 55	2.533	P106a	131.25"
11 04 03.00	+02 47 20	2.374	P106b	
13 12 13.84	+00 00 03.00	2.680	P107a	148.43"
13 12 13.29	+00 02 31.20	2.842	P107b	
15 54 07.74	+01 00 10.10	2.606	P108a	239.10"
15 53 59.96	+00 56 41.40	2.630	P108b	
01 06 16.06	+00 15 24.00	3.043	P109a	243.02"
01 06 12.22	+00 19 20.10	3.110	P109b	
08 40 55.70	+37 04 37	3.152	P111a	178.10"
08 40 42.20	+37 05 52	2.905	P111b	
13 24 11.60	+03 20 50	3.670	P112a	154.19"
13 24 01.50	+03 20 20	3.371	P112b	
14 30 06.40	-01 20 20	3.249	P113a	199.75"
14 29 57.10	-01 17 57	3.111	P113b	
15 00 58.70	+61 45 06	2.587	P114a	287.78"
15 00 23.50	+61 47 29	2.994	P114b	
15 37 29.50	+58 32 24	3.059	P115a	202.31"
15 37 15.70	+58 29 33	2.590	P115b	
01 02 51.85	-27 53 03.30	1.768	P116a	81.11"
01 02 57.35	-27 53 38.82	1.800	P116b	
15 19 13.29	+23 46 58.72	1.834	P117a	101.25"
15 19 19.40	+23 46 02.00	1.903	P117b	
16 25 48.00	+26 44 32.50	2.490	P118a	146.44"
16 25 48.75	+26 46 58.60	2.526	P118b	180.33"
16 25 57.66	+26 44 43.40	2.605	P118c	129.86"
21 42 25.90	-44 20 17.00	3.230	P119a	61.52"
21 42 22.20	-44 19 30.00	3.220	P119b	
21 43 07.01	-44 50 47.60	3.250	P120a	33.15"
21 43 04.09	-44 50 36.00	3.060	P120b	
09 45 05.93	-00 46 45.00	2.299	P121a	261.94"
09 44 54.24	-00 43 30.40	2.292	P121b	
09 27 43.02	+29 07 34.7	2.2530	P122a	57.60"
09 27 47.27	+29 07 20.7	2.2920	P122b	
11 51 38.05	+02 06 10.30	2.258	P123a	260.18"
11 51 22.14	+02 04 26.30	2.401	P123b	
14 11 08	+62 24 52	2.264	P124a	200.66"
14 11 30.7	+62 22 48	2.305	P124b	
09 46 42.43	+33 07 54.8	2.477	P125a	194.21"
09 46 56.17	+33 06 25.8	2.484	P125b	
08 33 21.61	+08 12 38.3	2.518	P126a	208.57"
08 33 26.82	+08 15 52.0	2.572	P126b	
10 00 52.21	+45 00 11.0	2.567	P127a	199.33"
10 00 54.38	+45 03 29.0	2.649	P127b	
09 35 31.84	+36 33 17.6	2.858	P128a	231.84
09 35 48.51	+36 31 21.9	2.977	P128b	

Table 1. Continued.

RA (J2000)	Dec (J2000)	z_{em}	Label	Separation
14 22 49.19	+42 02 46.2	3.071	P129a	106.87"
14 22 39.88	+42 02 20.4	3.236	P129b	
12 09 17.94	+11 38 30.4	3.105	P130a	196.41"
12 09 10.71	+11 35 45.2	3.122	P130b	
08 52 32.18	+26 35 26.2	3.208	P131a	170.86"
08 52 37.94	+26 37 58.6	3.29	P131b	
08 03 05.84	+50 32 15.3	3.244	P132a	190.91"
08 03 21.24	+50 34 17.4	3.245	P132b	
12 38 15.04	+44 30 26.2	3.254	P133a	232.24"
12 38 31.46	+44 32 58.2	3.268	P133b	
08 36 59.84	+35 10 19.4	3.319	P134a	269.47"
08 37 00.83	+35 05 50.2	3.311	P134b	
14 21 49.99	+46 59 38.6	3.678	P135a	201.85"
14 22 09.71	+46 59 32.5	3.798	P135b	
10 54 16.47	+51 27 24.6	2.367	P136a	238.50"
10 54 16.51	+51 23 26.1	2.341	P136b	
12 13 03.26	+12 08 39.2	3.384	P137a	137.99"
12 13 10.72	+12 07 15.1	3.469	P137b	
10 39 41.49	+55 09 27.8	3.709	P138a	258.46"
10 39 49.28	+55 13 37.5	3.851	P138b	
08 07 44.89	+23 48 25.7	3.745	P140a	225.90"
08 07 35.01	+23 51 26.4	3.76	P140b	
22 47 21.06	-09 15 45.7	4.13	P141a	284.94"
22 47 40.17	-09 15 11.8	4.167	P141b	
23 38 15.45	-10 19 17.2	2.279	P142a	281.75"
23 37 56.58	-10 20 00.1	2.436	P142b	
14 34 08.31	+23 22 30.0	3.97	P143a	166.07"
14 33 56.26	+23 22 22.8	4.16	P143b	
10 16 05.84	+40 40 05.8	2.99	P144a	68.24"
10 16 01.50	+40 40 52.9	2.963	P144b	
13 56 07.50	+58 12 36.1	3.32	P145a	89.15"
13 55 57.54	+58 13 18.0	3.371	P145b	
11 52 10.43	+45 18 25.8	2.282	P146a	113.40"
11 52 00.54	+45 17 41.4	2.379	P146b	
15 09 25.64	+50 56 09.3	2.365	P147a	119.68"
15 09 32.23	+50 57 51.5	2.343	P147b	
16 43 30.13	+30 55 41.8	2.703	P148a	244.49"
16 43 41.28	+30 58 59.8	2.559	P148b	
09 16 11.02	+33 11 30.5	3.112	P149a	152.45"
09 16 03.40	+33 09 31.8	3.153	P149b	
11 06 11.11	+13 56 00.0	3.908	P150a	101.72"
11 06 16.68	+13 54 58.6	3.846	P150b	
08 15 14.28	+06 05 42.5	2.495	P151a	64.08"
08 15 18.32	+06 06 04.3	2.529	P151b	
16 23 23.68	+33 12 32.6	2.411	P152a	103.69"
16 23 24.76	+33 10 49.8	2.585	P152b	
11 43 16.98	+13 24 00.8	2.514	P153a	138.30"
11 43 23.44	+13 25 42.0	2.515	P153b	
10 40 04.02	+32 21 50.6	2.609	P154a	191.02"
10 40 19.09	+32 21 56.4	2.649	P154b	
11 16 10.68	+41 18 14.5	2.98	P155a	13.75"
11 16 11.73	+41 18 21.5	2.971	P155b	

emission lines used to obtain the z_{em} values (Gaskell 1982; Tytler & Fan 1992; Vanden Berk & et al. 2001; Richards et al. 2002), the number of absorbers at negative velocities implies that z_{em} errors are typically $< 1000 \text{ km s}^{-1}$.

In Fig. 3 we show the distribution of the differences in the z_{em} values, where we define for each pair of QSOs

$$\Delta z_{EE} = |z_{\text{em}1} - z_{\text{em}2}|. \quad (4)$$

There is a strong tendency for QSOs in the sample to have

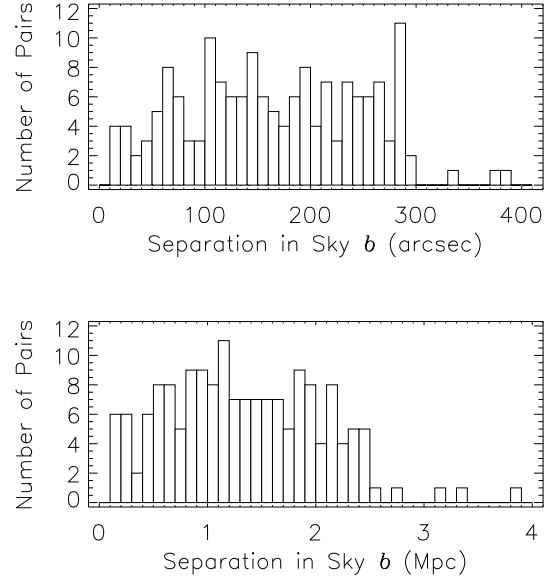


Figure 1. Separation of pairs of QSOs in arcseconds (upper, in bins of 10 arcsec) and proper Mpc in the plane of the sky, b (lower, in bins of 0.1 Mpc). We calculate the separation using the lower of the two z_{em} values. In this and many other figures we move the zero of the horizontal axis away from the vertical axis.

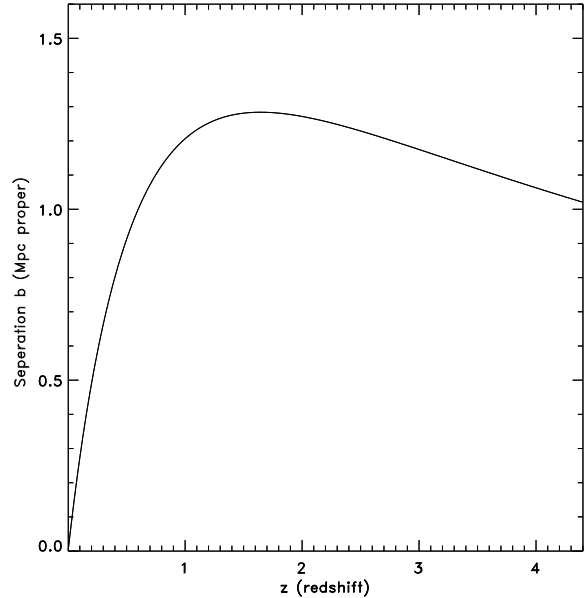


Figure 2. Proper distance between two sight lines separated by 150 arcsec as a function of redshift for the model we use in this paper with $\Omega_{\Lambda} = 0.73$, $\Omega_m = 0.27$ and $H_0 = 71 \text{ km s}^{-1} \text{ Mpc}^{-1}$.

very similar z_{em} values, because most of the pairs with the smallest angular separation are physical pairings (Hennawi et al. 2006; Shen et al. 2007), and because we favoured pairs with the most similar z_{em} values when we obtained spectra. We see a wide range of Δz_{EE} values with a pronounced excess at < 0.04 (4000 km s^{-1}) approximately. This excess has

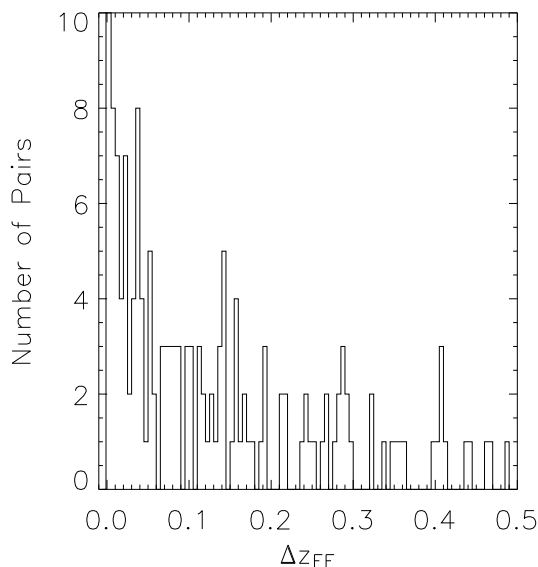


Figure 3. Distribution of the Δz_{EE} values, the difference between the z_{em} values of the QSOs in each pair, in bins of 0.005.

a major effect on the correlation of z_{abs} values, because there is also a pronounced excess of absorbers with $z_{abs} \simeq z_{em}$ in the individual sight lines.

3 OBSERVATIONS

We use spectra that we obtained with LRIS on the Keck I telescope, the Kast spectrograph on the Lick 3-m Shane telescope and from CTIO and KPNO. We also use spectra from the SDSS data release 5 (DR5).

We obtained spectra with LRIS (McCarthy et al. 1998; Oke et al. 1995) from 2001 to 2004 September. While we attempted to obtain spectra of a given pair on a given night, there are many cases where the partner spectrum was obtained on different nights or even in different years. The paired spectra then often have different resolution and wavelength coverage because LRIS changed.

In Table 2 we summarise the different grisms and gratings that we used with LRIS. LRIS is a double spectrograph with independent blue and red dispersers and cameras. We used various grisms and gratings to best match the targets to changes that were made in the instrument. We took blue spectra using either the 400/3400 grism or the 1200/3400 grism. The high resolution 1200/3400 grism has the advantage of showing weak absorption lines, but it sometimes had lower efficiency than the low resolution grism and there is an unavoidable gap at wavelengths 3880 – 4600 or 3770 – 4600 Å between the blue and red side spectrum. We took red spectra using either the 600/5000 grating or the 900/5500 grating. For the red spectra LRIS-R was used with the 2048 × 2048 Tektronix CCD with 24 μm pixels. For blue spectra prior to June 2002 LRIS-B was used with a SITe 2048 × 2048 engineering grade CCD similar to the red CCD. After the mid 2002 LRIS upgrade, blue spectra were obtained

Table 2. LRIS CCDs, Grisms and Gratings

CCD Used		
A	Marconi mosaic	
B	old blue SITe	
C	red	
	Blue Grism ¹	Red Grating ¹
1	1200/3400	
2	400/3400	
3		600/5000
4		900/5500
5	600/4000	

¹ Grooves per mm/Blaze Wavelength (Å)

with a mosaic of two Marconi 2048 × 4096 CCDs with 15 μm pixels.

In Table 3 we list the wavelength ranges covered by the various CCD, grating and grism choices and the FWHM resolution for a given slit. Setups A, B and C are for LRIS on Keck, and D is for RCSP on the CTIO and KPNO 4-m telescopes. We see significant differences between the resolution of individual spectra even when we use the same gratings and slit, because of differences in the focus, seeing and guiding.

In Table 4 we give the observation date, the width of the slit we used, the setup, exposure times, and the SNR per pixel for each spectra. Unless otherwise noted, we measured the SNR at 4200 Å for spectra observed with the A2 or B2 setup, and at 5200 Å for spectra observed with the A1 or B1 setup. We give the SNR for only a sub-sample of all spectra. The majority of the QSOs were observed using the 0.7 arcsecond slit but we used a 1.0 arcsecond slit for twenty nine QSOs. Exposure times for the objects ran from 460 seconds to 8000 seconds. Spectra were extracted using the standard IRAF extraction packages and our own software that is designed to give accurate flux calibration with the optimal SNR. In Table 4 we only list a pair if we obtained spectra of one or both QSOs. We do not list the pairs for which we used SDSS and no other spectra.

The spectra from Lick observatory used the Kast Double Spectrograph on the 3-m Shane telescope. We typically used the 830 grooves/mm grism blazed at 3460 Å in the blue camera and a 1200 groove/mm grating blazed at 5000 Å in the red camera. A dichroic with a 50% transmission near 4600 Å was used, and the wavelengths are setup to cover 3175 – 5880 Å with no gaps. The dispersion are 1.13 Å per pixel in the blue and 1.17 Å in the red. The typical slit gives approximately 2.5 pixels per FWHM depending on the wavelength and focus setting. We show similar spectra in Tytler et al. (2004).

4 ABSORPTION SYSTEMS

We take care to describe the types of absorption systems that we see in the spectra, since the spectra have various resolutions, wavelength coverage and SNR, all of which have a major effect on whether we detect an absorption system

Table 3. Spectra Characteristics.

Setup	Wavelength Range (Å)	Pixel (Å)	Slit (")	(Å)	FWHM (km s ⁻¹)	N ¹
A1	3200–3880	0.24	0.7	0.98 ²	83 ³	26
A1	3200–3880	0.24	1.0		108 ⁴	27
A1	3200–3880	0.24	1.5		162 ⁴	4
B1	3000–3770	0.41	0.7		105 ± 10 ^{5,6}	13
A2	3180–5800	1.07	0.7	4.21 ²	281 ³	7
B2	3000–5300	1.46	0.7		260 ± 30 ^{5,7}	21
C3	5500–8070	1.28	0.7	3.59 ⁸	166 ³	14
C4	4600–6330	0.85	0.7	2.39 ⁸	131 ³	53
C4	4600–6330	0.85	1.0	3.10 ⁸	170 ³	29
C4	4600–6330	0.85	1.5		255 ⁹	4
D1 ¹⁰	3180–6240	1.01	–	3.2	199 ³	2
D2 ¹¹	1600–4720	0.52	–	3.2	234 ³	2
D3 ¹²	3150–4720	0.76	–	1.8	135 ± 10 ⁵	3
D4 ¹⁰	3600–6700	1.01	–	3.2	163 ³	4
SDSS	3800–9200	0.90			165.5	164
LICK	3175–5880	1.15	2.3		250 ⁵	45

¹ *N* is the number of spectra with that setup.

² Values from Chuck Steidel 2002 July on LRIS web site:

http://www.astro.caltech.edu/~ccs/lrisb/new_numbers.txt

³ Converted from the FWHM in Å at the central wavelength of the spectrum, or the central wavelength to the red of Ly α emission when only one or two pairs of QSOs, or using 6500 Å for C3.

⁴ Gussed value. For the 1.0" slit we multiply the value for A1 by 1.3, the factor increase reported by Tonry (1998, §2) for the 600 g/mm grating. For the 1.5" slit we multiply the 1.0" value by 1.5.

⁵ Measured by comparing the Ly α forest in Keck HIRES spectra of bright QSOs, following Suzuki et al. (2003).

⁶ Constant from 3200 – 3600 Å.

⁷ Decreasing from 300 km s⁻¹ at 4350 Å to 235 km s⁻¹ at 5320 Å.

⁸ From Tonry (1998, §2) for the 600 g/mm grating and times 2/3 for the 900 g/mm.

⁹ Gussed value. We multiply the value for the 1.0" slit by 1.5.

¹⁰ CTIO 4m RCSP KPGL-1 632 g/mm grating blazed at 4200 Å.

¹¹ As D1 and including an HST FOS G270H spectrum.

¹² KPNO 4m RCSP BL 420 grating with 600 g/mm and blazed at 8000 Å.

at a given z_{abs} value. We will describe the procedure, what we found and what we could have found.

We began by looking for absorption to the red of the Ly α emission where we expect only metal ions. We identify many systems from the doublet lines and we then searched for other ions and Ly α absorption at the same redshift. Absorption systems with a single doublet will usually be reliable. The least reliable are perhaps those with N V alone, since they tend to lie on the red side of the peak of the Ly α emission where the flux changes rapidly and the continuum level is least reliable. Most will be real, and we could but we did not conduct a systematic search for Si III 1206 to attempt to confirm them.

We fit the absorption lines with Voigt profiles convolved to the spectral resolution. At the resolution of these spectra some lines are approximately a single unresolved Gaussian, but many others show velocity structure. If the velocity structure is clearly resolved, we list separate z_{abs} values for each component. When components are not well resolved,

Table 4. Keck LRIS Observations

Label	Date	Slit	Setup	Exposure Time (s)		S/N
				Blue	Red	
P1a	11/2001	0.7	B2,C4	1200	1200	35
P1b	11/2001	0.7	B2,C4	900	900	54
P2a	11/2001	0.7	B2,C4	2700	2700	46
P2b	11/2001	0.7	B2,C4	3600	3600	55
P3a	10/2001	0.7	B2,C4	2700	2700	17
P3a	08/2002	0.7	A1,C4	2400	2400	
P3a	09/2004	1.0	A1,C4	2200	2200	
P3b	10/2001	0.7	B2,C4	3600	3600	45
P3b	08/2002	0.7	A1,C4	462	462	
P3b	09/2004	1.0	A1,C4	3600	3600	
P4a	10/2001	0.7	B2,C4	900	900	6
P4a	11/2001	0.7	B2,C4	900	900	
P4a	09/2004	1.0	A1,C4	1800	1800	
P4a	09/2004	1.0	A1,C4	2400	2400	
P4b	10/2001	0.7	B2,C4	600	600	42
P4b	08/2002	0.7	A1,C4	300	300	
P5a	10/2001	0.7	B2,C4	424	423	32
P5a	10/2001	0.7	B2,C4	900	900	32
P5a	08/2002	0.7	A1,C4	2400	2400	
P5b	10/2001	0.7	B2,C4	1800	1800	51
P6a	08/2001	0.7	B2,C3	1200	1200	10
P6b	08/2001	0.7	B2,C3	1200	1200	16
P7a	03/2003	0.7	A1,C4	5400	5250	23
P7b	03/2003	0.7	A1,C4	5600	5400	26
P8a	03/2003	0.7	A1,C4	3600	3450	33
P8a	03/2003	1.0	A1,C4	2300	2300	
P8b	04/2001	0.7	B1,C4	1800	1800	17
P8b	03/2003	1.0	A1,C4	3600	3600	
P8c	04/2001	0.7	B1,C4	1800	1800	12
P9a	03/2003	1.0	A1,C4	1000	1000	33
P9b	03/2003	0.7	A1,C4	3600	3420	21
P10a	04/2001	0.7	B1,C4	3000	3000	10
P10b	04/2001	0.7	B1,C4	3000	3000	7
P11a	03/2003	0.7	A1,C4	5400	5250	35
P11b	03/2003	0.7	A1,C4	5400	5250	16
P11b	04/2004	0.7	A1,C4	4600	4600	
P12a	03/2003	0.7	A1,C4	3300	3150	30
P12b	03/2003	0.7	A1,C4	3300	3150	20
P13a	03/2003	0.7	A1,C4	2700	2550	41
P13b	03/2003	0.7	A1,C4	2700	2550	36
P14a	03/2003	0.7	A1,C4	2900	2750	13
P14b	03/2003	0.7	A1,C4	1500	1350	13
P15a	07/2002	0.7	A1,C4	7262	7262	22
P15b	08/2002	0.7	A1, –	3200	–	5 ¹
P16a	07/2002	0.7	A2,C3	1800	1800	47
P16b	07/2002	0.7	A2,C3	1800	1800	40
P17a	04/2001	0.7	B1,C4	2400	2400	24
P17b	04/2001	0.7	B1,C4	2700	2700	39
P18a	07/2002	0.7	A2,C3	2700	2700	21 ²
P18b	08/2001	0.7	–, C3	–	3600	19 ²
P19a	07/2002	0.7	A2,C3	2300	2300	34
P19b	07/2002	0.7	A2,C3	2100	2100	35
P20a	07/2002	0.7	A2,C3	900	900	8
P20a	08/2002	0.7	A1,C4	3421	3421	
P20b	07/2002	0.7	A2,C3	1500	1500	31
P21a	07/2002	0.7	A1,C4	5400	5400	33
P21b	07/2002	0.7	A1,C4	3600	3600	40
P22a	08/2001	0.7	B2,C3	1200	1200	29
P22b	08/2001	0.7	B2,C3	3600	3600	42
P22c	08/2001	0.7	B2,C3	1901	1046	73
P23a	08/2001	0.7	B2,C3	900	900	25
P23b	10/2001	0.7	B2,C4	2700	2700	6
P24a	11/2001	0.7	B2,C4	3300	3300	23
P24b	11/2001	0.7	B2,C4	1500	1500	22

Table 4. Continued.

Label	Date	Slit	Setup	Exposure Time (s)		S/N
				Blue	Red	
P25a	04/2004	0.7	B1,C4	3600	3600	
P25b	04/2004	0.7	B1,C4	600	600	
P26a	04/2004	0.7	B1,C4	2160	2160	
P26b	04/2004	0.7	B1,C4	4100	4100	
P27a	04/2004	0.7	B1,C4	3914	3914	
P27b	04/2004	0.7	B1,C4	4900	4900	
P28a	08/2003	3.3	LICK	3601	3601	
P28b	04/2004	0.7	B1,C4	2800	2800	
P29a	07/2002	0.7	A1,C4	4600	4600	
P29b	07/2002	0.7	A1,C4	2880	2880	
P30a	09/2004	1.0	A1,C4	2700	2700	
P30b	09/2004	1.0	A1,C4	4500	4500	
P31a	09/2004	1.0	A1,C4	1800	1800	
P31b	09/2004	1.0	A1,C4	1800	1800	
P32a	09/2004	1.5	A1,C4	2400	2400	
P32b	09/2004	1.5	A1,C4	2200	2200	
P34a	09/2004	1.0	A1,C4	2300	2300	
P34b	09/2004	1.0	A1,C4	3200	3200	
P35a	09/2004	1.5	A1,C4	2400	2400	
P35b	09/2004	1.5	A1,C4	1200	1200	
P36a	09/2004	1.0	A1,C4	1800	1800	
P36b	09/2004	1.0	A1,C4	5400	5400	
P37a	09/2003	1.0	A5,C4	2200	2200	
P37b	09/2003	1.0	A5,C4	4000	4000	
P38a	09/2003	1.0	A1,C4	4800	4800	
P38b	09/2003	1.0	A1,C4	2500	2500	
P39a	09/2003	1.0	A1,C4	2500	2500	
P39b	09/2003	1.0	A1,C4	3050	3050	
P40a	09/2003	1.0	A1,C4	5100	5100	
P40b	09/2003	1.0	A1,C4	3700	3700	
P41a	09/2003	2.3	LICK	4805	4805	
P41b	09/2003	2.3	LICK	4800	4800	
P42a	09/2003	1.0	A1,C4	3000	3000	
P42b	09/2003	1.0	A1,C4	5400	5400	
P43a	09/2003	1.0	A1,C4	3600	3600	
P43b	09/2003	1.0	A1,C4	2300	2300	
P44a	09/2003	1.0	A1,C4	2000	2000	
P44b	09/2003	1.0	A1,C4	1500	1500	
P45a	08/2003	3.3	LICK	4802	4802	
P45b	08/2003	3.3	LICK	6303	6303	
P46a	12/2004	2.3	LICK	4802	4802	
P49a	03/2005	2.3	LICK	5421	5421	
P50b	03/2005	2.3	LICK	5403	5403	
P51a	03/2005	2.3	LICK	1451	1451	
P51b	03/2005	2.3	LICK	4515	4515	
P52a	12/2004	2.3	LICK	9005	9005	
P52b	03/2005	2.3	LICK	5402	5402	
P53a	03/2005	2.3	LICK	5407	5407	
P54a	03/2005	2.3	LICK	3622	3622	
P55b	03/2005	2.3	LICK	5406	5406	
P56c	03/2005	2.3	LICK	5405	5405	
P57a	03/2005	2.3	LICK	5404	5404	
P58b	03/2005	2.3	LICK	5413	5413	
P60a	03/2005	2.3	LICK	4513	4513	
P61a	03/2005	2.3	LICK	5403	5403	
P61b	03/2005	2.3	LICK	5402	5402	
P62a	03/2005	2.3	LICK	5400	5400	
P63b	03/2005	2.3	LICK	5410	5410	
P64b	03/2005	2.3	LICK	5408	5408	
P65b	03/2005	2.3	LICK	4524	4524	
P66b	08/2003	3.3	LICK	4000	4000	
P67a	08/2003	3.3	LICK	3602	3602	
P69a	09/1998	2.0	LICK	5400	5400	
P70b	09/2003	2.0	LICK	7200	7200	

Table 4. Continued.

Label	Date	Slit	Setup	Exposure Time (s)		S/N
				Blue	Red	
P72b	03/2005	2.0	LICK	5400	5400	
P73b	04/2002		LICK	3600	3600	
P74a	06/2006	2.0	LICK	5400	5400	
P74b	06/2006	2.0	LICK	3600	3600	
P75a	06/2006	2.0	LICK	3600	3600	
P75b	06/2006	2.0	LICK	4500	4500	
P76b	06/2006	2.0	LICK	2700	2700	
P77a	04/2004	0.7	A1,C4	1000	1000	
P77a	06/2006	2.0	LICK	6000	6000	
P77b	06/2006	2.0	LICK	6000	6000	
P78a	06/2006	2.0	LICK	3600	3600	
P79a	06/2006	2.0	LICK	6000	6000	
P79b	06/2006	2.0	LICK	6000	6000	
P80a	06/2006	2.0	LICK	2800	2800	
P80b	04/2005	2.0	LICK	2900	2900	
P81a	06/2006	2.0	LICK	6000	6000	
P81b	06/2006	2.0	LICK	4600	4600	
P82a	04/2004	0.7	A1,C4	3602	3602	
P116a	10/1998		D1			4
P116b	10/1998		D1			9
P117a	12/1994 ³		D2			18
P117b	12/1994 ³		D2			17
P118a	06/1995		D3			17
P118b	06/1995		D3			13
P118c	06/1995		D3			21
P119a	10/1998 ⁴		D4			8
P119b	10/1998 ⁴		D4			26
P120a	10/1998 ⁴		D4			19
P120b	10/1998 ⁴		D4			18

¹ S/N measured at 3800 Å.² S/N measured at 6500 Å.³ Also 1995 Jan 25.⁴ Also 1999 June 16 – 17.

which in practice means velocity separations of $< \text{FWHM}$ of the spectrum, we select a single redshift for all the lines. We do not average the velocities of the components, but rather we seek to identify a single component, typically that with the largest column density. If all the lines are single components, we chose the z_{abs} of the line that is the best defined and most like a single Voigt profile. If we see multiple components we take the z_{abs} from the strongest component, and when we see many ions each with components we choose the ion with the least components and the location of the highest optical depth.

In Table 5 we list the 691 metal line redshift systems that we found, including 34 that we will classify as BAL. We give their z_{abs} values, the ions we saw and the rest frame equivalent widths W_{rest} values for the stronger lines in the doublets; $\lambda 1548.19$ for C IV, $\lambda 1238.82$ for N V, and $\lambda 2796.35$ for Mg II. We list the W_{rest} for C IV if N V is also seen. We give W_{rest} for 587 non-BAL systems, less than the 657 total number of non-BAL systems, since we did not measure any lines for some systems because of low SNR or lack of C IV, N V and Mg II. We also list under the heading W_{pm} the approximate minimum W_{rest} value that we could have seen in the partner spectrum at that redshift and for the same ion, where a value of -1 means that that ion could not be seen and hence there is a significant chance that the system

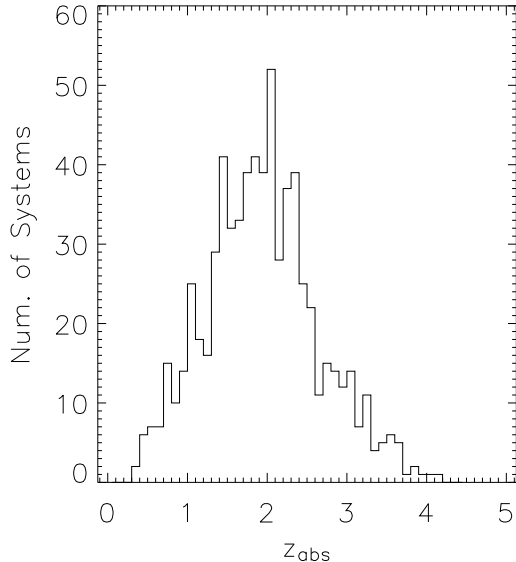


Figure 4. Distribution of all z_{abs} values in bins of size 0.01.

would not be detected in any ions. The list is in order of z for each pair, including the z_{em} values, to make it easier to see coincident redshifts.

In Fig. 4 we show the distribution of the z_{abs} values, which is very broad from 0.2 to 4.0 with a mode of 2.0.

The effective mean FWHM of our sample is near 170 km s^{-1} , although the spectra range from $83 - 281 \text{ km s}^{-1}$. The mean FWHM value from Table 3 weighted by the number of QSOs with spectra of each spectral resolution of 173 km s^{-1} . In Table 3 the N parameter gives the number of spectra with each resolution. We multiply these numbers by two for all setups where one rather than two setups are quoted for that QSO (D1, D2, D3, D4, SDSS and Lick). This mean is larger than the effective FWHM value because we expect to see more absorption systems in spectra with smaller FWHM values. In Fig. 5 we show the distribution of the separations of the absorption systems in individual lines of sight. We see only two pairs of systems with separations of $< 200 \text{ km s}^{-1}$, consistent with an effective resolution of near 170 km s^{-1} .

In Table 5 we mark the 34 systems that we consider to be broad absorption line BAL, because they show strong wide C IV lines. We arbitrarily choose to call BAL all systems with a total rest frame equivalent width for 1548 and 1550 of C IV $W_{\text{rest}}(\text{C IV}) > 5 \text{ \AA}$. We find that 32 of the QSOs contain one or more BAL systems. We will present separate analysis for the BAL and other systems because they are located near to their QSOs and not at the distance suggested by their z_{abs} . We exclude the BAL systems from our main analysis.

In Table 6 we list the number of times that we see each ion, N_{tot} , and the fraction of the absorption systems f_{tot} that show each ion. These distributions resemble those seen in other samples, such as Table VI of Barthel et al. (1990). However, we see fewer ions per system, and hence fewer instances of most of the ions than Milutinovic et al. (2007) saw in high resolution HST spectra of systems at $z_{\text{abs}} \simeq 1$.

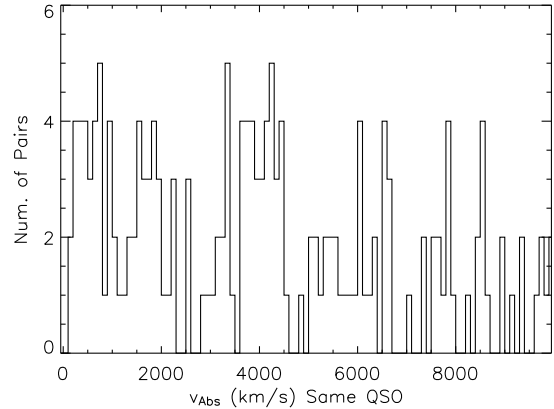


Figure 5. Histograms that show the distribution of redshift differences of absorption systems in individual QSOs. We include associated absorbers and use bins of 100 km s^{-1} .

In addition to the BAL systems, we expect that other systems, especially those with $z_{\text{abs}} \sim z_{\text{em}}$ will be intrinsic to the QSOs and not at the distances from the QSOs implied by their z_{abs} values (Misawa et al. 2007; Ganguly & Brotherton 2007). We make the following definition to help isolate such systems.

- **Associated absorbers** are at velocities $< 3000 \text{ km/s}$ in the frame of the z_{em} value of their QSOs.

We will explicitly state when we include or exclude associated systems from the samples that we analyse.

5 ANALYSIS OF NON-BAL METAL LINE ABSORPTION SYSTEMS

In this section we examine the distribution of the absorbers relative to each other and relative to the emission redshifts. We look for correlations along the individual sight lines and especially between the sight lines. We work in both redshift and velocity along the line of sight. We will see that many of the systems have $z_{\text{abs}} \sim z_{\text{em}}$, and we will establish that we see significant correlation between absorbers in the paired sight lines and between absorbers in one sight line and the z_{em} in the other sight line.

Many of our results on the distribution of the absorption and emission redshifts are shown in the five panels of Fig. 6 and the related panels of Fig. 7 that we will discuss one by one, and in comparison. The panels of Fig. 7 are closeups of the panels from 6, using the relative velocity instead of redshift differences. The bin size is 5 times smaller in Fig. 7 for $z = 2$. We include QSOs with BAL absorption, because a large fraction of the QSO groupings, 29/140, show one or more BAL systems; but we exclude the BAL systems themselves.

5.1 Absorbers Distributed Along Individual Lines of Sight

In Fig. 6(a) we show how the absorbers are distributed relative to the z_{em} of their QSO. For each absorption system we

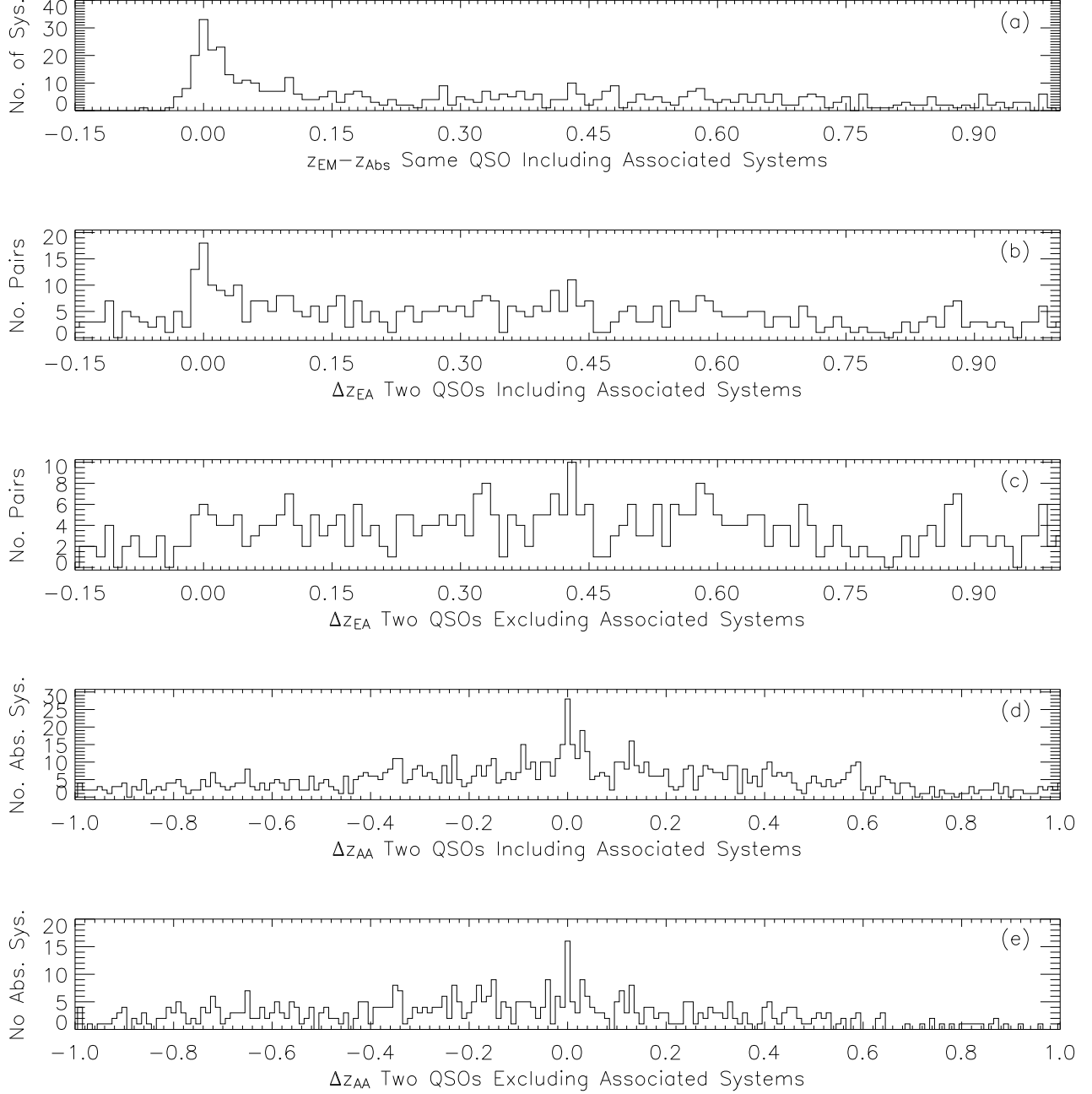


Figure 6. Histograms that show the distribution of redshift differences. The top panel (a) shows the distribution of the z_{abs} values from the z_{em} of the same QSO. The distributions in the remaining four panels all use one redshift from each of the pair of QSOs. The 2nd and 3rd panels (b) and (c) take a z_{em} value from one QSO in a pair, and a z_{abs} value from the other QSO. The 4th and 5th panels (d) and (e) take one absorber from each QSO. In the 2nd and 4th panels use all z_{abs} values, while the 3rd and 5th panels use subsets that exclude all absorbers within 3000 km s^{-1} of their QSOs z_{em} value. All bins have a width of $\Delta z = 0.01$, approximately 1000 km s^{-1} for QSOs at $z = 2$.

plot $z_{\text{em}} - z_{\text{abs}}$, where both redshifts are for the spectra of the same QSO. We see approximately 7 times more systems with $z_{\text{abs}} \simeq z_{\text{em}}$ compared to $0.15 < (z_{\text{em}} - z_{\text{abs}}) < 0.3$. The excess is conspicuous at $z_{\text{em}} - z_{\text{abs}} < 0.05$ ($5,000 \text{ km/s}$ for $z = 2$) and continues with lower amplitude to $z_{\text{em}} - z_{\text{abs}} > 0.1$ ($10,000 \text{ km s}^{-1}$ at $z = 2$).

Fig. 7(a) shows the same data as Fig. 6(a) but in terms

of velocity v_{abs} of the absorption system relative to the z_{em} of its QSO,

$$v_{\text{abs}} = c \times \frac{(1 + z_{\text{em}})^2 - (1 + z_{\text{abs}})^2}{(1 + z_{\text{em}})^2 + (1 + z_{\text{abs}})^2}, \quad (5)$$

where absorbers that appear to be falling into the QSOs have negative velocities. The v_{abs} values are approximately

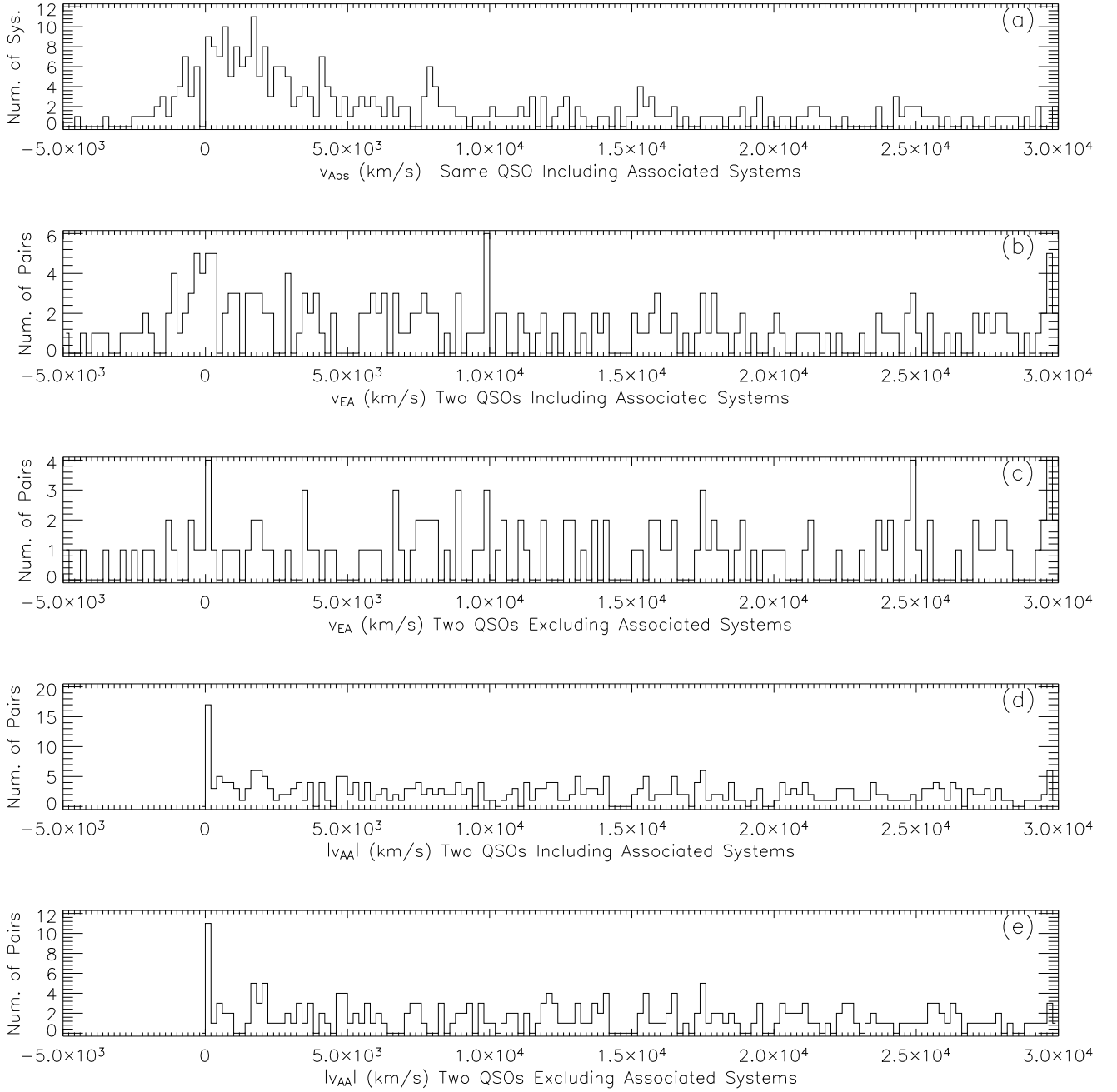


Figure 7. As Fig. 6 but using bins 200 km s^{-1} wide.

uniformly distributed from $0 - 2000 \text{ km s}^{-1}$, and the distribution is centred at approximately $v_{abs} \sim 1300 \text{ km s}^{-1}$, and not at $v_{abs} = 0$.

The excess absorbers with $z_{abs} \sim z_{em}$ is similar to that reported by Weymann et al. (1981) for a sample like our that does not employ an equivalent width cutoff. The velocity range $-4000 < v_{abs} < 4000 \text{ km s}^{-1}$ includes 42% of the Weymann et al. (1981) sample of C IV systems and 50% of our mixed absorption systems. Samples that contain only lines with W_{rest} exceeding some fixed minimum show much smaller excesses (Fig. 3 of Young et al. (1982) and Fig. 2a of Sargent et al. (1988)) because they exclude the additional

absorption lines that are easiest to see in the regions with the highest SNR, especially in and near to the C IV emission line.

5.2 Emission redshift errors and “infalling” Absorbers

Some QSOs show absorption with z_{abs} larger than their z_{em} with $v_{abs} > 1000 \text{ km s}^{-1}$. Peculiar velocities will account for many of the smaller “infall” velocities, but not the largest ones (Sargent et al. 1982). We believe that when we see

Table 5. The 619 Metal Lines Absorption Systems in the spectra of the 310 QSOs. Definitions for the symbols given under Notes are in §5.2 for EA and EAV, §5.3 for AA and §9 for AAV and AAA. An “EA” for two redshifts means a coincidence between the emission redshift of one QSO and an absorber redshift in the partner QSO. An “AA” for two redshifts means a coincidence between two absorber redshifts, one in each QSO of a pair. We give 5 decimal places for the mean redshifts of absorption systems in the AA AAV and AAA coincidences, and 4 decimals for most other absorbers. Errors on redshifts are given in Table 9 discussed in §9 below. We comment on the AA coincident systems in the appendix. W_{rest} is the rest frame equivalent width for one of the stronger doublet lines (1548, 1238 or 2796) and W_{pm} is the minimum W_{rest} that we could have seen for the same line in the spectrum of the partner QSO at the same z . Here we give only the first few lines of the table which will be distributed electronically.

QSO	z	Ions or z_{em}	Notes	W_{rest}	W_{pm}
P1 a	0.9397	Mg II, Fe II		2.29	0.08
P1 b	1.0091	Mg II, Fe II		0.68	0.1
P1 a	1.1355	Mg II, Fe II		1.59	0.10
P1 b	1.4267	C IV, Mg II		0.68	0.15
P1 a	1.541	Mg II		0.31	0.20
P1 b	1.7244	H I, C II, C IV, Si II, Si III, Si IV, Al II, Al III, Mg II, Fe II		0.86	0.15
P1 b	1.7584	C IV		0.39	0.15
P1 b	1.85837	H I, C IV, Si IV	AAA21	0.62	0.18
P1 b	1.866	z_{em}	EA1		
P1 a	1.86730	H I, N V ² , C IV	EA1 AAA21	0.38	0.10
P1 a	1.878	z_{em}			
P2 a	2.1142	H I, C IV, Si IV		0.63	0.10
P2 b	2.125	z_{em}			
P2 a	2.2193	H I, C IV, Si IV		1.05	0.10
P2 a	2.250	z_{em}			
P3 a	0.96767	Mg II, Fe II	AA1	1.29	0.10
P3 b	0.96770	Mg I, Mg II, Fe II	AA1	1.33	0.10
P3 b	1.0322	Mg II		0.26	0.10
P3 b	1.5483	C IV ²		0.34	0.30
P3 b	1.7854	H I, C IV, Si III, Si IV		0.50	0.25
P3 a	1.954	N V, C IV, Si IV	BAL	11.3	0.15
P3 a	1.970	z_{em}			
P3 b	1.976	z_{em}			

¹ W_{rest} value for C IV 1550 or N V 1242.

² A significantly blended absorption line.

Full version of this 11 page table is in the electronic version of the paper.

a large negative v_{abs} the z_{em} value is too small by about $-v_{abs}$. This idea due to Gaskell (1983) is credible because we know that large negative blueshifts of the C IV emission lines are common (Gaskell 1982; Tytler & Fan 1992; Richards et al. 2002). With this interpretation many of the absorbers at positive velocities relative to the QSO systemic redshift and the negatives v_{abs} values do not need special treatment, other than noting that the z_{em} values are too small.

The distribution of the velocities of the absorption systems in the frame of the QSOs give information on the z_{em} errors. In Fig. 7(a) we see only 15 systems from 310 QSOs at velocities $< 1000 \text{ km s}^{-1}$. This suggests that z_{em} errors

Table 6. Ions seen in absorption systems. We have not conducted a thorough search, and we only occasionally looked for ions such as Si III, C III with lines at rest wavelengths $< 1216 \text{ \AA}$.

Ion	N_{tot}	f_{tot}	N_{BAL}	N_{AA}	f_{AA}	N_{EA}	f_{EA}
C IV	416	0.602	32	21	0.656	16	0.89
H I	256	0.370	27	5	0.156	14	0.78
Mg II	192	0.278	0	12	0.375	0	0.00
Si IV	117	0.169	11	3	0.094	4	0.22
Si III	114	0.165	0	2	0.063	2	0.11
N V	106	0.153	26	1	0.031	4	0.22
Fe II	106	0.153	0	7	0.219	0	0.00
Si II	56	0.081	0	3	0.094	1	0.06
Al II	45	0.065	0	2	0.063	2	0.11
C II	44	0.064	0	2	0.063	1	0.06
O VI	31	0.045	16	0	0.000	0	0.00
Al III	17	0.025	0	1	0.031	2	0.11
O I	10	0.014	0	0	0.000	0	0.00
Mg I	6	0.009	0	1	0.031	0	0.00
C III	2	0.003	0	0	0.000	0	0.00
Ca II	1	0.001	0	0	0.000	0	0.00

are typically $< 1000 \text{ km s}^{-1}$. We say more about z_{em} errors below.

5.3 Redshift ordering of absorption and emission redshifts

The remaining panels in Fig. 6 all compare one redshift from each QSO of a pair. We will discuss pairings of absorbers with emission redshifts first, then separately, absorbers with absorbers.

We provide two figures to help visualise the arrangement of the redshifts. In Fig. 8 we show the emission and absorption redshifts in the first 24 QSO pairs. In Fig. 9 we give a sketch to help clarify the possible arrangements of the z_{em} and z_{abs} values. When we add an absorber to Fig. 9 we can distinguish 4 binary choices:

- Does the pair of QSOs have similar z_{em} ?
- Is the absorber in the QSO with the higher z_{em} ?
- Is the z_{abs} less than the partner QSO’s z_{em} ?
- Is the absorber associated with its QSO?

Not all of these 16 combinations are possible, but those that are can populate and can explain much of the shape of the distributions that we will now discuss.

5.4 Absorption in one QSO near the Emission Redshift of the Partner: EA

Fig. 6(b) shows the distribution of Δz_{EA} values that we define as

$$\Delta z_{EA} = z_{em1} - z_{abs2}. \quad (6)$$

This panel shows the tendency of absorbers in the spectrum of one QSO to lie near the emission redshift of the other QSO.

We do not place any constraints on the relative values of the z_{em} of the paired QSOs, hence we see a large number of highly negative Δz_{EA} values, most of which are of no interest to us. If there were no peculiar velocities, and the QSO

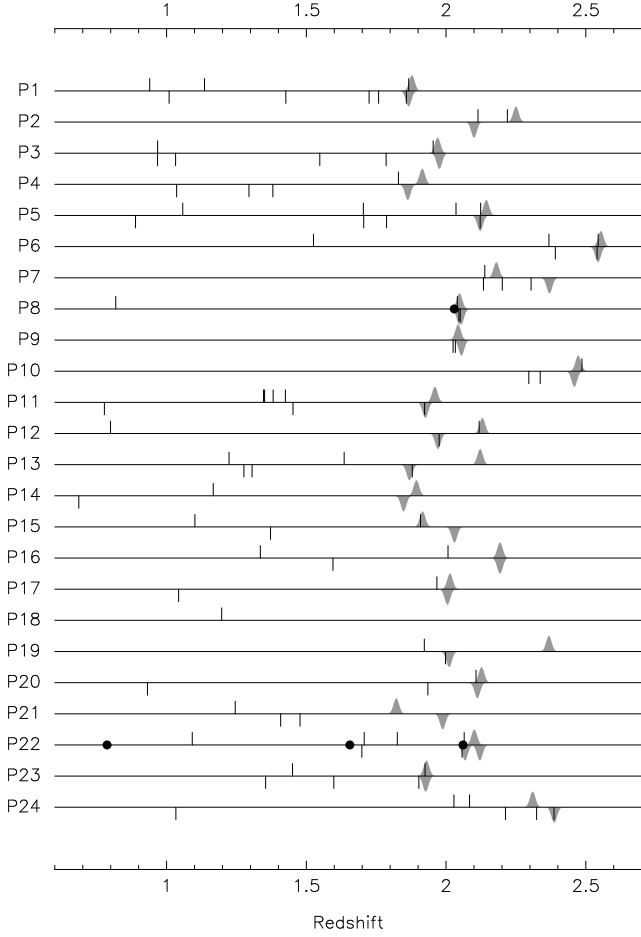


Figure 8. The absorption systems and z_{em} from Table 5 for the first 24 QSO pairs. The z_{em} is shown as a gaussian grey region with $\sigma_z = 0.01$ (1000 km s^{-1} at $z = 2$). The upwards tick marks represent the redshifts in the ‘a’ QSO and the downward tick marks represent the redshifts in the ‘b’ QSO. For the triples P8 and P22 the filled black circles represent the absorption redshifts in the ‘c’ QSO, ‘c’ z_{em} are shown below the line. P18a and P18b have $z_{\text{em}} > 2.7$ and one system has $z_{\text{abs}} < 0.6$. The two highest z_{abs} in P1a (above the line) is coincident with the z_{em} of P1b below the line (EA1). The lowest two z_{abs} in P3 are coincident (AA1). P5 has coincident absorbers at 1.7 (AA2) and 2.2 (AAV17). In P6 absorbers at 2.54 are coincident with each other (AAA23) and with the z_{em} of the partner QSO (EA3, EAV19). P7 has a coincident absorbers at 2.14 (AA4). The triplet P8 has multiple coincidences near the z_{em} values. The triple P22 has a wide coincidence at 1.7 (AAV18) and multiple coincidences near the 3 z_{em} values. The absorber in P23a at 1.9 is coincident with the z_{em} of P23b.

emission lines gave the systemic redshifts of the QSOs (that of the host galaxies), then all cases with $\Delta z_{EA} < 0$ would be of no interest because they would come from absorption systems in the background QSOs which are at higher redshift than the foreground QSO. However, we expect peculiar velocities are frequently a few hundred km s^{-1} . If the z_{em} values for a pair of QSOs are very similar, and we allow for measurement errors, the light from the QSO showing the z_{abs} is passing through at least part of the volume around the other QSO.

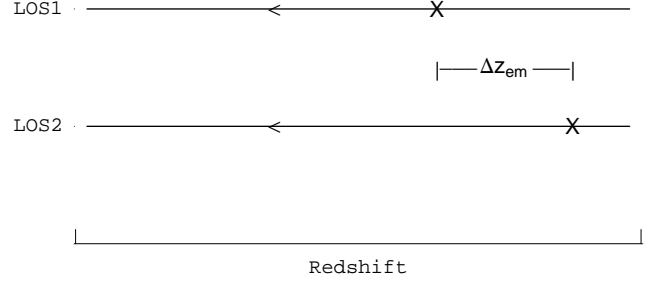


Figure 9. Visualisation of the range of possible and most common redshift differences. The two horizontal lines represent the lines of sight to a pair of QSOs, with light travelling to the left and redshift increasing to the right. The X’s represent the emission redshifts. In Fig. 3 we saw that the z_{em} values of the pair are often similar. In Fig. 6(a) we saw the distribution of z_{abs} values relative z_{em} values. It is also common for z_{abs} values to be similar to the z_{em} values. If we take z_{em} from LOS1 and compare to a z_{abs} value from LOS2 which is at $z_{\text{em}2} + 0.05$, then the Δz_{EA} value is negative: $z_{\text{em}1} - z_{\text{em}2} - 0.05$. Similar arrangements may explain why the Δz_{EA} distribution in Fig. 6(b) is asymmetric around zero.

Fig. 6(b) shows how the absorbers in one QSO are distributed relative to the z_{em} of the partner QSO. We see 18 absorbers in the bin centred at zero, at $-0.05 < \Delta z_{EA} < 0.05$, which is $\pm 500 \text{ km s}^{-1}$ at $z = 2$. Since the errors on the z_{em} values are likely in the range $400 - 800$ or more km s^{-1} we expect any clustering of absorbers next to a QSO to be spread over the three bins centres on zero. There at $-0.015 < \Delta z_{EA} < 0.015$ we see about 23 pairings in excess of the background level at larger Δz_{EA} values. This excess is highly significant.

In Fig. 7(b) we use velocity v_{EA} instead of redshift, where

$$v_{EA} = c \times \frac{(1 + z_{\text{em}})^2 - (1 + z_{\text{abs}})^2}{(1 + z_{\text{em}})^2 + (1 + z_{\text{abs}})^2}, \quad (7)$$

and the emission and absorption redshifts are from the different QSOs in the pair. Fig. 7(b) shows that the excess extends over approximately $\pm 400 \text{ km s}^{-1}$ and perhaps farther; the extend is not well determined in this small sample when we do not have definite model to test. We fit the distribution with the sum of a straight line plus a Gaussian. The Gaussian that represents the excess has a mean near -150 km s^{-1} (consistent with zero) and a dispersion of approximately 525 km s^{-1} .

Both the dispersion and the mean are of physical interest. The dispersion gives an upper limit on the random errors in the z_{em} values of the QSOs that show systems with $z_{\text{abs}} \sim z_{\text{em}}$. In addition to the z_{em} errors, the dispersion includes the pair-wise random velocity difference of the absorbing galaxies relative to the QSOs galaxy. From references that we discuss in §7.7, this pair-wise velocity is likely in the range $200 - 400 \text{ km s}^{-1}$ if the QSOs are in blue galaxies and $500 - 800 \text{ km s}^{-1}$ if they are in red galaxies. Hence much of the dispersion we measure can be from pair-wise velocities leaving little for the z_{em} errors. If we know the z_{em} errors we should be able to decide if the QSOs are in

red or blue galaxies. We will see below that the absorbers far from QSOs are typically in a population with unusually small pair-wise velocity dispersions.

The mean velocity of the excess of absorbers around the partner QSOs is an interesting new way to measure the difference of the z_{em} values from the systemic redshifts. At least, this is true if the absorbers are symmetrically distributed in velocity relative to the QSO systemic velocity. We will discuss below why absorbers would be preferentially behind the QSOs if QSOs are luminous for ~ 3 Myr and their UV radiation destroys absorbers.

Fig. 6(c) repeats the panel above, but now excluding all associated systems, those within 3000 km s^{-1} of the z_{em} . The excess near $\Delta z_{EA} = 0$ has gone leaving an approximately constant number of pairings at $-0.015 < \Delta z_{EA} < 0.6$.

Fig. 7(c) shows v_{EA} excluding associated absorbers. While there are more pairs in the $v = 0 - 200 \text{ km s}^{-1}$ bin than in most other bins, two other bin also show 4 pairs, hence from an *a posteriori* perspective, where we do not know which velocity to consider, this is not a significant excesses. However, we have *a priori* reasons to look for the excess in the two bins covering $\pm 200 \text{ km s}^{-1}$. Here we see 5 coincidences where we expect 1.5, from the 18 seen at $200 - 5000 \text{ km s}^{-1}$. The probability of 5 or more is 1.9%.

We distinguish two possible explanations for the excess pairings of absorbers with z_{abs} similar to the z_{em} of the partner QSO.

1) **Normal Line of Sight (los) associated absorbers.** These are the excess C IV absorbers at $v_{EA} < 3000 \text{ km s}^{-1}$ seen in individual lines-of-sight, and seen in Figs. 6(a) and 7(a). The excess pairings that we see in Fig. 6(b) may be normal los associated absorbers that are selected because the QSO pairs often have very similar z_{em} values.

2) **Transverse associated absorbers.** These are a new type of absorption connected to and near to the QSOs. Their existence has already been established by the 4 Mg II pairings reported by Bowen et al. (2006) and probably also for LLS found by Hennawi & Prochaska (2007). They are different because most of them are not seen along the line of sight to individual QSOs. The transverse absorbers know with more precision the systemic velocity of the other QSO, that giving the z_{em} , than do its own los associated absorbers. The transverse absorbers might arise in the host galaxy, but considering the sky separations, they are more far likely from galaxies clustered around the QSO. Chelouche et al. (2007, Fig. 8) shows a possible arrangement of the transverse absorbers.

We suspect that many of the excess EA pairings at $\Delta z \approx 0$ are transverse associated absorbers. The excess of EA absorbers Fig. 7(b) appear to be more concentrated around zero than are the normal los associated absorbers in Figs. 7(a). The four absorbers that remain at $v=0$ in Figs. 7(c) when we have removed the associated absorbers hint the same.

Several pieces of weak evidence suggest that the transverse associated absorbers are not just a subset of the los associated absorbers. For Mg II systems and LLS the arguments given by Bowen et al. (2006) and Hennawi & Prochaska (2007) are that the transverse absorbers are more common than the los associated. We can not claim this for

the Mg II and C IV systems we study here because we do not have a complete sample with a defined W_{rest} limit. Indeed Figs. 7(a) and (b) show that there are more los associated systems in our sample per km s^{-1} than there are transverse QSO-absorber coincidences. However we do expect that many of the transverse Mg II and C IV systems that we study are similar to the Mg II and LLS studied by Bowen et al. (2006) and Hennawi & Prochaska (2007), and hence their arguments should apply our sample.

We suspect that we would also see a difference in the v_{EA} of the los and transverse associated systems if we had a complete sample of absorbers. This complete sample would need to come from a much larger total sample than we have here, since complete samples tend to contain only a fraction of all systems seen. Sargent et al. (1988, Fig. 2a) shows that the excess of los associated systems extends over about $\pm 2000 \text{ km s}^{-1}$, a larger range than the $\pm 400 \text{ km s}^{-1}$ indicated for the coincidences in Figs. 7 (b), however this comparison is insecure because of the small samples and differences in the ways in which z_{em} values are measured. Sargent et al. (1988) measured z_{em} values using laboratory rest frame wavelengths for emission lines of H I, N V, Si IV+OIV], C IV, and their QSOs are significantly more luminous leading to less distinct emission lines, factors that might lead to larger errors in the z_{em} values and hence a wider range of v_{EA} for the excess C IV absorbers in their complete sample.

We now introduce a definition to simplify our discussion.

- **EA** (emission-absorption) coincident absorbers are close to the emission redshift of the partner QSO, with $-0.005 < \Delta z_{EA} < 0.005$. We include associated systems. We do not require that the absorber is in the QSO with the higher z_{em} value.

In Table 5 we mark with EA1, EA2,.. the 18 pairings of z_{em} and z_{abs} values and we give notes on each in the appendix. In Table 7 we list some properties of these 18 EA coincident absorbers, including the separation in Mpc in the plane of the sky and in velocity. The triple P8 includes 3 EA pairings, one an absorber in P8a with QSO P8c, and two from absorbers in P8b paired with QSO P8a. The other EA pairings are each from a different pair of QSOs.

For 2 of the 18 EA pairings (P116 and P119) the absorber is in the QSO with the lower z_{em} value. For P116 the absorber is at $v_{\text{abs}} = -3,435 \text{ km s}^{-1}$ and $v_{EA} = 13 \text{ km s}^{-1}$. If both z_{em} values have negligible errors, this can not be a physical coincidence. However, if the z_{em} value of the QSO showing the absorber is too low by $\sim 3,400 \text{ km s}^{-1}$, depending on peculiar velocities, we may still have a physical coincidence. P119 is similar but less extreme with $v_{\text{abs}} = -444 \text{ km s}^{-1}$ and $v_{EA} = 266 \text{ km s}^{-1}$. In a third case, EA18, the absorber is in the QSO with the higher z_{em} value, and the z_{abs} is larger than the z_{em} of its QSO by $v_{\text{abs}} = -239 \text{ km s}^{-1}$. These coincidences between absorbers apparently “infalling” into QSOs with the z_{em} values in partner QSOs strengthen our belief that the systemic redshifts for these two QSOs, and by implication most QSOs with absorbers at large negative velocities, are significantly higher than their z_{em} values.

We define a second type of coincidences that explore a larger range of separations.

• **EAV coincident absorbers** (V for velocity) are like EA coincidences but they have $v_{EA} < 1000 \text{ km s}^{-1}$ instead of $-0.005 < \Delta z_{EA} < 0.005$.

In Table 7 we list 12 EAV coincidences.

Examining Table 7, we see contradictory evidence as to whether we see the transverse absorbers along a single line-of-sight. Arguing in the negative, both Bowen et al. (2006) and Hennawi & Prochaska (2007) claim that they see far more transverse absorbers than los associated ones. Our spectra also show no excess of los associated absorbers confined to $v_{abs} < \pm 400 \text{ km s}^{-1}$ in Fig. 7(a). For example, if 20% of QSOs showed absorption within $\pm 400 \text{ km s}^{-1}$ of their z_{em} value, from the population of transverse absorbers that happen to be in the los, then we would see 62 excess absorbers at these v_{abs} values where we see only 23, which is no excess compared to $400 < v_{abs} < 2000 \text{ km s}^{-1}$.

However, examining Table 7 we see that many of the absorbers in the EA and EAV coincidences have small v_{abs} values that presumably place them very close to their QSOs, where we have just argued we do not typically see excess absorption. The distribution of the v_{abs} values of the EA and EAV coincidences seems similar to that for absorbers as a whole. We are surprised to see absorption in a QSO coincident with the z_{em} of the partner QSO, when the absorber and the two QSOs are all have similar redshifts. In Fig. 9 imagine that both QSOs are embedded in a spherical halo of (transverse) absorbers that also overlaps the other line of sight. We see excess absorption in LOS2 at the z_{em} of QSO1, but no excess in LOS1 due to its own halo of absorbers. How can we see transverse absorption associated with the partner QSO1 at small v_{abs} values, given that we do not often see such absorption, as similar small v_{abs} values, in either individual line-of-sight? We expect that whatever prevents us from seeing the transverse absorbers along the line-of-sight to most individual QSOs would also prevent us from seeing them around the partner QSO when the similarity of the z_{em} values places them at small v_{abs} values. This is a mystery.

5.5 Absorption in one QSO near Absorption in the Partner: AA

We now discuss absorber-absorber coincidences, where one absorber comes from each of a pair of QSOs. Fig. 6(d) shows the distribution of Δz_{AA} which we define as

$$\Delta z_{AA} = z_{abs1} - z_{abs2}, \quad (8)$$

where one absorber is from each QSO in a pair. We arbitrarily chose which QSO is 1 for the subtraction of the absorption redshifts and hence the signs have no physical meaning. However, the QSO ordering in the main table is not random, and hence the Δz_{AA} distribution has a clear, unintended asymmetry. Some of the peak near the $\Delta z_{AA} = 0$ value again comes from the tendency of the two QSOs in a pair to have similar z_{em} values and the excess of absorbers with $z_{abs} \simeq z_{em}$. The counts are low but hint that the excess extends over several bins, perhaps covering a range of Δz similar to that of the excess of absorbers in the individual sight lines in the top panel.

Fig. 6(e) is like panel 6(d), but now excluding the associated systems from both QSOs. The excess remains and

Table 7. EA Emission-absorber coincidences. The first column gives the QSO that contributes the z_{em} value (listed in Table 5). The letter in front of the z_{abs} in the second column identifies the QSO that gives the z_{abs} value. We designate a pairing EA if $-0.005 < \Delta z_{EA} < 0.005$, otherwise it is EAV which means that $\Delta z_{EA} > 0.005$ and $v_{EA} < 1000 \text{ km s}^{-1}$. Velocities are in (km s^{-1}) and v_{abs} is the velocity of the absorber in the frame of the z_{em} value of its QSO. The separation of the two sight lines in the plane of the sky is the b value in proper Mpc.

QSO em	QSO z_{abs}	Pair	v_{abs}	v_{EA}	b (Mpc)	W_{rest} (Å)
P26b	a 1.8896	EAV22	-815	-919	0.2114	0.80
P26b	a 1.89084	EAV23	-686	-790	0.2114	0.80
P64a	b 2.00451	EAV24	26886	-651	2.1137	0.54
P8c	b 2.04602	EAV20	785	-593	0.9202	0.77
P147a	b 2.3708	EAV28	-2484	-517	0.9911	0.28
P147b	a 2.34871	EAV29	1456	-512	0.9927	
P94a	b 3.2081	EAV25	42063	-363	1.9958	
P28a	b 2.1686	EA9	1831	-341	1.5089	2.72
P153a	b 2.5178	EA18	-239	-324	1.1315	0.75
P8a	b 2.05115	EA6	280	-310	1.1069	0.52
P6b	a 2.54697	EA3	594	-251	0.5880	0.17
P43b	a 2.0665	EA12	13151	-147	0.4292	0.32
P1b	a 1.8673	EA1	1117	-136	0.7556	0.38
P123a	b 2.25927	EA17	12762	-117	2.1715	0.40
P5b	a 2.12306	EA2	2005	-102	0.5075	0.28
P116b	a 1.79988	EA15	-3435	13	0.6928	2.00
P38b	a 1.91658	EA11	15366	43	0.1869	
P8c	a 2.03912	EA4	875	87	1.8363	0.16
P36a	b 1.96688	EA10	32073	113	0.3425	
P8a	b 2.04602	EA5	785	195	1.1072	0.77
P23b	a 1.9249	EA8	523	215	0.4211	0.14
P95c	b 3.14571	EA14	1825	238	2.2246	0.69
P119a	b 3.22625	EA16	-444	266	0.4713	0.57
P22b	a 2.06449	EA7	3553	343	1.3093	1.25
P82b	a 1.98055	EA13	2151	347	1.4410	0.58
P153b	a 2.50758	EAV30	549	634	1.1325	
P22b	c 2.05997	EAV21	5924	786	1.2880	0.16
P141a	b 4.1160	EAV27	3001	845	2.0000	2.85
P6a	b 2.54327	EAV19	62	907	0.5883	0.26
P121b	a 2.2882	EAV26	347	984	2.1815	1.32

is now restricted to the 16 systems in the single bin at $-0.005 < \Delta z_{AA} < 0.005$ ($\pm 500 \text{ km s}^{-1}$ at $z = 2$). We now make a definition to simplify our discussion.

• **AA** (absorption-absorption) coincident systems have a partner in the paired QSO with $-0.005 < \Delta z_{AA} < 0.005$. They exclude associated systems, those with $v_{abs} < 3000 \text{ km s}^{-1}$ relative to their QSOs z_{em} value.

The 16 AA coincident systems constitute a highly significant detection of the correlation of metals between the paired sight lines. A straight line fit to the distribution of the absolute Δz_{AA} values in Fig. 6(e), excluding absolute values < 0.005 , gives $y = -0.037x + 4.645$ absorption systems per $\Delta z = 0.01$. Hence we expect 4.645 system pairs with $-0.005 < \Delta z_{AA} < 0.005$. The Poisson probability of observing ≥ 16 given an expectation of 4.645 is 3×10^{-5} . The 16 pairings are a factor of $16/4.645 = 3.44$ above the expected number of chance pairings. We give notes on each of these 16 systems in the appendix, and we label and number them with AAXx in Table 5.

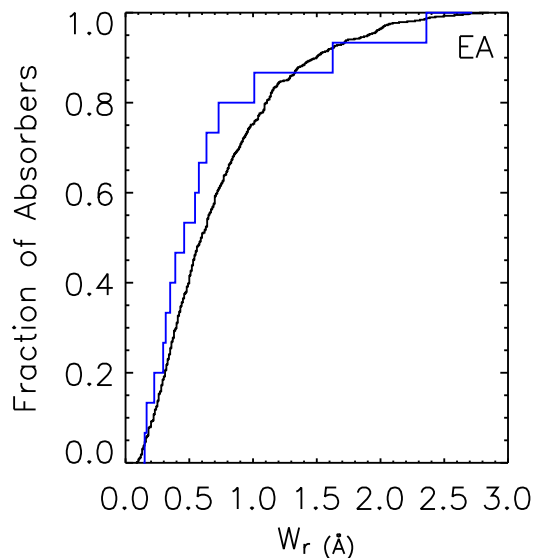


Figure 10. Cumulative distribution of the rest frame equivalent width of 572 of the non-BAL absorption lines from Table 5, excluding the 15 EA coincidences but including associated systems (smoother black line). We show separately the W_{rest} values of 15 of the EA coincidences (stepped blue line).

Fig. 7(e) shows the absolute values of v_{AA} values, excluding all associated systems. The excess that we saw in terms of redshift is still present, and now gives 12 pairs in the first bin covering $0 < v < 200 \text{ km s}^{-1}$. The peak at $v = 0$ is largely confined to this first bin and is clearly highly significant.

6 REST FRAME EQUIVALENT WIDTHS AND IONS SEEN IN THE COINCIDENT SYSTEMS

In this section we see that both the AA and the EA coincident systems are unremarkable spectroscopically. Rather they seem typical of all systems that we see.

In Fig. 10 we show the cumulative distribution of the W_{rest} values of the main ions of the non-BAL absorption systems listed in Table 5. There is a surprisingly wide range of W_{rest} values from $0.1 - 2.8 \text{ \AA}$, with a mean near 0.74 \AA . We show separately the W_{rest} distribution for 15 of the 15 EA coincident absorbers. We did not measure W_{rest} values for the other 3 EA systems for various reasons. The EA systems tend to have smaller W_{rest} values than the sample as a whole, but the maximum difference of 0.208 is not significant according to the KS test.

In Fig. 11 we compare the AA systems with the sample from which they were selected. Like the EA absorbers, the AA coincident absorbers also include a larger fraction of smaller than average W_{rest} values. The maximum difference between the two distributions is 0.243 near $W_{rest} = 0.41 \text{ \AA}$. This difference is barely significant at the 95% level.

We are not surprised that the coincident absorbers have smaller W_{rest} values, since higher quality spectra that can

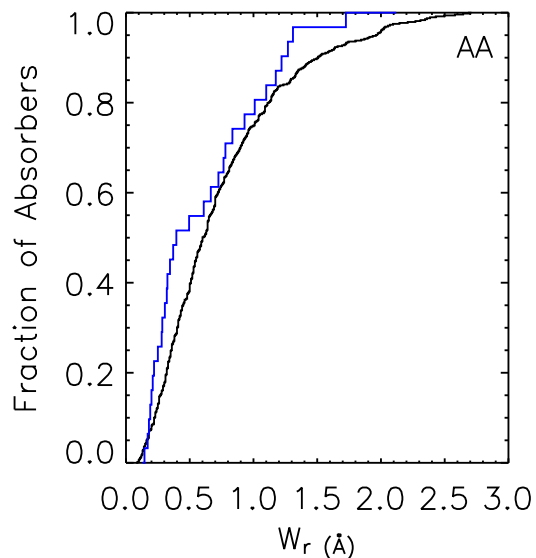


Figure 11. Cumulative distribution of the rest frame equivalent widths of the AA systems (stepped blue line) and the sample from which they were drawn (smoother black line). We use the W_{rest} values from Table 5 of the main ions in the 452 non-BAL absorption systems, excluding associated systems and excluding the 32 absorption systems from the 16 paired AA coincidences. This figure differs from Fig. 10 in that associated absorbers are now removed and the samples are divided by whether an absorber is an AA rather than EA coincidence.

reveal smaller W_{rest} values will tend to have more systems per spectrum and hence a larger chance of showing coincidences. They will not all have the smallest W_{rest} values, because too few spectra could show such values.

6.1 Ionisation of the Coincident Systems

In Table 6 we list the frequencies of ions in the EA and AA systems. We see nothing unusual about the AA coincidences. Most AA coincidences show the same ions in both systems. In only two cases (AA5, AA15) do coincident systems have no ions in common. The AA coincidences show C IV 13 times and Mg II 8 times, and 11 of the AA systems show other ions, most often Fe II, but also Mg I, Si III, Si IV, N V, Al II and Al III.

The 16 of the 18 EA systems show C IV while the other two show Al II and Al III. They do not show Mg II or other lines with large rest frame wavelengths because the z_{em} values are too high for these lines to be in our spectra. We do not see any excess of N V, unlike Hennawi et al. (2006) who note that several of the LLS that they find near to QSOs exhibit N V, an ion rarely seen far from QSOs.

7 SPATIAL DISTRIBUTION OF ABSORBERS AROUND ABSORBERS

We now give a more detailed discussion of the absorber-absorber correlation, in both redshift and impact parameter in the plane of the sky. We see that the absorbers

are strongly correlated on scales < 0.6 Mpc. We detect the redshift-space distortion, in which peculiar velocities make the correlation elongated along the line of sight. We show that the peculiar velocities are low, much less than the velocities that Adelberger et al. (2005) see in the C IV and H I absorption from star forming Lyman break galaxies (LBGs).

In Table 8 we list the velocity separations for the 16 AA system pairs that we defined as all non-BAL systems with $-0.005 < \Delta z_{AA} < 0.005$, which is 500 km s^{-1} or a distance of 2.49 Mpc at $z = 2$. Of the 16 AA such systems, only AA12 has a velocity separation

$$v_{AA} = c \times \frac{(1 + z_{\text{abs1}})^2 - (1 + z_{\text{abs2}})^2}{(1 + z_{\text{abs1}})^2 + (1 + z_{\text{abs2}})^2}, \quad (9)$$

larger than 500 km s^{-1} , which somewhat less than the correlation length seen in individual sightlines for strong C IV and Mg II absorption systems (Young et al. 1982; Petitjean & Bergeron 1990; Scannapieco et al. 2006). We make two further definitions that expand upon the AA definition.

- **AAV coincident systems** (V for velocity) have $v_{AA} < 1000 \text{ km s}^{-1}$ but $|\Delta z_{AA}| > 0.005$, so that they were not listed as AA. As with the AA systems, we require that both absorbers be farther than $v_{\text{abs}} = 3000 \text{ km s}^{-1}$ from their QSO.

- **AAA coincident systems** (Associated Absorber-Absorber) have $v_{AA} < 1000 \text{ km s}^{-1}$ and one or both absorbers at $v_{\text{abs}} < 3000 \text{ km s}^{-1}$ from their QSO.

We find 4 AAV coincidences (AAV17 – 20) and 14 AAA coincidences (AAA21 – 34). We list them in Tables 5 and 8 and we describe some of them in the appendix. Seven pairs (P5, P6, P25, P31, P38, P42, P155) and two tripples (P8, P22) contribute two or more coincidences each.

7.1 Absorption Redshift Errors

We are especially interested in the errors on the absorption system z_{abs} values that happen to be close to another z_{abs} or z_{em} value. For each system listed in Table 8 we made optimised fits to the main absorption lines. We list the results in Table 9. For about 40% of these systems we have two or more ions per system. In those cases we calculate $\sigma(z)$, the standard deviation of the z that we measured for each ion. The mean $\sigma(z)$ is $23 \pm 4 \text{ km s}^{-1}$. We believe that this is representative of the internal errors on the z_{abs} values for systems showing one ion. For systems with two ions, we might attain errors smaller by a factor of up to $1/\sqrt{2}$. For approximately 10% of the systems the lines are blended in ways that make it hard to find a unique centre, and errors will be several times larger. When we compare to a z_{abs} value measured in the partner QSO we need to also account for systematic errors in the wavelength scales. We typically see the same ions in both spectra, and hence we are measuring the z_{abs} values at the same observed wavelengths. When these measurements are done with the same instrument and grating these external errors should be similar and hence they will have little effect on relative velocities. Otherwise the external errors may be some fraction of a pixel. We shall assume that our errors for a typical z_{abs} value are 23 km s^{-1} , noting that they will be several times larger in some cases, as seen from the large standard deviation of 19 km s^{-1} of the $\sigma(z)$ values in Table 9.

Table 8. The 34 absorber-absorber coincidence separations in order of velocity difference v_{AA} . In all cases one absorber is from each of a pair of QSOs. We label pairs of absorbers with $\Delta z_{AA} < 0.005$ as AA (16 cases), and those with $v_{AA} < 1000 \text{ km s}^{-1}$ as AAV (4 cases). When one or both system is within 3000 km s^{-1} of their QSO (v_{E1} or $v_{E2} < 3000$) we call them AAA (14 cases). The two letters after the pair number in the first column identify the two QSOs containing the absorbers. The first letter (e.g. P3b) refers to the v_{E1} value in the 3rd column, while the second letter refers to the v_{E2} value. Velocities are in km s^{-1} , and the redshift difference is in units of 10^{-5} . At $z = 2$, $\Delta z_{AA} = 10^{-5}$ corresponds to $v_{AA} \simeq c\Delta z_{AA}/(1+z) = 1 \text{ km s}^{-1}$. The last column shows the separation between the sight lines at the redshift of the absorbers in proper Mpc.

QSO ¹ pair	Label	v_{E1}	v_{E2}	Δz_{AA} (10^{-5})	v_{AA}	Sep. (Mpc)
P3ba	AA1	117487	116978	3.0	5	0.096
P7ba	AA4	21463	4098	9.0	9	0.544
P38ab	AA10	69880	55187	20	25	0.187
P31ba	AA9	70389	60783	26	32	0.858
P22cb	AAA27	5924	745	40	41	1.310
P31ba	AA8	119710	111093	36	53	0.815
P36ba	AAA30	32073	180	66	67	0.343
P155ba	AAA34	2097	2708	90	68	0.108
P25ba	AA6	64626	66842	54	70	0.126
P70ab	AA15	18124	31855	72	76	1.560
P155ba	AA16	24237	24829	102	84	0.111
P38ab	AA11	68229	53422	88	108	0.187
P5ab	AAA22	2005	26	133	128	0.507
P5ab	AA2	44888	42697	119	132	0.516
P44ab	AA14	76087	79820	100	140	0.382
P42ab	AA13	39010	66642	147	179	0.228
P83ba	AAA31	8135	1731	90	198	1.148
P25ba	AA7	49553	52112	192	238	0.128
P147ba	AAA32	-795	1456	316	283	0.993
P6ab	AAA23	594	62	370	313	0.588
P22ab	AAA29	3553	745	410	402	1.310
P6ab	AA3	202347	201643	231	442	0.468
P22ab	AA5	3553	5923	452	443	1.310
P22cb	AAA26	5924	1253	476	467	1.310
P125ab	AAV20	38663	39804	568	558	0.831
P42ab	AA12	78387	103869	445	621	0.222
P8ab	AAA25	875	785	690	680	1.836
P5ab	AAV17	10597	7701	802	792	0.510
P22ba	AAV18	38224	40523	784	870	1.326
P153ba	AAA33	-239	549	1022	873	1.132
P22ab	AAA28	3553	1253	928	910	1.310
P1ab	AAA21	1117	800	893	936	0.756
P31ba	AAV19	69457	60783	775	953	0.858
P8ac	AAA24	875	1048	959	961	1.836

¹ In order of velocity separation.

7.2 Impact parameters of AA coincidences

In Fig. 12 we see a highly significant tendency for the AA coincidences to be at unusually small separations. Of the 16 pairs, 6 are at < 0.2 , and 12 at < 0.6 Mpc, where as the mean separations of all systems is 1.3 Mpc. This is also seen in the histograms in Fig. 13. When we see absorption in one sight line, the probability of also seeing absorption with $\Delta z_{AA} < 0.005$ (approximately $v_{AA} < 500 \text{ km s}^{-1}$) in the partner sight line is high for small impact parameters and declines rapidly. We see 1 coincidences from 2 systems (50%)

Table 9. Redshift and velocity errors for 28 AA, AAV or AAA systems in order of pair number. We list only the ions we use to obtain the mean redshift in column 2 and the standard deviation of the two z_{abs} values in column 3. In column 4 we have converted the standard deviation of the z_{abs} values into velocity. The $\sigma(z)$ is in units of 10^{-5} . Velocities are in km s^{-1} .

QSO	z_{abs} mean	$\sigma(z)$ (10^{-5})	$\sigma(v_{AA})$ (km s^{-1})	Ions
P1a	1.86730	13	14	C IV N V
P1b	1.85837	26	27	C IV Si IV
P3a	0.96770	1.4	2.1	Mg II Fe II
P3b	0.96767	1.4	2.1	Mg II Fe II
P5a	2.03513	20	20	C IV C II
P5a	2.12306	7.2	6.9	C IV N V
P5b	2.04286	75	74	C IV Si III
P5b	2.12173	18	18	C IV Si IV
P6a	2.54697	17	14	C IV N V
P7a	2.13685	52	49	C IV Al II
P22a	2.06449	23	22	C IV Si IV
P22a	1.70703	6.0	6.6	C IV Si IV
P22a	1.69908	26	29	C IV Si IV
P22c	2.05997	44	42	N V Si III
P25a	1.30321	27	35	C IV Si IV
P25b	1.42593	52	65	C IV Mg II
P31a	1.02822	4.7	6.9	Mg II Fe II
P36a	1.96622	16	16	N V Si III
P36b	1.96688	23	24	Al II Si III
P42a	1.14819	6.2	8.6	Mg II Fe II
P44a	1.14351	10	14	Mg II Fe II
P70a	1.83710	41	43	Mg II Fe II
P147b	2.35187	6.0	5.3	C IV Si IV
P153b	2.51780	23	19	C IV Si IV
P155a	2.66316	59	48	C IV Si IV
P155a	2.94423	7.0	5.3	C IV Si IV
P155b	2.66216	23	19	C IV Si IV
P155b	2.94333	4.7	3.6	C IV Si IV

in sight lines separated by < 100 kpc, 5 from 22 sight lines (23%) at $100 - 200$ kpc, 6 coincidences in 103 systems (6%) at $200 - 600$ kpc, 2 in 107 (1.9%) at $0.6 - 1$ Mpc, and 2 in 264 (0.7%) at $1 - 2$ Mpc. We obtain these ratios by dividing the two histograms in Fig. 13. These ratios are very much lower limits since there are many cases in which we have limited or no ability to see systems in the partner QSO. High quality spectra with complete wavelength coverage would show many more systems include those with small W_{rest} values that would give much higher probabilities. We could obtain higher probabilities if we include the W_{pm} values in the calculation, but we have not done this.

7.3 Redshift-space distribution of AA coincidences

In Fig. 14 we see the 2D distribution of the absorber-absorber separations, in redshift space along the x -axis and in the plane of the sky along the y -axis. We place one of the two absorbers in each pairing at the origin. The y -axis is the impact parameter, and the x -axis is distance derived from Δz_{AA} assuming Hubble flow and ignoring peculiar velocities. Light rays travelling to us are horizontal lines going to the right. We show separately pairings that do not involve associated absorbers (including, but not limited to

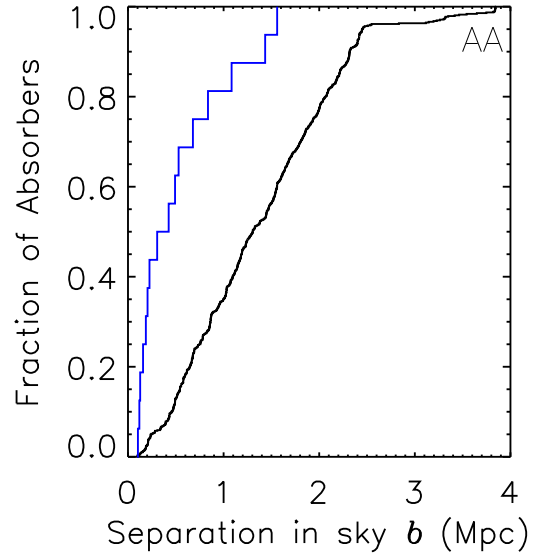


Figure 12. The cumulative distribution of the distances between lines of sight measured in the plane of the sky b proper Mpc. We show separately the separations between 15 of the AA coincidences (blue, stepped line) and the partner sight line, and the sample of 625 systems (black, smooth line) from which the AA sub-sample were drawn.

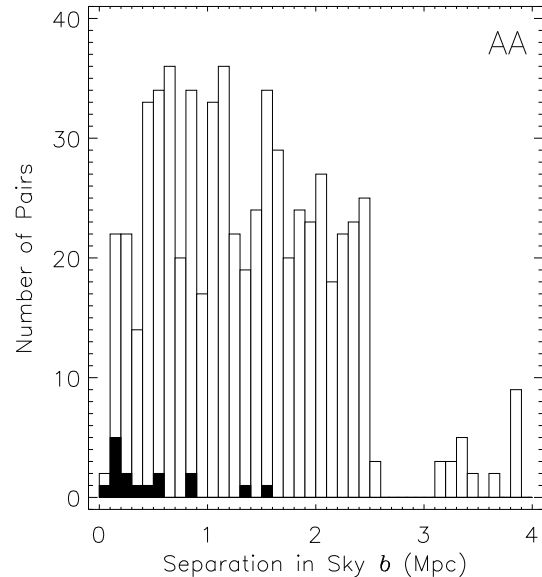


Figure 13. The distribution of distances between the 16 AA coincidences each with $\Delta z_{AA} < 0.005$ (solid) and the sample from which they were selected (clear). The horizontal axis is the impact parameter, the distance from each absorber to its partner QSO in the plane of the sky, b in proper Mpc. The clear histogram includes all absorption systems, including coincidences, but excluding all cases where $z_{\text{abs}} > 0.005 + z_{\text{em}}$ of partner QSO. For both histograms we have removed all absorption systems within 3000 km s^{-1} of the host QSO, and we count each coincident pair of systems as one system.

all the AA and AAV pairings that extend to approximately 5 Mpc) and those that do include one or two associated systems (including and not limited to all AAA coincidences). We have already seen projections of the absorber-absorber correlations into the two axes of this Figure. Fig. 7 showed the projection along the x -axis ignoring the sky separation, while Fig. 13 is the projection in the plane of the sky for coincidences with $\Delta z_{AA} < 0.005$, the AA coincidences.

We see the over-density of absorbers near the origin. We have already established the statistical reality of this excess, which seems to extend out to about 1 Mpc or perhaps ~ 2.5 Mpc. There are 23 absorbers within 2.5 Mpc (500 km s^{-1} at $z = 2$) of the origin, including all 16 AA coincidences that we list in Table 8. We see the background of absorbers separated by 5 – 20 Mpc that is approximately uniform in density, although sparsely sampled. The clumps of points far from the origin are accidental because they are nearly all from different QSO pairs. Clustering of two or more system pairings along the line of sight to a given QSO pair would appear as a horizontal grouping.

The distribution of absorbers around absorbers can be determined from their 3D spatial correlation function. If the absorbers arise in galaxies, then the correlation function for those galaxies, modified by peculiar velocities, our sampling function, and our measurement errors will describe the distribution in Fig. 14. The level of concentration of points near the origin of the plot then depends on the correlation length, the peculiar velocities and the measurement errors.

Errors in the measurement of absorption redshifts tend to smear the x -coordinates of the plotted points. Measurement errors of 23 km s^{-1} per absorption system will contribute a 1σ dispersion of only ~ 0.16 Mpc along the x direction, too small to have a major effect.

We see non-uniformity and asymmetry in the distribution of absorbers in the inner 2.5 Mpc. We choose 2.5 Mpc because we know from Fig. 1 that we have approximately constant number of sight lines as a function of separation in the sky out to 2.5 Mpc. In Fig. 13 we saw that the absorbers that we found also have an approximately uniform distribution in impact parameter out to 2.5 Mpc. This is because we deliberately observed all known close pairs of QSOs but only a fraction of those at larger separations. In this way we accidentally cancelled the increase with b^2 in the area of annuli on the sky of radius b . In the absence of clustering we expect the absorbers to be approximately uniformly distributed along the y -axis of Fig. 14. Fig. 15 is an enlargement of the inner 2.5 Mpc of Fig. 14.

We now comment on the distribution of the points. Although the excess of points near the origin is clearly real, the asymmetry in the distribution of this excess could be entirely accidental because the sample is small. Since we noticed the features *a posteriori* we decline to give any statistical assessment, and we leave the reader to decide if the evidence combined with the physical implications are sufficient to motivate further comment or investigation.

We see a relative lack of absorbers in the upper left at $x < 5$ Mpc and $y > 1.5$ Mpc. We have no explanation for this and expect that it is an accident. Within approximately 1 Mpc of the origin we see that the excess is mostly at angles below 45° from the x -axis. We do not have any explanation for such angles. However, we can instead think of the plot as showing a tendency of the clustering around an ab-

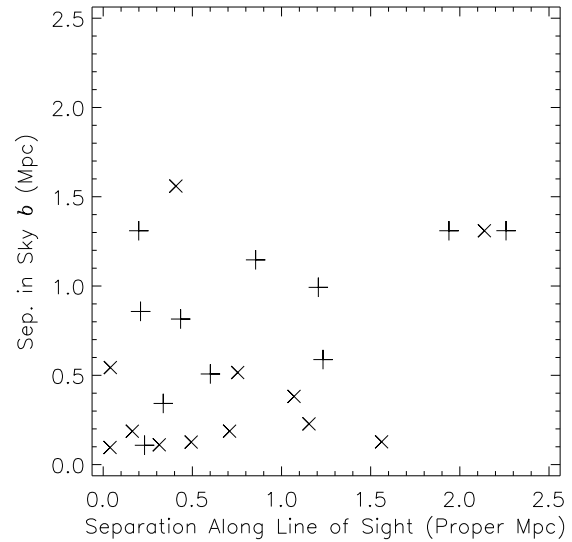


Figure 15. Enlargement of the inner 2.5 Mpc of Fig. 14.

sorber to be more widely distributed along the line of sight (x -axis) than in the plane of the sky (y -axis), and this has a well known explanation.

Crotts et al. (1997) found the same effect from a study of metal lines in HIRES spectra of the triplet of QSOs, P118abc. They found that the correlation between the lines of sight was much weaker than expected from the two-point correlation seen along many individual lines of sight. Crotts et al. (1997) proposed that the effect was caused by peculiar velocities that are large compared to the correlation length. The peculiar velocities make the line of sight correlation in velocity space appear to be more extended than it is in proper Mpc multiplied by the Hubble constant. This is the usual redshift-space distortion or anisotropy that makes the “fingers of God” in maps of galaxy position in redshift versus sky position. Clusters of galaxies are elongated in the redshift coordinate (Davis & Peebles 1983, Fig. 4) because of the large peculiar velocities. Peculiar velocities move points along the x -axis, decreasing the density near the y -axis. Peculiar velocities along the y -axis have no effect since they do not change redshifts or positions on the sky. For our absorbers the peculiar velocities could include random motions, rotations and winds flowing out from the absorbing galaxies. To account for the asymmetry we see in Fig. 15 we need velocities along the line of sight of $\sim 100 \text{ km s}^{-1}$. Adelberger et al. (2005) also claim to see this redshift distortion in their Fig. 12 that we will discuss below.

7.4 Qualitative assessment of the redshift-space distortion

In Fig. 16 we show the expected distribution of AA separations derived from the 3D 2-point correlation function of LBGs from Adelberger et al. (2005). Their correlation length measurements are larger but consistent with those from Cooke et al. (2006) who use redshifts for LBGs with similar redshifts and magnitudes, but with less sky coverage. We assume $\xi(r) = [(r + r_m)/r_0]^{-\gamma}$ with $\gamma = 1.6$ from

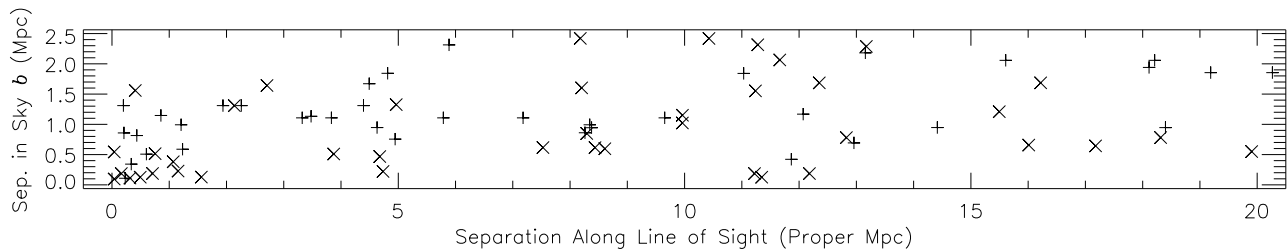


Figure 14. The separation in proper Mpc of two absorption systems, one in each of a pair of QSOs. We plot each pairing once, with one system at the origin and the other is marked by the \times , or a $+$ if either absorber is within 3000 km s^{-1} of its QSO. The x -axis is distance from one absorption system to that in the partner, obtained directly from the difference between the two absorption redshifts. This is the proper equivalent of the comoving π used in galaxy literature. The y -axis is the distance between the sight lines in the plane of the sky, at the redshift of the absorbers. This is the impact parameter b from Eqn. (1) and (2), and it is the proper equivalent of the r_p in galaxy literature. We limit the vertical axis to 2.5 Mpc because we saw in Fig. 13 that we have approximately constant number of sight lines per unit b out to this distance.

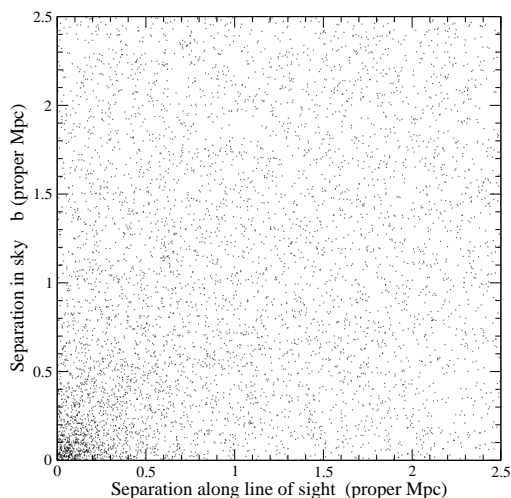


Figure 16. The expected distributions of absorbers about an absorber at the origin. We begin with a random distribution of points that sample the galaxy-galaxy two point correlation function. We ignore peculiar velocities but we add a Gaussian random deviate to the horizontal position of each point with $\sigma(v) = 23\sqrt{2} \text{ km s}^{-1}$ or $\sim 0.16 \text{ Mpc}$.

Adelberger et al. (2005). We set $r_m = 0.05$ proper Mpc to account for our difficulty in distinguishing multiple absorbers inside one halo. We convert the Adelberger et al. (2005) comoving correlation length measurements at $z = 1.69$ and 2.24 to proper Mpc and we linearly interpolate to $z = 2$, giving $r_0 = 2.06 \text{ Mpc}$ for our Hubble constant. We further reduce this by a factor of 0.6 to 1.24 Mpc at $z = 2$ to convert from the correlation length of their LBG galaxies to the correlation of all galaxies in the DEEP sample. We obtain the factor $0.6 = 3.2/5.4$ from the comparison at $z \sim 1$ given in Fig. 12 of Adelberger et al. (2005). To mimic our Fig. 14, we assume a constant number of sight lines per unit of impact parameter along the y -axis. Note that we have no paired QSOs separated by $y < 0.09 \text{ Mpc}$, and hence we can not see the full amplitude of the peak near the origin. By design the distribution is symmetric about the origin, and in this sense, and in the extent of the concentration about the origin it looks different from our data.

Table 10. Halo masses used for infall velocities in different models. We assume the probability of absorption in a halo of mass M is $\propto M^{-\beta}$. We list the percentage of halos of each mass listed on the top row in solar units.

Model	β	5.1×10^9	1.6×10^{11}	9.1×10^{11}
LowM	2	96.9	3	0.1
MidM	1	75	23	2
HiM	...	0.1	3	96.9

7.5 Adding gravitational infall

Adelberger (2005, Fig. 2) discusses the distortion produced by different types of peculiar velocity flows. Gravitational infall of one absorbing galaxy towards the other is a systematic effect that is correlated across the area of the plot. If the density field were spherically symmetric about the absorber at the origin we would expect radial towards the origin that moves most points closer to the y -axis. The amplitude of the infall will depend on the masses of the halos of the absorbers.

In Fig. 17 we show the effect of adding systematic infall velocities. We use infall velocities for halo masses given in Table 10 from the lower portion of Fig. 2 of Kim & Croft (2007). The halos give infall velocities of approximately 70 km s^{-1} out to 2.8 Mpc , declining to 20 km s^{-1} by 10 Mpc . We assume that the number of halos is distributed as M^{-2} (Vale & Ostriker 2004) and that the absorbing area of an halo scales with the halo mass. Chen et al. (2001) find that the area out to which C IV absorption is readily seen at low z scales with the galaxy luminosity, and we assume constant M/L . Hence we assume that the absorption we see samples a halo mass distribution $\propto M^{-1}$ that we call the MidM distribution in Table 10. We expect slightly larger infall velocities because we observe two galaxies that are absorbing, implying a local mass density above that around a typical galaxy that need not have an neighbour.

We add radial infall velocities directed towards the origin. These 3D velocities are a function of the radial distance (before we add simulated observational errors!) from the origin alone, with no random component. The component of the velocity along our line of sight decreases to zero as we rotate from the x -axis up to the y -axis, making a caustic like density peak, as shown in the upper right quadrant of Fig. 5

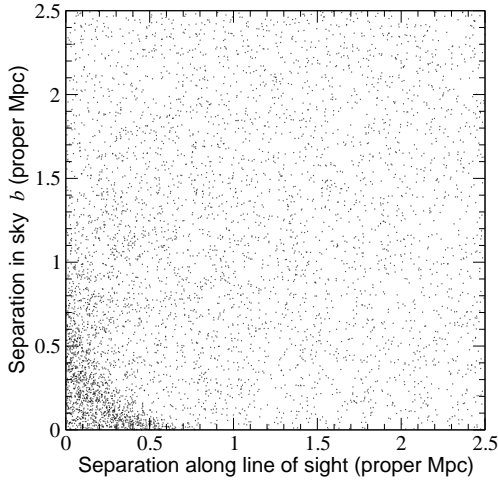


Figure 17. As Fig. 16 with observational errors and now including radial infall due to a moderate distribution of halo masses, MidM from Table 10.

of Kaiser (1987). Since we use more than one halo mass and we have smoothed in the x direction by adding random errors in the redshifts, the caustic is less distinct in Fig. 17. The infall increases the density of points along both the x and y axes. For $y < 0.1$ Mpc the infall moves points away from the origin and along the x axis, but we have almost no sight lines that sample these small y values. For other y values the infall moves points towards the y -axis, giving a lower density of points at $x > 0.4$ Mpc, $y < 0.5$ Mpc, and a higher density at $x < 0.2$, $0.2 < y < 0.5$ Mpc. This elongation of the density along the y -axis is the opposite of the asymmetry that we see in the absorber-absorber correlation.

7.6 Adding pair-wise random velocities

In Fig. 18 we add random velocities to represent the pair-wise velocity differences of galaxies. We select the velocities from the exponential distribution

$$f(v_{12}) = \frac{1}{\sqrt{2}\sigma_{12}} \exp\left(-\frac{\sqrt{2}}{\sigma_{12}}|v_{12} - \bar{v}_{12}|\right) \quad (10)$$

from Coil et al. (2007, Eqn 17), where \bar{v}_{12} is the mean infall velocity. Since we apply these random velocities to the undisturbed x, y coordinates, before we apply the infall velocities or simulated measurement errors, we set the term $\bar{v}_{12} = 0$. This term is used if we fit the function to data comprising velocities that will necessarily include infall. We choose the dispersion $\sigma_{12} = 240 \text{ km s}^{-1}$ to represent the random pair-wise velocity differences. The points are smeared along the x -axis giving the usual redshift-distortion that makes the “finger of God” effect that is most readily seen in dense groups and clusters where the peculiar velocities are large. Now we see a tendency of the points to be more extended along the x -axis, but it is unclear if this provides a better match to our data.

7.7 Estimation of the pair-wise velocity dispersion

Is the distribution of absorber-absorber separation in Fig.15 consistent with absorption arising in ordinary galaxies with

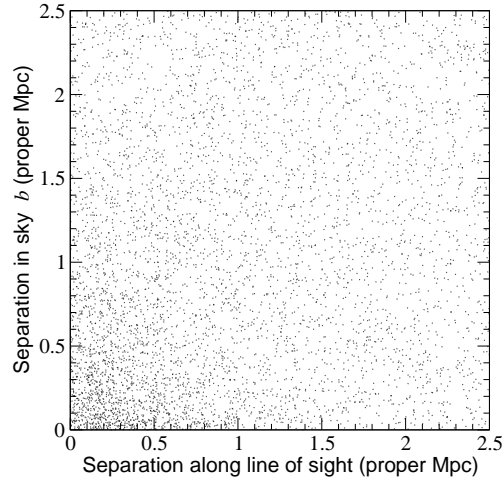


Figure 18. As Fig. 16 including observational errors and radial infall (for the MidM halo mass distribution) but now adding random pair-wise velocities from the exponential distribution with a $\sigma_{12} = 240 \text{ km s}^{-1}$ applied to the absorber that is not at the origin.

the expected galaxy-galaxy autocorrelation, infall and the pair-wise peculiar velocity distributions? Given the small size of our sample, we can only detect the absorber-absorber correlation on very small scales where the peculiar velocities are larger or comparable to the Hubble flow. Let us then assume that we know the absorber-absorber correlation length, the infall velocities and the measurement errors, and ask what value for the pair-wise dispersion of the velocities is most consistent with the data. We understand that the pair-wise velocity distribution, the infall and the correlation length are all related to each other and to the history of the density distribution (Scoccimarro 2004; Slosar et al. 2006).

We calculate the likelihood of our absorber-absorber distribution, as a function of the dispersion of the pair-wise velocities σ_{12} . We estimate the probability of each coincidence shown on Fig. 15 from the density of points on a version of Fig. 18 with many more points and various values for σ_{12} . For each absorber in Table 5 we calculate the probability P_s of absorption at x, y in the spectrum of the partner QSO.

The probability of one absorber at position x_i in an interval $0 < x < x_{max}$ of one line of sight is the product of three probabilities, $P_s = p_l p_i p_r$ where p_l is the probability of finding no absorbers in $0 < x < x_l$, p_i is the probability of finding an absorber at x_i and p_r is the probability of finding no absorbers at $x_r < x < x_{max}$. We have no information on possible extra absorbers in the interval $x_l < x_i < x_r \sim 0.85$ Mpc, because we can see a maximum of one absorber per FWHM of the spectra. From the Poisson distribution, the probability of no absorbers is $p = e^{-\mu}$ where μ is the expected number of absorbers. We have

$$\mu_l = w_i \int_0^{x_l} p(x, y) dx \quad \text{and} \quad \mu_r = w_i \int_{x_r}^{x_{max}} p(x, y) dx \quad (11)$$

where $p(x, y)$ is probability of an absorber at (x, y) given by the density of points and w_i is a weighting factor that accounts for the sensitivity of the spectrum to an absorption system. Similarly the probability of the absorber at x_i is $p_i = w_i p(x_i, y)$, and hence the probability for sight line s is

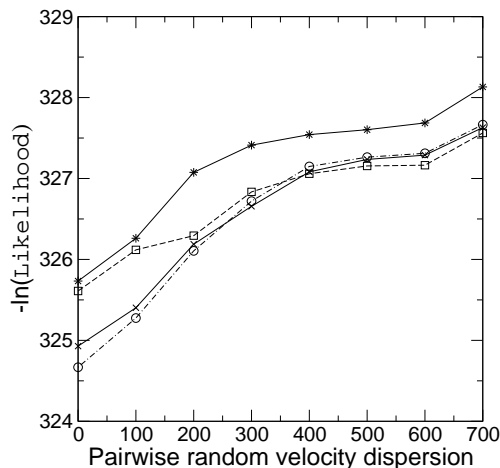


Figure 19. The maximum likelihood estimate of the pair-wise random velocity dispersion. The vertical axis shows the negative of the natural likelihood of the absorber-absorber data, both coincidences and lack of coincidences. The horizontal axis shows the of the random pair-wise velocities dispersion σ_{12} for the exponential distribution in Eqn. 10. Reading down from the top at $\sigma_{12} < 200 \text{ km s}^{-1}$, the stars show a model with no infall, the boxes high mass halos (HiM), the crosses medium masses (MidM) and the circles low mass halos (LowM).

$$P_s = e^{-\mu_l} w_i p(x_i, y) e^{-\mu_r}. \quad (12)$$

The weighting w_i is the fraction of all W_{rest} values that are larger than the W_{pm} value in Table 5. If we do not list a value for either W_{rest} or W_{pm} we assume $w = 0.2$ corresponding to $W_{pm} = 1.5 \text{ \AA}$ in Fig. 10. If $W_{pm} = -1$, meaning that the main line could not be seen in the partner spectrum, we use $w = 0.1$.

The likelihood \mathcal{L} of the data set for a given model is the product of the probabilities for each sight line. We count each coincidence twice since the W_{pm} values for the two sight lines differ. We ignore absorbers with $z_{abs} > \Delta z_m + z_{em}$ of the partner QSO, where $\Delta z_m = (1+z)H(z)x_{max}/c$ is the redshift equivalent of the distance x_{max} .

In Fig. 19 we see that the likelihood of the data is maximum when the $\sigma_{12} = 0$ with a 1σ upper limit of 100 km s^{-1} and a 2σ limit of 300 km s^{-1} . The likelihood is insensitive to larger pair-wise velocity dispersions because the density of points is then nearly uniform in space. These pair-wise velocity dispersion values are very much at the lower end of the values reported for galaxies. The absorber-absorber correlation is more concentrated near the origin that we expect except for a very “cold” population, with low velocities relative to their neighbours.

In Fig. 19 we also show the likelihood of the three other models. We show a model with no infall velocities, a model where the probability of absorption in a halo is proportional to M^{-2} favouring very low mass halos and a model favouring high mass halos (see Table 10). To first order the models give similar infall velocities and all are compatible with the data. In detail the data are most likely in models with low to medium halo masses, and less likely by more than 1σ in models using high mass halos or no infall. The trends follow because the low and medium mass halo models both give high density in the caustic region where we have 4 data points. The high mass halos have excessive velocities giving

a slightly lower density near the origin, while the no-infall model has the highest density at the origin but a lower density in the caustic region.

Davis & Peebles (1983) estimated line of sight random velocity differences locally could be represented as

$$\sigma_{12}(b) = 340 \pm 40(b/1.4 \text{ Mpc})^{0.13 \pm 0.04} \text{ (km s}^{-1}\text{)}, \quad (13)$$

for projected separations $14 \text{ kpc} < b < 1.4 \text{ Mpc}$. Like most authors we will assume that σ_{12} values apply with no b dependence over a few Mpc. At redshifts $z \sim 0.1$ Zehavi & et al. (2002) find SDSS blue galaxies give $\sigma_{12} \sim 300 - 450 \text{ km s}^{-1}$ while red galaxies give $\sigma_{12} \sim 650 - 750 \text{ km s}^{-1}$. Li et al. (2006) find $200 - 400 \text{ km s}^{-1}$ for blue and $600 - 800 \text{ km s}^{-1}$ for red SDSS galaxies. For the 2dF Redshift survey Madgwick et al. (2003) find $\sigma_{12} = 416 \pm 76 \text{ km s}^{-1}$ for active star forming galaxies and $612 \pm 92 \text{ km s}^{-1}$ for passive galaxies. We expect lower velocities at higher redshift but measured values are only slightly lower. At $z \sim 1$ Coil et al. (2007) estimate $\sigma_{12} = 240 \pm 20 \text{ km s}^{-1}$ for blue galaxies and $530 \pm 50 \text{ km s}^{-1}$ for red galaxies.

The low pair-wise velocities for the absorbers are marginally compatible with absorption in some samples of blue galaxies, and incompatible with red galaxies. This implies that the absorbers tend to avoid the rare high density regions such as clusters of galaxies where the red galaxies gain much of their larger pair-wise velocities. We also believe that our sample is much too small to give a fair sample of all absorbers and hence we might anticipate a larger velocity dispersion in a larger sample, as is seen with galaxies.

7.8 Limits on Wind Outflows

We can use our upper limit on the random velocities to put a limit on wind outflow velocities. Adelberger et al. (2005) recommended this test as one of the best ways to try to determine how far winds extend from the centres of galaxies. Our sample is well suited to this examination because our redshift errors of 23 km s^{-1} are small compared to the wind velocities of hundreds of km s^{-1} , and much smaller than the errors obtained for galaxies at $z = 2$ from their optical and UV lines.

Consider absorption in gas flowing radially out from galaxies. We assume this gas is transparent so we see either absorption with a velocity component towards us, or away from us. The result is that the redshifts of the absorbers are changed by an amount given by the wind velocities. Assume pure radial outflow at velocity v_w confined to a thin spherical shell, and assume that absorption occurs on either the front or the back of the shell, but not on both sides. The mean component of the wind velocity along the line of sight is then $0.5v_w$. If instead we see the same absorption from both sides then the mean velocity is zero by symmetry. The mean velocity will be less than $v_w/2$ depending on the frequency of two-sided absorption. Since we attempt to measure z_{abs} values for the velocity component with the highest optical depth, we will tend to set the z_{abs} value to one of the other side rather than the mean of both, except when they give similar or blended lines.

We will model the component of the wind velocity in the line of sight as a Gaussian random deviate. We expect that a Gaussian is a more realistic distribution than that from a pure radial outflow with a constant velocity for all

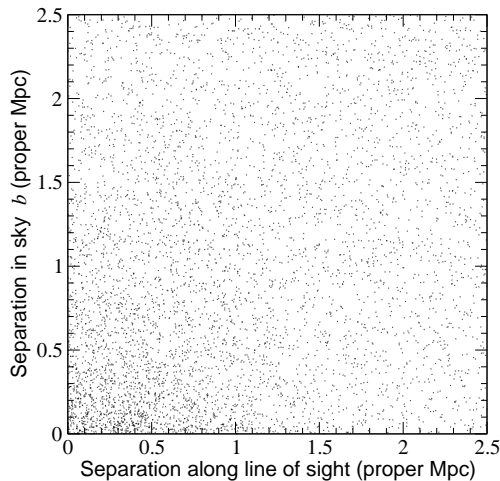


Figure 20. As Fig. 16 with observational errors, radial infall and random pair-wise velocities from the exponential distribution with $\sigma_{12} = 100 \text{ km s}^{-1}$, and now adding random peculiar velocities from a Gaussian with a $\sigma_w = 88 \text{ km s}^{-1}$ applied to the absorber that is not at the origin. This represents radial winds of $v_w = 125 \text{ km s}^{-1}$ from each galaxy, including that at the origin.

galaxies. We set the standard deviation of the Gaussian to $\sigma_w = 0.5v_w\sqrt{2}/\sqrt{2/\pi}$. The last term is the expected absolute value of a random Gaussian deviate, $\sqrt{2/\pi} = 0.7979$. The first $\sqrt{2}$ term accounts for the wind from the galaxy that makes the absorber that we place at the origin of the plot, so we do not need to also add a deviate to the origin. We choose the absorber that we place at the origin of the plot at random from each pairing, and we assume equal and uncorrelated winds for both absorbers. We then add these Gaussian deviates to each absorber on the plot, and not to the origin.

In Fig. 20 we add random velocities from a Gaussian pdf with a dispersion of $\sigma_w = 222 \text{ km s}^{-1}$ to model a wind with $v_w = 250 \text{ km s}^{-1}$. Since the pair-wise random velocities can hardly be zero, we use a models with $\sigma_{12} = 100 \text{ km s}^{-1}$. This model has much more dispersion than our data.

Adelberger et al. (2005, Fig. 1) have estimated the redshifts of LBGs at $2 < z < 3.5$ from three different spectral features, the Ly α emission line, the ISM UV absorption lines and nebulae emission lines such as [OII], H α , H β and [OIII]. The nebulae lines are believed to be close to the systemic velocities and give errors of 60 km s^{-1} for 90 galaxies. The Ly α lines and UV lines were seen in spectra with about 10 \AA (600 km s^{-1}) resolution and have much larger errors of approximately $200 - 275 \text{ km s}^{-1}$ (from the σ_z values below Eqn. 3 in Adelberger et al. (2005) for $z = 2.6$) The Ly α lines give redshifts that are systematically larger by up to 1000 km s^{-1} and typically 450 km s^{-1} . The UV absorption lines give redshifts systematically smaller than the nebular lines by about 250 km s^{-1} with wide range from 800 km s^{-1} smaller to 200 km s^{-1} larger. The UV absorption lines are direct evidence for outflowing winds. Separately, Adelberger et al. (2005) see strong C IV lines in background objects 40 kpc from LBGs and weak lines extending much farther, but they do not know if this is wind material, and they do not know if the winds escape from the LBGs. They notice that the mean absorption within 40 kpc of foreground galax-

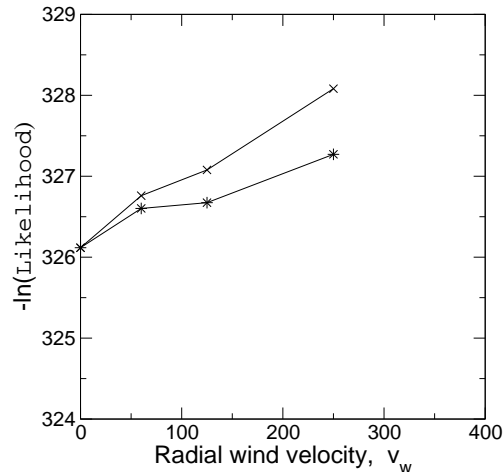


Figure 21. The negative of the natural likelihood of the absorber-absorber data, both coincidences and lack of coincidences, as a function of the wind velocity v_w (km s^{-1}), shown by the upper line marked with crosses. We also show (lower line with stars) a case where the wind velocities are restricted to 1/3 of the galaxies.

ies is large $W_{rest} \ 2.7 \text{ \AA}$ and implies significant absorption over at least a 260 km s^{-1} velocity range.

Adelberger et al. (2005, Fig. 12) shows the positions of C IV absorbers (about 17 systems with 68 components) that they observed with < 0.4 proper Mpc separation and $< \pm 4$ Mpc redshift difference from LBGs. For each impact parameter they calculated the redshift difference out to which the 3D correlation function would place 50% of absorbers if there were no peculiar velocities. They see that most absorption components have larger velocity differences from their QSOs, implying several hundred km s^{-1} peculiar velocities. They suggest that these peculiar velocities may be winds, but they do not discuss normal pair-wise random peculiar velocities that can be comparable in size.

We do not see such large peculiar velocities. In Fig. 21 we see the likelihood of the absorber-absorber correlation data declines significantly with increasing v_w that we use to represent the random wind velocity. The data prefer zero wind velocity with a 1σ limit of $v_w < 45 \text{ km s}^{-1}$ and a 2σ limit of 250 km s^{-1} .

The Adelberger et al. (2005) sample differs from our in two obvious ways. We measure distances between pairs of absorbers while they measure distances from LBGs to absorbers. We take absorber redshifts from the main component visible in moderate resolution spectra while they consider all the components visible in higher resolution spectra. Hence they are exploring the low column density gas around LBGs while we are more sensitive to higher column density gas that is likely near to typical absorbing galaxies that may not be LBGs.

Absorption in gas flowing out from galaxies at a mean velocity of $v_w = 250 \text{ km s}^{-1}$ would produce much more elongation along the line of sight than we see. We conclude that the absorbing gas is not in fast winds. The winds seen by Adelberger et al. (2005) in LBG spectra are not representative of absorption systems that we see. Either the winds are confined to LBGs, or they do not extend to $> 40 \text{ kpc}$ with large velocities, or they do not produce absorption we can detect. Here 40 kpc is the distance from LBGs at which

Adelberger et al. (2005) see strong C IV absorption (not necessarily from winds). Typical absorption systems are too common to be confined to smaller distances from galaxies.

Adelberger et al. (2005, §3.1) further deduce that the LBGs in their sample can account for roughly one-third of C IV 1548 lines with $W_{rest} > 0.4 \text{ \AA}$ that is the typical W_{rest} for our AA absorbers. We model this assuming that their LBGs account for 1/3 of all z_{abs} that we can detect. For 1/9 of the points, where both absorbers arise in fast winds, we set $\sigma_w = 0.5v_w\sqrt{2}/\sqrt{2/\pi}$ as usual. For 4/9 of points where only one of the two absorbers arises in a wind we set $\sigma_w = 0.5v_w/\sqrt{2/\pi}$, and for the remaining 4/9, $\sigma_w = 0$. The lower curves in Fig. 21 show that the likelihood is still lower for higher wind velocities, with a 1σ limit of $< 95 \text{ km s}^{-1}$ but now 250 km s^{-1} is allowed at the 2σ level.

Hence our small sample of absorber-absorber coincidences could arise in fast winds from LBGs alone extending to 40 kpc and making 1/3rd of strong C IV or Mg II lines that we could detect. However the data prefer absorption in a cold population, with no extra velocity dispersion from winds, or otherwise. We are not consistent with most C IV or Mg II coming from such high velocity winds. If most galaxies have high velocity absorbing winds, these winds must be confined to $\ll 40 \text{ kpc}$, the typical radius around a galaxy at which strong metal lines are seen. If all galaxies have winds that travel out $> 40 \text{ kpc}$ then the wind material must have low velocities where we see absorption, or not have the density, metal abundance, ionization and velocity structure necessary to make metal lines that we can see.

8 SPATIAL DISTRIBUTION OF ABSORBERS AROUND QSOS

We now leave the absorber-absorber coincidences and turn to the QSO-absorber coincidences. The EA pairings share some features with the AA pairings (3D correlation, infall velocities, pair-wise random velocities) but they differ in other ways, especially the much larger errors on the z_{em} values and the possibility of larger halo masses for the QSOs.

We will look to see if there are any signs of an asymmetric distribution of absorbers around the QSOs. If the UV radiation from QSOs can change or destroy absorbers, then we will see an asymmetric distribution of absorbers around QSOs if the QSO UV is confined to a narrow beam, or alternatively if QSOs emit isotropically but for only 0.3 – 10 Myr. We will not use the absorber-QSO correlation to look for signs of winds from galaxies, because the errors on the z_{em} values are too large.

In Fig. 22 we show the cumulative distribution of separations of the sight lines from the foreground QSOs in each pairing. We show the 18 EA coincidences and separately the sample from which they were selected, which includes the associated absorbers. We see that the EA coincidences are preferentially seen at impact parameters $b < 1.2 \text{ Mpc}$. There is a 2% chance of seeing a larger difference between the two cumulative distributions in a random sample of 18 pairs. Preference for small separations is not as strong as for the AA coincidences seen in Fig. 12.

In Fig. 23 we show the distribution of the separations of the EA systems compared to all QSO separations, now as a histogram. As for the AA coincidences in Fig. 13, we

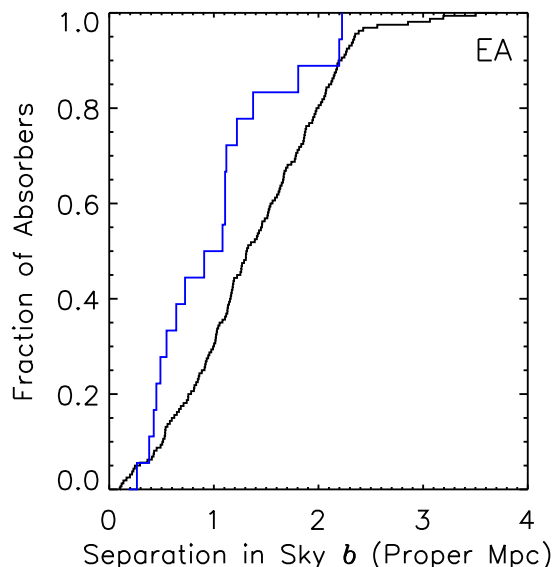


Figure 22. The cumulative distribution of the separations in the sky of the QSO pairs. The smooth black line shows the distances from all foreground QSOs to the partner lines of sight, plus the distances for the background to the foreground QSOs when the z_{em} difference is < 0.005 . The 18 EA coincidences are the sub-set shown by the fainter blue stepped line.

divide the histograms to estimate the probability of seeing absorption as a function of impact parameter. The probability of seeing an EA coincident absorption when a sight line passes a QSO is 1/6 (17%) at impact parameters of $b = 100 - 200 \text{ kpc}$, 4/16 (25%) at $200 - 500 \text{ kpc}$, 4/40 (10%) at $0.5 - 1 \text{ Mpc}$, 7/43 (21%) at $1 - 1.5 \text{ Mpc}$ and 2/62 (3%) at $1.5 - 2.5 \text{ Mpc}$. As for the AA coincidences, these ratios are very much lower limits because we do not detect most weak metal lines. For example, if we add the EAV coincidences that extend out to $v_{EA} \pm 1000 \text{ km s}^{-1}$ we are less likely to miss a coincidence that has a large z_{em} error, and the probabilities rise by about 30/18. On scales below 100 kpc where we have no sight lines, Bowen et al. (2006) found Mg II in 4/4 sight lines at impact parameters of 26 – 97 kpc, while Hennawi et al. (2006, Fig. 1) see LLS in 3/3 cases at $< 100 \text{ kpc}$. At 100 – 200 kpc our probability of 1/6 for EA coincidences is not much lower than the 3/8 from Hennawi et al. (2006, Fig. 1), for their LLS absorbers.

We are surprised that the probability of detecting an EA or EAV coincidence is approximately constant from about 0.1 out to 1.5 Mpc. We expect the probability to rise rapidly as the b -value decreases, especially at 100 – 300 kpc, because of galaxy clustering, as we saw for the AA coincidences. The distribution of absorbers around QSOs (Fig. 23) is less centrally concentrated than the distribution of absorbers around absorbers (Fig. 13).

Why are absorbers be more concentrated around absorbers than around QSOs? If anything we might expect more concentration around the QSO host galaxies than around random galaxies. The difference is not caused the the z_{em} errors because we are discussing a distribution in the plane of the sky, not in redshift. For the absorber-QSO

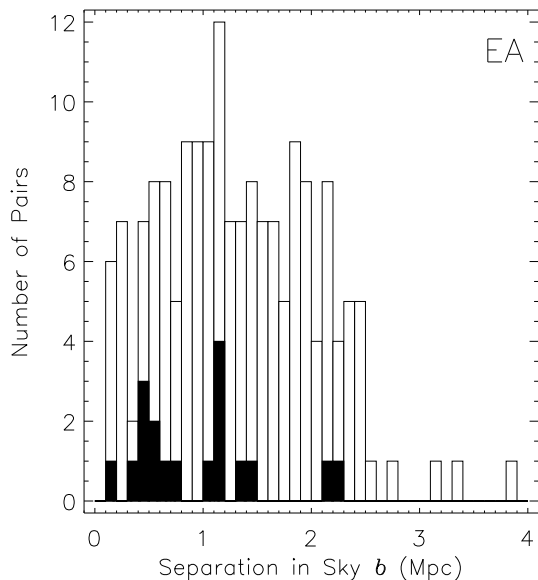


Figure 23. The distribution of impact parameters between the 18 EA coincidences (black) and the sample from which they are drawn (clear). We show the distances between the sight lines measured in the plane of the sky. The clear histogram shows the distances from all foreground QSOs to the partner lines of sight, plus the distances from the background to the foreground QSOs when the z_{em} difference is < 0.005 and including all EA pairings.

correlation the z_{em} errors can cause systems to have a larger Δz_{EA} or v_{EA} than we consider for an EA or EAV coincidence, but this will not be a function of the impact parameter. Fig. 23 looks similar when drawn for both the EA + EAV coincidences that extend out to 1000 km s^{-1} , but with a bit less concentration around the QSO, presumably because we pick up more associated absorbers that are not strongly influenced by clustering.

We propose that the probability of seeing an EA or EAV coincidence does not rise rapidly at low impact parameters because the absorbers nearest to the QSOs are often destroyed by the UV from the QSOs, perhaps by photoevaporation (Hennawi & Prochaska 2007).

8.1 Redshift-space distribution of absorbers around QSOs

In Fig. 24 we show how the absorption systems are distributed around the QSOs in two dimensions. This Fig. is like Fig. 14 but we now place the QSOs at the origin of the plot. The x -axis is distance from the QSO to the absorber along the line-of-sight. We obtain this from $z_{\text{em}} - z_{\text{abs}}$, giving positive values when $z_{\text{abs}} < z_{\text{em}}$. If there were no redshift errors or peculiar velocities, the right hand of the plot would contain space nearer to us than the QSOs. The y -axis is the impact parameter in the plane of the sky. As we discussed for the EA values in §5.4 we include both foreground and background QSOs since many pairs have similar z_{em} values and z_{em} errors can be large. We show an 8 Mpc range for the x -axis because the UV from the QSOs is expected to a

factor of a few larger than the UVB out to about 4 Mpc for this sample of QSOs (Kirkman et al. 2007).

We include on the plot the absorption systems from Table 1 of Hennawi et al. (2006). The systems are Ly α limits and damped Ly α lines within 1500 km s^{-1} of the z_{em} values of 149 foreground QSOs at projected separations of $0.031 - 2.4 \text{ Mpc}$. We are interested in the distribution of the absorbers in velocity, and not in the absolute rate of detection, and hence we are not concerned that some of their systems might not have high H I column densities.

Errors in the z_{em} values will often be several hundred km s^{-1} and hence the x -axis location of many points will have large random errors. As we discussed in §5.4 the narrow width of v_{EA} values for the coincident EA systems suggests that some QSOs have z_{em} errors of $< 525 \text{ km s}^{-1}$. However, we also expect larger errors for many QSOs. Hennawi et al. (2006) list errors of 300, 500, 1000 and 1500 km s^{-1} , depending on the emission lines seen, for the z_{em} values that they provide and we use.

The interpretation of Fig. 24 is complicated by the presence of background QSOs on the left hand side of the plot. The spectra of these QSOs sample only part of the line-of-sight past the foreground QSO, the part to the right of the QSOs position. We have 5 QSOs near zero, 3 at -0.5 to -4 Mpc and 8 at -4 to -8 Mpc . These QSOs are all from our sample, since we allow EA systems to come from QSOs with similar or identical z_{em} values. Hennawi et al. (2006) did not consider QSOs within 8 Mpc of their foreground QSOs. There few QSOs have a small effect on the total sample of 313 QSOs.

We discussed in §7.5 the effects of systematic infall velocities for the absorber-absorber correlation. That discussion also applies to absorbers around QSOs, with the difference that the infall velocities may be different, though not necessarily higher (Slosar et al. 2006), if the QSOs reside in more massive halos than typical galaxies. Croom et al. (2005) estimated QSO halo masses of $4.2 \pm 2.3 \times 10^{12}$ solar masses in the 2QZ sample at all redshifts. Less directly, Kim & Croft (2007) use the distribution of H I absorption seen in background QSOs to estimate the masses of nearby foreground QSO halos. They find a mean mass of $\log M = 12.48^{+0.53}_{-0.89}$ in solar units for QSOs at $z = 3$ with absolute G-band magnitude -27.5 , a factor of 20 above the mass of LBGs.

Adelberger (2004, Fig. 16) shows corrections for systematic infall towards QSOs plus random peculiar velocities. These corrections are typically $0.2 - 0.4 \text{ Mpc}$ at $z = 3$ for the distances out to 4 Mpc, implying (Hubble flow) velocities of $40 - 80 \text{ km s}^{-1}$. Systematic corrections of this size have little effect on our plots. As we mentioned in §7.5 Kim & Croft (2007, Fig. 2) use simulations to estimate how the mean radial infall velocities increase with the mass of the halo. These infall velocities are also modest, except for their most massive halo with 5.1×10^{12} solar masses that gave peak infall velocities of 270 km s^{-1} at 1.2 Mpc .

8.2 Is the UV emission from QSOs is beamed?

The first popular explanation for why we see few transverse absorbers along the los to individual QSOs is that the UV from QSOs illuminates the los but not the transverse directions. Absorbers in the UV beam and near to the QSO are

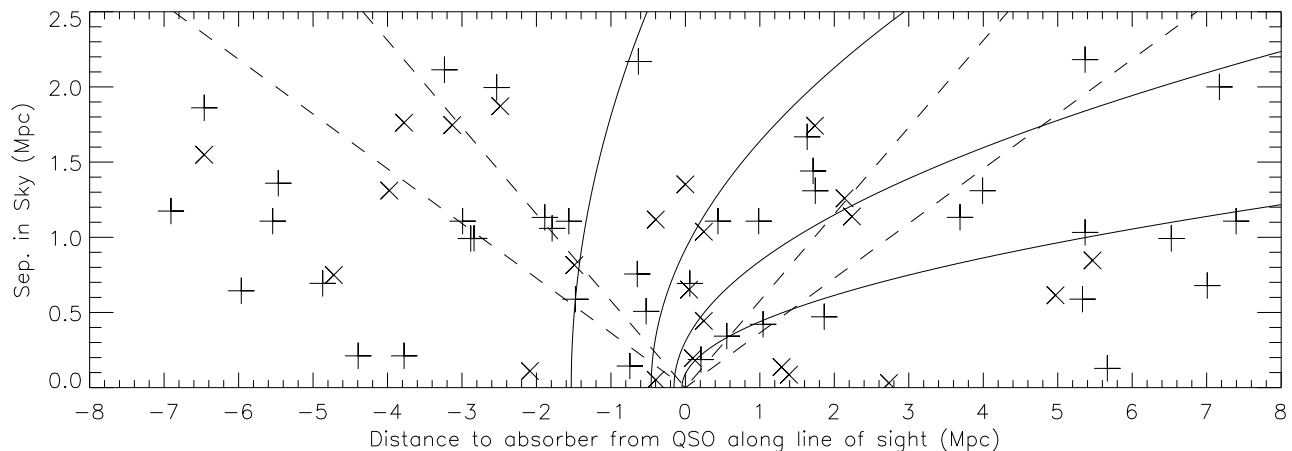


Figure 24. The distribution of absorbers near to QSOs that we place at the origin of the plot. Rays from the QSOs travelling towards us are horizontal lines extending to the right. The horizontal axis is derived from the velocity difference $v_{EA} \sim c(z_{em} - z_{abs})/(1+z)$ which is positive for absorbers that have a smaller redshift than the emission redshift of the partner QSO. We have converted the v_{EA} values into proper Mpc using the Hubble flow alone, ignoring peculiar velocities. The vertical axis shows the proper distance between the two QSOs in the plane of the sky, coming from their angular separation. We truncate the plot at $b = 2.5$ Mpc because Fig. 23 shows that the density of impact parameters for possible EA coincidences is nearly constant up to this value, but then declines by a factor of several. We show the 41 absorbers (+ symbols) that we saw around 167 QSOs (the sum of the open histograms at $b < 2.5$ Mpc on Fig. 23), and 23 absorbers (x) towards 146 QSOs from Hennawi et al. (2006). We use our z_{abs} for 3 cases where we report the same absorber in the same QSO, and 2 additional z_{abs} from their Table 1 are outside the area of this plot. The dashed lines show angles of 20 and 40 degrees from the horizontal axis, while the parabolas show the maximum distance the light travels from a QSO if that QSO switched on 0.3, 1, 3 or 10 Myr ago. Points below the dashed lines and to the right of the parabolas are more likely to be illuminated by the UV flux that we see from each QSO. Errors in the z_{em} values move points horizontally 2 - 4 or more Mpc.

destroyed or photo-evaporated (Hennawi & Prochaska 2007) so they no longer make absorption lines that we can see.

Let us put aside the z_{em} errors, peculiar velocities, and complications of QSOs near to QSOs and look for evidence that the QSO UV is beamed. Let us assume that the UV luminosities of the QSOs have not changed for > 17 Myr so they can illuminate all of Fig. 24. Assume that the UV from all QSOs is emitted only inside a pair of coaxial cones, one opening towards the Earth and the other away, and with their vertices at the QSO. If the QSO UV destroys the transverse absorbers that we do not see in the los, then we expect absorbers will be less common inside the cones of UV radiation.

We show on Fig. 24 dashed lines for cone apex half-angles of $\theta = 20$ and 30 degrees measured up from the horizontal axis, the line-of-sight to the Earth. We see numerous absorbers between the horizontal axis and the dashed lines, and to first order the distribution of absorbers around the QSOs looks isotropic.

However, three issues persuade us that the plot is compatible with radiation confined to cones where there is a lower density of absorbers. First, the UV may destroy absorbers out to at most 4 Mpc from the QSO at the origin. The precise distance will depend on the absorber density and structure, the ions we see, the sensitivity of the spectrum, and the QSO luminosity. The density of points is lower inside the 20 degree cone out to about 4 Mpc. Second, z_{em} errors will more often move points into the cone than outside it when the impact parameter is small. This can account for the absorbers near the x -axis. Third, line-of-sight to the Earth can be anywhere in the UV illuminated cone, includ-

ing at the edge of the cone. The probability of looking into a cone at a some angle to the cone axis is proportional to that angle. If a line-of-sight is along one edge of the cone, then we expect absorbers below the dashed line down to the horizontal axis, on both sides of the origin, because the figure ignores the position angle on the sky from the QSO at the origin to the absorber.

8.3 QSO lifetimes

The second popular explanation for why we see no transverse absorbers along the los to individual QSOs is that the QSOs have a short life time of ~ 1 Myr. By life time we mean how long has a QSO had a UV luminosity similar to that seen today.

If the QSOs emit isotropically but were less luminous in the past, then we expect a lack of absorbers confined to regions illuminated while the QSOs are luminous. These regions are bounded by parabolic surfaces with the QSO at the focus and the apex of the parabola farther away from us by half the distance that light can travel in the QSO life. All rays leaving a QSO at a given time and reflecting on this parabola reach us at the same time. Adelberger (2004, Fig. 3) and Visbal & Croft (2007, Fig. 1) show these parabolic surfaces that have the equation

$$y = \sqrt{2d(x + d/2)}, \quad (14)$$

where x is the horizontal axis of our plots, along the line-of-sight to Earth and y is the impact parameter in the plane of the sky. With x and y in proper Mpc, the d in the equation is the delay measured in Mpc which corresponds

to a time delay t in Myr of $t(\text{Myr}) = 3.2617d(\text{Mpc})$. We show delays of $t = 0.3, 1, 3$ and 10 Myr, corresponding to $d = 0.09198, 0.3066, 0.9198$ and 3.066 Mpc. All points in space that are to the right of the parabola for a given life time will have been exposed to the QSO flux.

A key point is that these parabolas are strongly asymmetric about the QSO while the bi-cone beaming hypothesis gives a symmetric pattern. We should then be able to distinguish beaming from QSO life time by examining the distribution of absorbers about the QSOs. We again assume that the QSOs UV is only able to destroy absorbers out to some distance, and we ignore the infall velocities that are probably much smaller than the errors on the z_{em} values.

There are many points to the right of the parabolas where we would expect none if the QSOs have short lives, and their UV destroys all nearby absorbers. We expect some absorbers inside the parabolas for two of the three reasons already mentioned for the beamed bi-cone model. The QSO UV will only destroy absorbers out to at most 4 Mpc, depending on the QSO and absorber, and the z_{em} errors will move many points horizontally. Hence the plot could be compatible with life times of about 0.3 Myr, leading to the low density of points to the right of the smallest parabola and extending out to 5 Mpc. We do not advocate this explanation because a lifetime of 0.3 Myr is at the lower limit of other estimates. Croom et al. (2005) estimate QSO active life times of $4 \times 10^6 - 6 \times 10^8$ yr at $z \sim 2$. Adelberger & Steidel (2005) argue that the lack of dependence of the QSO-galaxy correlation length on QSO luminosity implies that lower luminosity AGN live longer.

9 BAL SYSTEMS

So far we have ignored the BAL systems. We now present two figures that explore potential coincidences in BAL systems between the paired lines-of-sight. We do not expect to see any statistically significant excess coincidences over the random distributions, because the BAL winds are believed to extend much less than a Mpc from the QSOs.

In Fig. 25 we show the distribution of BAL system redshifts relative to the redshifts of the partner QSO. We see that about 50% of the differences are confined to $0.1 < \Delta z_{EA} < 0.1$. In comparison 6 showed that the non-BAL absorbers show an excess that is more confined around $\Delta z_{EA} = 0$. The Δz_{EA} values for the BAL systems may have a wider dispersion in part from the difficulty in selecting a single z_{abs} for a BAL system that shows many components spread over a large velocity range. In addition the BAL systems might ignore the partner QSO and the excess at $0.1 < \Delta z_{EA} < 0.1$ may come from the similarity of the two z_{em} values combined with the tendency of BAL systems to arise at $v_{\text{abs}} \sim 0$. To make progress we would prefer a sample in which the background QSO z_{em} was much larger than the foreground value.

In the lower panel of Fig. 25 we look for coincidences between BAL systems in one sight line with BAL systems in the other sight line. There is no excess near to $\Delta z_{AA} \sim 0$, except to the occurrence of 4 pairings at $\Delta z_{AA} \sim 0.03$.

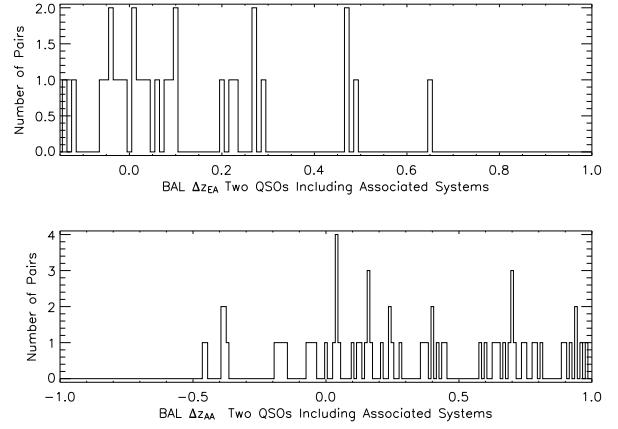


Figure 25. The Δz_{AA} and Δz_{EA} distributions for the 34 BAL systems, with Δz bins of 0.01.

10 DISCUSSION

In this paper we report the first sample of absorption systems showing metal lines in a large sample of pairs of QSOs that are close in the sky. The QSO pairs are separated by $0.1 - 2.5$ Mpc at $0.2 < z < 4$ and typically 1 Mpc at $z = 2$. We found 691 absorption systems in the spectra of 310 QSOs in 170 pairings. We used medium resolution spectra (FWHM ~ 170 km s $^{-1}$) and saw lines with typical rest frame equivalent widths $W_{\text{rest}} = 0.5$ Å, with a 90% range of $0.2 - 1.3$ Å. We summarise this work under several headings as follows.

10.1 Line-of-sight Associated Absorption

The sample of absorption systems that we use does not conform to some minimum W_{rest} limit. The top panel of Fig. 7 shows the strong tendency of the absorbers in a given spectrum to have $z_{\text{abs}} \simeq z_{\text{em}}$. We see many absorption systems out to $v_{\text{abs}} = 3000$ km s $^{-1}$ and continuing to approximately 10,000 km s $^{-1}$. This distribution is largely determined by the ease of finding absorption near to the emission lines where the SNR is high. While our distribution is very similar to that of Weymann et al. (1981) for a sample like ours that does not employ an equivalent width cutoff, it is also possible that the lower luminosity QSOs presented here have different intrinsic absorption than that seen in the samples of high luminosity QSOs analysed in the 1980s.

In Fig. 3 we showed that many of the QSOs in our sample have similar emission redshifts to their partners. When we compare the absorption redshifts that we see in one spectrum to those in the partner, we often find accidental associations favoured by the interplay of the similar z_{em} values with the excess of absorbers with $v_{\text{abs}} \sim z_{\text{em}}$ in each sight line.

10.2 AA associations of absorbers with absorbers in the paired sight lines

The correlation of absorbers about absorbers describes the distribution of metals around galaxies and the clustering of those galaxies. We learn about the distribution of the pairwise velocities of the halos that cause the absorbers and we

obtain limits on the peculiar velocities of the gas relative to the halos. Our absorber redshift errors of $\sim 23 \text{ km s}^{-1}$ are about ten times smaller than the typical errors for galaxies. This allows us to study the redshift space distortion on rather small scales in a sample that is tiny by galaxy standards.

In the bottom two panels of Fig. 6 and 7 we see the highly significant excess of absorbers at the same redshift as an absorber in a second sight line. We see 17 cases where absorption in one line-of-sight is within 200 km s^{-1} of absorption in the second line-of-sight. Twelve of these 17 coincidences are both $> 3000 \text{ km s}^{-1}$ or approximately 15 Mpc, from their QSOs. This is the first secure detection of coincident absorption in two sight lines separated by about 1 Mpc.

In Fig. 13 we saw that the incidence of AA coincidences is very high for small impact parameters and drops rapidly with increasing separation. In §7.2 we found that the probability of finding an absorber in the partner spectrum is at least $\approx 50\%$ at $< 100 \text{ kpc}$, declining rapidly from 23% at $100 - 200 \text{ kpc}$ to 0.7% by $1 - 2 \text{ Mpc}$. These probabilities are very much lower limits because high resolution spectra with high SNR and full wavelength coverage will show factors of several times more absorbers than do our moderate resolution spectra with partial wavelength coverage.

The rapid drop in the rate of coincidences with separation explains why we are able to detect a significant number of coincidences in 170 pairings of QSOs while Coppolani et al. (2006) did not see any significant correlation in 139 C IV systems towards 32 pairs of QSOs, except for an overdensity of C IV in front of a group of 4 QSOs. Their QSOs had a mean separation of $> 2 \text{ arcmin}$ which is too large.

We can explain the distribution of absorbers around absorbers if each arises in a typical galaxy. Galaxy clustering accounts for the rapid rise in the number of coincidences with small separations. The distribution of points in Fig. 16 shows the expected distribution of absorbers around absorbers from galaxy clustering, and including our errors on the z_{abs} values that are $\sim 23 \text{ km s}^{-1}$.

When we add the expected systematic infall velocities of $\sim 70 - 100 \text{ km s}^{-1}$ we move the points towards a caustic shape with concentrations near both the x and y -axes. We assume that the infall velocities are given by the simulations of Kim & Croft (2007) for a distribution of halo masses $\propto 1/M$. This distribution in Fig. 17 looks more like our data. Other halo mass distribution give similar results because the infall velocities are not much different.

10.3 Absorbers arise in a cold population: blue galaxies, not in winds

The absorber-absorber correlation is sensitive to the redshift-space distortions caused by random peculiar velocities that make the distribution of absorber-absorber separations elongated along the line-of-sight. We see a hint in Figs. 14 and 15 that points are more strongly clustered about the origin in the sky (y) direction but less so in the redshift (x) direction. This is the usual appearance of redshift-space distortion. However, when we calculated the likelihood of obtaining the data as a function of σ_{12} and find that the preferred value is zero, with a 1σ upper limit of 100 km s^{-1} and a 2σ limit of 300 km s^{-1} . The pair wise velocities are

expected to be at least $\sim 240 \text{ km s}^{-1}$ from galaxy data, and hence our absorbers arise in a very “cold” population with minimal random velocities. We conclude that the absorbers arise in the blue rather than the red samples of galaxies discussed in the references of §7.7.

We expect that the distribution of halo masses sets both the infall velocity field and the pair-wise random velocities σ_{12} . We expect a consistent pairing on infall velocities and pair-wise velocities for a given halo mass distribution, with smaller velocities for smaller masses. In Fig 19 we saw that changing the halo mass distribution from $\propto M^{-1}$ to $\propto M^{-2}$ had no effect on the allowed σ_{12} values because low mass halos dominate in both cases. The Kim & Croft (2007) simulations show only a small decrease in the infall velocities for decreasing halo mass below $\sim 2.9 \times 10^{10}$ solar masses. Hence it is unclear if even much lower halo mass would allow the data to be consistent with significantly larger velocity dispersions, from either pair-wise random motions or from winds. We also found that a model with more high mass halos gave similar results to a model with no infall, and that both give lower likelihoods for the data.

Our data set is not compatible with most absorbers arising in winds that flow quickly out from galaxies. Absorption in gas flowing out from galaxies at a mean velocity of 250 km s^{-1} would produce more elongation than we see. We conclude that the absorbing gas does not arise in outflowing winds. The winds seen by Adelberger et al. (2005) in LBG spectra are not representative of absorption systems that we see. Either the winds are confined to LBGs, or they do not extend to $> 40 \text{ kpc}$ with large velocities, or they do not produce absorption we can detect. We are compatible with $1/3$ of strong metal line systems coming from fast winds from LBGs.

In a similar vein, Rauch et al. (2001) found the the Ly α absorption in two pairs of QSOs separated by 86 pc at $z \sim 3.3$ was very similar, implying that strong winds blowing for a substantial fraction of the Hubble time fill less than 20% of the volume of the universe.

10.4 Size and Effect of z_{em} errors

Before we discuss the correlation of absorbers around QSOs, we should summarise what we learnt about the distribution of z_{em} errors.

We know that z_{em} values are often in error by many hundreds of km s^{-1} . The SDSS QSOs in our sample have z_{em} values that are intended to correct for the typical systematic errors in z_{em} values obtained from the common emission lines to give systemic redshifts. We see from Fig. 7(a) that our sample contains about 15 QSOs that probably have z_{em} value too small by $\sim 1000 \text{ km s}^{-1}$ or more, while others will also have such errors and by chance do not show z_{abs} at negative v_{abs} velocities.

However, we also see in Fig. 7(b) that about 12 of our QSOs have z_{em} values with errors of $< 400 \text{ km s}^{-1}$. In Fig. 7(b) we saw that the excess could be represented by a gaussian with a mean -150 km s^{-1} and a $\sigma \sim 525 \text{ km s}^{-1}$. The small absolute value for the mean implies that the redshifts that we use do not have a large systematic error relative to systemic values. The small σ implies that the z_{em} values have small random differences from the systemic redshifts, especially because much of the measured σ will come from

the pair-wise random velocities of the absorbing galaxies relative to the QSO hosts. Since EA coincidences are rare, we can conclude that many of our QSOs have such small z_{em} errors. This conclusion is not very secure because there are few relevant pairings and hence a larger sample could show a wider or displaced peak.

We are lead to speculate that overall the z_{em} errors sample at least two populations; small errors for some QSOs with favourable emission lines and large errors in other cases. The absorption redshifts in the spectra of the partner QSOs may often be better measurements of the systemic velocities of the QSO hosts than are the z_{em} values themselves!

10.5 QSO host population

We can use the distribution of the velocity differences in the QSO-absorber pairings to comment on the QSO host population. The velocity differences include terms from the z_{em} errors and the pair-wise velocity dispersions of QSOs relative to absorbers. We know that both terms can be as large or larger than the small dispersion of $\sigma \sim 525 \text{ km s}^{-1}$ that we see. This suggests that the QSOs, like the absorbers, are in hosts with a low pair-wise velocity dispersion, favouring blue over red galaxies. With the current data and analysis, this conclusion is speculation on what might be done in the near future. The 525 km s^{-1} is not well determined because it is based on few pairing. The value may also be biased because the distribution of absorbers around QSOs appears to be anisotropic because the QSOs destroy some absorbers.

10.6 EA association of absorbers with QSOs in the paired sight lines

We see excess absorption at redshifts similar to the z_{em} values of QSOs close in the sky. We see these absorbers in the bins near zero in Fig. 6(b). We suspect that some of this excess is not caused by ordinary line-of-sight associated absorbers that are selected by chance because the two QSOs have similar z_{em} values. We suspect this because the width of the peak in Fig. 7(b) may be narrower than the distribution of los associated absorbers in Fig. 7(a), and because it would be consistent with the findings of Bowen et al. (2006) and Hennawi et al. (2006). The EA pairings select absorbers that are more concentrated near the QSO host velocities than are the los associated absorbers as a whole. Fig. 7(b) shows that the excess of absorbers around QSOs can be represented by a gaussian with a $\sigma \sim 525 \text{ km s}^{-1}$ that is a much wider distribution than we saw for the clustering of absorbers about absorbers seen in Fig. 7(d) and (e), because of the z_{em} errors are much larger than the z_{abs} errors and because the QSOs may destroy the nearest absorbers.

In §6 we saw that the EA absorbers have absorption lines with W_{rest} values that are typical for our sample as a whole. Most of the systems show C IV lines and we see no excess of N V, though we did not explicitly search for N V in each case.

We discussed the spatial distribution of the absorbers around the QSOs in §8. In Fig. 22 we saw that the EA coincidences are more concentrated to pairings with small impact parameters than are random absorbers. Only 2% of random samples of absorbers would have a stronger preference for

small impact parameters. On the other hand, Fig. 23 shows that the probability of seeing an EA coincidence is relatively constant from 0.1 – 1.5 Mpc. This is a surprise because we know that galaxy clustering should give a rapid increase in probability of a coincidence for smaller impact parameters, as we saw for AA coincidences. We proposed that we do not see the rapid rise in the probability of a coincidence at small impact parameters because QSOs destroy some near by absorbers.

10.7 Is the distribution of absorbers around QSOs anisotropic?

We see signs of anisotropy in the distribution of absorbers around QSOs, both in redshift differences, in the distribution of impact parameters and in prior data. The arguments include the following.

1. Bowen et al. (2006) found 4 Mg II systems that established the existence of transverse associated absorbers that are not seen in the line of sight. Hennawi et al. (2006) reached a similar conclusion in their sample of 149 background QSOs that showed 27 LLS and DLAs near to foreground QSOs.

2. We see transverse absorption that is centred on the z_{em} of the partner QSOs (Fig. 7b) and more tightly centred than are the usual los associated absorbers. Fig. 22 showed the same in the plane of the sky. In redshift and separately in the plane of the sky, the probability of seeing at least this concentration around the QSOs by accident is 2%.

3. We saw that the distribution of absorbers around QSOs is much less concentrated to low impact parameters, than are absorbers around absorbers. This is not due to z_{em} errors, but might be because QSOs destroy the nearest absorbers. This does not mean there is anisotropy, but it implies a process that can cause anisotropy.

4. In a parallel study Kirkman et al. (2007) using a subset of this sample of QSOs, see no sign of the H I transverse proximity effect. The metal lines studied here provide a very sparse sampling of the space around the QSOs. In contrast, the H I provides more samples along a given line of sight. However, they also do not detect the los proximity effect. The lack of the los proximity might be caused by some combination of several effects; systematic z_{em} errors, large random z_{em} errors, higher density of gas near to the QSOs cancelling the QSO UV, and cancellation by extra absorption from the Ly α lines of the associated C IV systems that we see in Fig. 7(a). If the UV is the cause, the UV flux in the transverse direction is less than that along the los, by about a factor of 10 – 100. The Ly α forest data sampling is dense enough to rule out UV emission restricted to irregular patches on the sky, including the line of sight that we see, but without any single well defined beam.

5. The distribution of absorbers around QSOs (Fig. 24) is to first order isotropic, with only a hint of the pattern expected if QSO radiation were beamed.

If the absorber distribution is anisotropic, then the obvious explanations include beamed UV emission (Barthel et al. 1990) and short life times. We can not yet make a distinction with the data presented here, though improved z_{em} values will help. If the QSO UV were anisotropic the total emissivity in UV photons per Mpc^3 is unchanged, since this is set by the number of QSOs observed in any random

direction. However there will be more QSOs luminous at a given time, and their radiation is concentrated in a way that will change the standard picture of ionization spreading out from QSOs in roughly of spherical bubbles that expand and overlap over time.

ACKNOWLEDGMENTS

The data presented herein were obtained using the Kast spectrograph on the Lick Observatory 3m-Shane telescope, and LRIS spectrograph on the Keck-I telescope. The W.M. Keck Observatory is operated as a scientific partnership among the California Institute of Technology, the University of California and the National Aeronautics and Space Administration and was made possible by the generous financial support of the W.M. Keck Foundation. We are exceedingly grateful for the help we receive from the staff at both observatories. We recognise and acknowledge the very significant cultural role and reverence that the summit of Mauna Kea has always had within the indigenous Hawaiian community. We are extremely grateful to have the opportunity to conduct observations from this mountain. Former UCSD students John O'Meara and Nao Suzuki helped to obtain some of the spectra used in this paper. We thank Don Schneider, Chuck Steidel, Jason Prochaska, Jeffrey Newman, Jeff Cooke, Mat Malkan and Peter Bartel for important discussions. Our work was inspired by the pioneering work of Chuck Steidel and his collaborators. Angela Chapman was funded by the NSF REU program grant to the Physics Dept. at UCSD. This work was funded in part by NSF grants AST-0098731 and 0507717 and by NASA grants NAG5-13113.

REFERENCES

- Adelberger K. L., 2004, *ApJ*, 612, 706
- Adelberger K. L., 2005, in Williams P., Shu C.-G., Ménard B., eds, *IAU Colloq. 199: Probing Galaxies through Quasar Absorption Lines Galaxies, intergalactic absorption lines, and feedback at high redshift*. pp 341–348
- Adelberger K. L., Shapley A. E., Steidel C. C., Pettini M., Erb D. K., Reddy N. A., 2005, *ApJ*, 629, 636
- Adelberger K. L., Steidel C. C., 2005, *ApJ*, 630, 50
- Adelberger K. L., Steidel C. C., Kollmeier J. A., Reddy N. A., 2006, *ApJ*, 637, 74
- Adelberger K. L., Steidel C. C., Pettini M., Shapley A. E., Reddy N. A., Erb D. K., 2005, *ApJ*, 619, 697
- Alcock C., Paczynski B., 1979, *Nature*, 281, 358
- Antonucci R., 1993, *AAP*, 31, 473
- Barthel P. D., 1989, *ApJ*, 336, 606
- Barthel P. D., Tytler D. R., Thomson B., 1990, *A&A*, 82, 339
- Best P. N., 2007, *New Astronomy Review*, 51, 168
- Bowen D. V., Hennawi J. F., Ménard B., Chelouche D., Inada N., Oguri M., Richards G. T., Strauss M. A., Vanden Berk D. E., York D. G., 2006, *ApJ*, 645, L105
- Boyle Smith R. J., Shanks T., Croom S. M., Miller L., 1997, *Proc. IAU Symp.* 183, 'Fundamental Cosmological Parameters in Kyoto' (Kyoto 1997)
- Broadhurst T. J., Ellis R. S., Koo D. C., Szalay A. S., 1990, *Nature*, 343, 726
- Chelouche D., Ménard B., Bowen D. V., Gnat O., 2007, *ArXiv e-prints* 0706.4336, 706
- Chen H., Lanzetta K. M., Webb J. K., 2001, *ApJ*, 556, 158
- Churchill C. W., Kacprzak G. G., Steidel C. C., Evans J. L., 2007, *ApJ*, 661, 714
- Coil A. L., Newman J. A., Croton D., Cooper M. C., Davis M., Faber S. M., Gerke B. F., Koo D. C., Padmanabhan N., Wechsler R. H., Weiner B. J., 2007, *ArXiv e-prints*, 2007arXiv0708.0004C
- Cooke J., Wolfe A. M., Gawiser E., Prochaska J. X., 2006, *ApJ*, 652, 994
- Coppolani F., Petitjean P., Stoehr F., Rollinde E., Pichon C., Colombi S., Haehnelt M. G., Carswell B., Teyssier R., 2006, *MNRAS*, 370, 1804
- Cristiani S., D'Odorico S., D'Odorico V., Fontana A., Giallongo E., Savaglio S., 1997, *MNRAS*, 285, 209
- Croft R. A. C., 2004, *ApJ*, 610, 642
- Croom S. M., Boyle B. J., Shanks T., Smith R. J., Miller L., Outram P. J., Loaring N. S., Hoyle F., da Ângela J., 2005, *MNRAS*, 356, 415
- Crotts A. P. S., 1989, *ApJ*, 336, 550
- Crotts A. P. S., Bechtold J., Fang Y., Duncan R. C., 1994, *ApJ*, 437, L79
- Crotts A. P. S., Burles S., Tytler D., 1997, *ApJ*, 489, L7
- Crotts A. P. S., Fang Y., 1998, *ApJ*, 502, 16
- Davis M., Peebles P. J. E., 1983, *ApJ*, 267, 465
- Di Matteo T., Springel V., Hernquist L., 2005, *Nature*, 433, 604
- Dobrzycki A., Bechtold J., 1991a, *ApJ*, 377, L69
- Dobrzycki A., Bechtold J., 1991b, in Crampton D., ed., *The Space Distribution of Quasars Vol. 21 of Astronomical Society of the Pacific Conference Series, The influence of quasars on the Lyman-alpha forest*. pp 272–279
- D'Odorico V., Petitjean P., Cristiani S., 2002, *A&A*, 390, 13
- Faucher-Giguere C. ., Lidz A., Zaldarriaga M., Hernquist L., 2007, *Astrophysics e-prints*, astro-ph/0701042
- Fernandez-Soto A., Barcons X., Carballo R., Webb J. K., 1995, *MNRAS*, 277, 235
- Ganguly R., Brotherton M. S., 2007, *ArXiv e-prints*, 710
- Gaskell C. M., 1982, *ApJ*, 263, 79
- Gaskell C. M., 1983, *ApJ*, 267, L1
- Guimarães R., Petitjean P., Rollinde E., de Carvalho R. R., Djorgovski S. G., Srianand R., Aghaee A., Castro S., 2007, *MNRAS*, 377, 657
- Hamilton T. S., Casertano S., Turnshek D. A., 2002, *ApJ*, 576, 61
- Hennawi J. F., Prochaska J. X., 2007, *ApJ*, 655, 735
- Hennawi J. F., Prochaska J. X., Burles S., Strauss M. A., Richards G. T., Schlegel D. J., Fan X., Schneider D. P., Zakamska N. L., Oguri M., Gunn J. E., Lupton R. H., Brinkmann J., 2006, *ApJ*, 651, 61
- Hennawi J. F., Strauss M. A., Oguri M., Inada N., Richards G. T., Pindor B., Schneider D. P., Becker R. H., Gregg M. D., Hall P. B., Johnston D. E., Fan X., Burles S., Schlegel D. J., Gunn J. E., Lupton R. H., Bahcall N. A., Brunner R. J., Brinkmann J., 2006, *AJ*, 131, 1
- Hui L., Stebbins A., Burles S., 1999, *ApJ*, 511, L5
- Jakobsen P., Jansen R. A., Wagner S., Reimers D., 2003, *A&A*, 397, 891

- Jakobsen P., Perryman M. A. C., 1992, *ApJ*, 392, 432
- Jakobsen P., Perryman M. A. C., di Serego Alighieri S., Ulrich M. H., Macchetto F., 1986, *ApJ*, 303, L27
- Kaiser N., 1987, *MNRAS*, 227, 1
- Kaiser N., 1988, *MNRAS*, 231, 149
- Kim Y.-R., Croft R., 2007, *ArXiv e-prints*, astro-ph/0701012
- Kirkman D., Tytler D., Gleed M., 2007, *ArXiv e-prints*
- Kirkman D., Tytler D., Lubin D., Charlton J., 2007, *MNRAS*, 376, 1227
- Lanzetta K. M., Bowen D., 1990, *ApJ*, 357, 321
- Li C., Jing Y. P., Kauffmann G., Börner G., White S. D. M., Cheng F. Z., 2006, *MNRAS*, 368, 37
- Liske J., 2000, *MNRAS*, 319, 557
- Liske J., Williger G. M., 2001, *MNRAS*, 328, 653
- Loeb A., Eisenstein D. J., 1995, *ApJ*, 448, 17
- Loh J.-M., Quashnock J. M., Stein M. L., 2001, *ApJ*, 560, 606
- Madgwick D., S. H. D., and others 2003, *MNRAS*, 344, 847
- McCarthy J. K., Cohen J. G., Butcher B., Cromer J., Croner E., Douglas W. R., Goeden R. M., Grewal T., Lu B., Petrie H. L., Weng T., Weber B., Koch D. G., Rodgers J. M., 1998, in *Proc. SPIE Vol. 3355*, p. 81-92, *Optical Astronomical Instrumentation*, Sandro D’Odorico; Ed. Blue channel of the Keck low-resolution imaging spectrometer. pp 81–92
- McDonald P., 2003, *ApJ*, 585, 34
- McDonald P., Miralda-Escudé J., 1999, *ApJ*, 518, 24
- Miller L., Lopes A. M., Smith R. J., Croom S. M., Boyle B. J., Shanks T., Outram P., 2004, *MNRAS*, 348, 395
- Milutinovic N., Misawa T., Lynch R. S., Masiero J. R., Palma C., Charlton J. C., Kirkman D., Bockenhauer S., Tytler D., 2007, *ArXiv e-prints*, 2007arXiv0705.1353M
- Misawa T., Charlton J. C., Eracleous M., Ganguly R., Tytler D., Kirkman D., Suzuki N., Lubin D., 2007, *ApJS*, 171, 1
- Misawa T., Eracleous M., Charlton J. C., Tajitsu A., 2005, *ApJ*, 629, 115
- Moller P., Kjaergaard P., 1992, *A&A*, 258, 234
- Narayanan D., Hamann F., Barlow T., Burbidge E. M., Cohen R. D., Junkkarinen V., Lyons R., 2004, *ApJ*, 601, 715
- Oke J. B., Cohen J. G., Carr M., Cromer J., Dingizian A., Harris F. H., Labrecque S., Lucinio R., Schaal W., Epps H., Miller J., 1995, *PASP*, 107, 375
- Pen U.-L., 1999, *ApJS*, 120, 49
- Petitjean P., Bergeron J., 1990, *A&A*, 231, 309
- Petitjean P., Bergeron J., 1994, *A&A*, 283, 759
- Petitjean P., Rauch M., Carswell R. F., 1994, *A&A*, 291, 29
- Pichon C., Scannapieco E., Aracil B., Petitjean P., Aubert D., Bergeron J., Colombi S., 2003, *ApJ*, 597, L97
- Pieri M. M., Schaye J., Aguirre A., 2006, *ApJ*, 638, 45
- Prochaska J. X., Hennawi J. F., Herbert-Fort S., 2007, *ArXiv e-prints*, astro-ph/0703594
- Quashnock J. M., vanden Berk D. E., York D. G., 1996, *ApJ*, 472, L69
- Rauch M., Sargent W. L. W., Barlow T. A., Carswell R. F., 2001, *ApJ*, 562, 76
- Rauch M., Sargent W. L. W., Barlow T. A., Simcoe R. A., 2002, *ApJ*, 576, 45
- Rauch M., Sargent W. L. W., Womble D. S., Barlow T. A., 1996, *ApJ*, 467, L5
- Richards G. T., Vanden Berk D. E., Reichard T. A., Hall P. B., Schneider D. P., SubbaRao M., Thakar A. R., York D. G., 2002, *AJ*, 124, 1
- Richards G. T., York D. G., Yanny B., Kollgaard R. I., Laurent-Muehleisen S. A., vanden Berk D. E., 1999, *ApJ*, 513, 576
- Rollinde E., Petitjean P., Pichon C., Colombi S., Aracil B., D’Odorico V., Haehnelt M. G., 2003, *MNRAS*, 341, 1279
- Rollinde E., Srianand R., Theuns T., Petitjean P., Chand H., 2005, *MNRAS*, 361, 1015
- Romani R. W., Filippenko A. V., Steidel C. C., 1991, *PASP*, 103, 154
- Russell D. M., Ellison S. L., Benn C. R., 2006, *MNRAS*, 367, 412
- Sargent W., Young P., Boksenberg A., Tytler D., 1980, *ApJS*, 42, 41
- Sargent W. L. W., Boksenberg A., Steidel C. C., 1988, *ApJS*, 68, 539
- Sargent W. L. W., Boksenberg A., Young P., 1982, *ApJ*, 252, 54
- Sargent W. L. W., Steidel C. C., 1987, *ApJ*, 322, 142
- Scannapieco E., 2005, *ApJ*, 624, L1
- Scannapieco E., Pichon C., Aracil B., Petitjean P., Thacker R. J., Pogosyan D., Bergeron J., Couchman H. M. P., 2006, *MNRAS*, 365, 615
- Schirber M., Miralda-Escudé J., McDonald P., 2004, *ApJ*, 610, 105
- Schirber M., Miralda-Escudé J., McDonald P., 2004, *ApJ*, 610, 105
- Scoccimarro R., 2004, *PhysRevD*, 70, 083007
- Shanks T., Boyle B. J., Croom S., Loaring N., Miller L., Smith R. J., 2000, in *Mazure A., Le Fèvre O., Le Brun V., eds, Clustering at High Redshift Vol. 200 of Astronomical Society of the Pacific Conference Series, The 2dF QSO Redshift Survey*. pp 57–+
- Shaver P. A., Boksenberg A., Robertson J. G., 1982, *ApJ*, 261, L7
- Shaver P. A., Robertson J. G., 1983, *ApJ*, 268, L57
- Shaver P. A., Robertson J. G., 1985, *MNRAS*, 212, 15P
- Shen Y., Strauss M. A., Oguri M., Hennawi J. F., Fan X., Richards G. T., Hall P. B., Gunn J. E., Schneider D. P., Szalay A. S., Thakar A. R., Vanden Berk D. E., Anderson S. F., Bahcall N. A., Connolly A. J., Knapp G. R., 2007, *AJ*, 133, 2222
- Simcoe R. A., Sargent W. L. W., Rauch M., Becker G., 2006, *ApJ*, 637, 648
- Slosar A., Seljak U., Tasitsiomi A., 2006, *MNRAS*, 366, 1455
- Srianand R., 1997, *ApJ*, 478, 511
- Steidel C. C., Sargent W. L. W., 1991, *AJ*, 102, 1610
- Stoughton C., et al. 2002, *AJ*, 123, 485
- Suzuki N., Tytler D., Kirkman D., O’Meara J. M., Lubin D., 2003, *PASP*, 115, 1050
- Tonry J. L., 1998, *AJ*, 115, 1
- Tytler D., 1982, *Nature*, 298, 427
- Tytler D., 1987, *ApJ*, 321, 49
- Tytler D., Fan X.-M., 1992, *ApJS*, 79, 1
- Tytler D., O’Meara J. M., Suzuki N., Kirkman D., Lubin D., Orin A., 2004, *AJ*, 128, 1058
- Tytler D., Sandoval J., Fan X.-M., 1993, *ApJ*, 405, 57
- Urry C. M., Padovani P., 1995, *PASP*, 107, 803

- Vale A., Ostriker J. P., 2004, MNRAS, 353, 189
 Vanden Berk D. E., et al. 2001, AJ, 122, 549
 Vanden Berk D. E., Stoughton C., Crotts A. P. S., Tytler D., Kirkman D., 2000, AJ, 119, 2571
 Visbal E., Croft R. A. C., 2007, ArXiv e-prints, 2007arXiv0709.2364V
 Weymann R. J., Carswell R. F., Smith M. G., 1981, AnnRAAp, 19, 41
 Williger G. M., Hazard C., Baldwin J. A., McMahon R. G., 1996, ApJS, 104, 145
 Wise J. H., Eracleous M., Charlton J. C., Ganguly R., 2004, ApJ, 613, 129
 Worseck G., Fechner C., Wisotzki L., Dall’Aglia A., 2007, ArXiv e-prints, 2007arXiv0704.0187W
 Worseck G., Wisotzki L., 2006a, A&A, 450, 495
 Worseck G., Wisotzki L., 2006b, ArXiv Astrophysics e-prints, 2006astro.ph.10895W
 Wright E. L., 2006, PASP, 118, 1711
 York D. G., et al. 2000, AJ, 120, 1579
 Young P., Sargent W. L. W., Boksenberg A., 1982, ApJS, 48, 455
 Zehavi I., et al. 2002, ApJ, 571, 172

11 APPENDIX: COMMENTS ON INDIVIDUAL SYSTEMS

11.0.1 P1

EA and AAA coincidences. For EA1 an absorption system in P1a is coincident with the z_{em} of P1b. The C IV and N V are slightly to the blue of their emission lines. Both absorbers are single velocity components. The N V $\lambda 1242.80$ transition is blended with unidentified absorption. For AAA21 the same system in P1a is coincident with a system showing a single velocity component in C IV and Si IV.

11.0.2 P3

An AA coincidence. Both P3a and P3b show strong Mg II and Fe II absorption. There are two velocity components in the Mg II absorption of P3b. The Mg I in P3b shows a single velocity component. The Mg II and Fe II in P3a are also single velocity components.

11.0.3 P5

EA, AA, AAA, and AAV coincidences. For AA2 both P5a and P5b show single velocity components in C IV absorption. For EA2 an absorption system in P5a is coincident with the z_{em} of P5b. AAA22 consists of this same absorption system in P5a and a system in P5b that shows single velocity components in C IV and Si IV. AAV17 consists of an absorption system in P5a containing single velocity components in C IV and Si IV and an absorption system in P5b containing a single velocity component in C IV.

11.0.4 P6

Both P6a and P6b show Mg II absorption comprising the AA3 coincidence. The Mg II in P6a is in a blend but seems

reliable. The Mg II in P6b is less secure. Its Mg II 2803 is the blue side of a blend with N V 1238. We use the redshift $z = 2.5593$ for the N V from its Si III 1206.

The EA3 absorption system in P6a is coincident with the z_{em} of P6b. The C IV has multiple velocity components that are blended. The N V is a single velocity component. Both the N V and C IV are slightly blueward of their emission lines.

The same absorption system in P6a that comprises EA3 is coincident with an absorption system in P6b, which is AAA23. The system in P6b shows a single velocity component in C IV, and it is coincident with the z_{em} of P6a to create EAV19.

11.0.5 P7

An AA coincidence. The C IV in P7a is very strong and is a single velocity component. The Al III is a multiple velocity component. The C IV in P7b is a single velocity component.

11.0.6 P8

EA, EAV, and AAA coincidences. For EA4 an absorption system in P8a is coincident with the z_{em} of P8c. The C IV is a single velocity component and slightly blueward of its emission line. The P8a absorption system of EA4 is also coincident with an associated system of P8c to form AAA24 and an associated system of P8b to form AAA25. The AAA24 absorption system in P8c shows a single velocity component in C IV.

The C IV in the system in P8b is strong and its $\lambda 1550.77$ transition is blended with another C IV at a different redshift. For EA5 the z_{em} of P8a is coincident with the AAA25 absorption system in P8b. For EAV20 the z_{em} of P8c is also coincident with the AAA25 absorption system in P8b. For EA6 the z_{em} of P8a is coincident with another absorption system in P8b. The C IV in this system in P8b is strong and its $\lambda 1548.19$ transition is blended with the C IV in the system mentioned above. We find a Ca II in P8a at $z = 0.4215$.

11.0.7 P22

EA, AA, AAA, EAV, and AAV coincidences. An absorption system in P22a is coincident with the z_{em} of P22b. The same absorption system in P22a is coincident with an absorption system in P22c and two different absorption systems in P22b. The C IV in P22a is strong and has multiple velocity components that are blended. The Si IV has multiple velocity components. The N V in the system in P22c is a single velocity component and is in the Ly α emission line. The two coincidences with P22b are AAA28 and AAA29. For P22b the $\lambda 1550.77$ transition of the C IV in AAA28 is blended with the $\lambda 1548.19$ transition of the C IV in AAA29. In addition, the system in P22c mentioned above is also coincident with the two close proximity systems of P22b to form AAA26 and AAA27 and the z_{em} of P22b to form EAV21. For the AAV coincidence, in P22a the C IV and Si IV are both show a large single velocity component. In P22b the C IV and Si IV both show a small single velocity component.

11.0.8 P23

An EA coincidence. An absorption system in P23a is coincident with the z_{em} of P23b. The C IV is at the peak of the C IV emission line and is a single velocity component.

11.0.9 P25

Two AA coincidences. For P25a the C IV in both coincident systems is a single velocity component. For P25b the C IV in both coincident systems show multiple velocity components.

11.0.10 P31

Two AA coincidences and an AAV coincidence. For AA8 an Mg II absorption system in P31a is coincident with a Mg II absorption system in P31b. The Mg II in P31b is a single velocity component, and the Mg II in P31a is weak but is also a single velocity component. AA9 consists of an absorption system in P31a that shows strong multiple velocity components. C IV and an absorption system in P31b with C IV that is a single velocity component. AAV19 consists of the C IV absorption of P31a of AA9 and C IV absorption in P31b that is a single velocity component.

11.0.11 P36

EA and AAA coincidences. An absorption system in P36b is coincident with the z_{em} of P36a and also with an associated system of P36a. The system in P36b consists of a single velocity component in Si II, Al II and Al III. AAA30 is this system plus a single velocity component N V absorption in P36a.

11.0.12 P38

Two AA coincidences. An absorption system in P38a with large C IV that has multiple velocity components is coincident with an absorption system in P38b with large C IV that has multiple velocity components. Another absorption system in P38a with weak C IV that has multiple velocity components is coincident with an absorption system in P38b with weak C IV that has multiple velocity components.

11.0.13 P42

Two AA coincidences. An absorption system in P42a with Mg II that has multiple velocity components is coincident to a system in P42b with Mg II that is a single velocity component. An absorption system in P42a is coincident with an absorption system in P42b. The C IV in both systems has strong multiple velocity components.

11.0.14 P44

An AA coincidence. An absorption system in P44a with C IV, Mg II, Al II and Fe II identified is coincident with an absorption system in P44b that has C IV identified. The C IV in both systems are large and appear in the Ly α forest.

11.0.15 P70

An AA coincidence. An absorption system in P70a with Mg II and Fe II is coincident with an absorption system in P70b with C IV.

11.0.16 P83

An AAA coincidence. An absorption system in P83a with C IV is coincident with an absorption system in P83b with Si III and H I. The C IV is a single velocity component.

11.0.17 P125

An AAV coincidence. Both of the absorption systems contain C IV. The C IV in P125a is a large single velocity component and the C IV in P125b is a small single velocity component.

11.0.18 P147

An AAA and two EAV coincidences. EAV29 is the coincidence of an absorption system in P147a and the z_{em} of P147b. This same absorption system is also coincident with an absorption system in P147b with a single velocity component in C IV identified. A system in P147b with a single velocity component in C IV identified slightly to the red of the emission line is coincident with the z_{em} of P147a.

11.0.19 P153

EA, AAA and EAV coincidences. One absorption system in P153a and one in P153b are coincident with each other, and with the opposite z_{em} . For the system in P153a only H I and Si III were identified. For the system in P153b, weak single velocity components in C IV and Si IV are identified.

11.0.20 P155

AA and AAA coincidences. An absorption system in P155a is coincident with an absorption system in P155b. Also, another absorption system in P155a is coincident with a separate absorption system in P155b.